

General Disclaimer

One or more of the Following Statements may affect this Document

- This document has been reproduced from the best copy furnished by the organizational source. It is being released in the interest of making available as much information as possible.
- This document may contain data, which exceeds the sheet parameters. It was furnished in this condition by the organizational source and is the best copy available.
- This document may contain tone-on-tone or color graphs, charts and/or pictures, which have been reproduced in black and white.
- This document is paginated as submitted by the original source.
- Portions of this document are not fully legible due to the historical nature of some of the material. However, it is the best reproduction available from the original submission.

ESh3/Eugene Lissner

(NASA-CR-171406) SUPERCONDUCTING GYROSCOPE
RESEARCH Final Report (Alabama Univ.,
Huntsville.) 203 p HC A10/ME AG1 CSCL 14B

N85-25795

Unclassified
G3/35 21187

FINAL REPORT

SUPERCONDUCTING GYROSCOPE RESEARCH

Contract Number NAS8-29316

J. B. Hendricks and G. R. Karr
The University of Alabama in Huntsville

PREPARED FOR

George Marshall Space Flight Center
National Aeronautics Space Administration
Marshall Space Flight Center, Alabama, 35812

February 1985

FINAL REPORT

SUPERCONDUCTING GYROSCOPE RESEARCH

Contract Number NAS8-29316

J. B. Hendricks and G. R. Karr

The University of Alabama in Huntsville

PREPARED FOR

George Marshall Space Flight Center
National Aeronautics Space Administration
Marshall Space Flight Center, Alabama, 35812

February 1985

TABLE OF CONTENTS

Chapter 1. Analysis of a SQUID Readout for a Superconducting Gyroscope	1
Chapter 2. Dependence of Gas Spin-up Torque on Channel and Gas Properties	22
Chapter 3. Theory of Super Fluid Plug Operation	56
Chapter 4. Gyro Rotor and Housing Manufacture	89

Chapter 1 - Analysis of a SQUID Readout for a
Superconducting Gyroscope

I. Introduction

A high sensitivity magnetic flux detector is required for the Relativity Gyroscope Experiment to read out the angular position of the gyro rotor. A magnetic field is generated inside the spinning superconducting rotor, and this field lies along the instantaneous spin axis of the rotor. The magnitude of this field (the "London" Moment) is theoretically,¹

$$B_L = - \frac{2m}{e} \dot{\omega}$$
$$= - 1.137 \times 10^{-11} \dot{\omega} \text{ Tesla}$$

where ω is the spin speed in radians per second. All the published experimental work²⁻⁵ agrees with the theoretical value. There have been speculations that the numerical value might be altered by a few parts per million due to a mass shift of the electrons,⁶ but this has never been verified. We would still expect the direction of the magnetic field to lie exactly along the spin axis in any case.

To measure the orientation of the spin axis, a magnetometer loop is placed around the spinning gyro rotor. For simplicity, we assume the loop lies in a plane, and the center of the spherical gyro rotor lies in the same plane. The magnetic flux linked by the loop will then be (neglecting the return flux between the loop and the sphere).

$$\phi_{\text{meas}} \approx \phi_{\text{max}} \cdot \sin \theta$$
$$\approx B_L \cdot A_{\text{loop}} \cdot \sin \theta$$
$$= (3.572 \times 10^{-11}) r^2 \omega \sin \theta \text{ Weber}$$
$$= (1.726 \times 10^4) r^2 \omega \sin \theta \text{ flux-quanta,}$$

where B_L is the London moment, r is the radius of the sphere in meters, and θ is the angle between the spin axis and the plane of the magnetometer loop. These equations are not exact, but we must establish the exact geometry of the readout loop, etc. before we can make substantial improvements in the accuracy.

The only magnetometer system available at present, that will actually measure a steady magnetic flux of the required sensitivity is based on the Josephson Effect. It is called a SQUID, which originally was an acronym for Superconducting Quantum Interference Detector. A large amount of development has been done on these devices, and a number of review papers have been published describing various types of SQUIDS.⁷⁻¹² The "Best" r.f. SQUID available at present is a commercial unit from SHE Inc.¹³, while the "Best" d.c. SQUID has been described by Clarke, et.al.¹⁴.

A sensitivity number for a given SQUID has little meaning, because the signal must be coupled into the SQUID, and this coupling affects the sensitivity. The effect of coupling will be calculated in Section II. In Section III, we will calculate some inductance values for some superconducting circuits we must use. In some cases it might be useful to limit the bandwidth of the SQUID detector, and this will be considered in Section IV. Finally, in Section V we will calculate the sensitivity of the combined parts of a readout system for a superconducting gyroscope. In Section VI we will calculate the performance required to successfully carry out the Relativity Gyroscope Experiment, and what is left to be done before we can complete a satisfactory SQUID readout system.

II. Flux Transformer Coupling to SQUID Systems

The equivalent circuit of a SQUID detector in its simplest form is shown in Figure 1. It consists of a superconducting circuit, having an inductance L_s , connecting the two ends of a superconducting junction. The equivalent circuit has one turn; the actual SQUID might have more than one turn, or a fractional number of turns. The readout system of the SQUID is not shown. For the single junction SQUID shown a r.f. readout is required; for a two junction SQUID, a d.c. readout can be used. In either case, the SQUID responds to the magnetic flux linking the superconducting SQUID circuit, and this response will be periodic in the flux quantum, $\phi_0 = 2.07 \times 10^{-15}$ Weber.

Usually, the unknown magnetic flux can not be directly applied to the SQUID, so a flux transformer is required. (Figure 2). When a flux is applied to the pick up coil, having an inductance L_p , a current will flow in the superconducting circuit to keep the total flux linked by the circuit a constant. Some of the magnetic flux generated in L_s will then be linked to the SQUID through the mutual inductance, M_{is} .

To calculate the transfer ratio of the magnetic flux, we replace the transformer coupling with a T-equivalent as shown in Figure 3. The circuit can be simplified to a single loop containing a junction. The value of the loop inductance will be the equivalent SQUID inductance with the flux transformer in place. The value of the equivalent inductance, L_s^1 , is:

$$L_s^1 = L_s - (M_{is})^2 / (L_p + L_i)$$

where

L_s = "isolated" SQUID inductance

L_p = pick up coil inductance

L_ℓ = inductance of connecting leads

L_i = inductance of the input coil coupled to the SQUID

M_{is} = mutual inductance between the input coil and the SQUID.

If we use the usual definition of the coupling constant:

$$k_{is} = M_{is}/(L_i L_s)^{1/2},$$

then;

$$L_s^1 = L_s \left\{ 1 - (k_{is}^2 L_i)/(L_p + L_\ell + L_i) \right\}$$

The effect of a flux transformer is to always reduce the value of the inductance.

The amount of flux actually coupled can be calculated from the loop equations;

$$N_p \phi_x = L_p i_1 + L_\ell i_1 + L_i i_1 - M_{is} i_2$$

$$0 = L_s i_2 - M_{is} i_1.$$

The two equations can be combined and rearranged to give the following:

$$\phi_x \left\{ (N_p M_{is})/(L_p + L_i) \right\} =$$

$$i_2 \left\{ L_s - M_{is}^2/(L_p + L_\ell + L_i) \right\}.$$

The quantity in brackets on the right hand side is just the value of equivalent inductance. The amount of flux actually seen by the SQUID

will be:

$$\phi_s = L_s^{-1} i_2,$$

so:

$$\phi_s = \phi_x \left\{ (N_p M_{is}) / (L_p + L_\ell + L_i) \right\}$$

or, using the coupling constant, k:

$$\phi_s = \phi_x \left\{ (k N_p) (L_i L_s)^{1/2} / (L_p + L_\ell + L_i) \right\}.$$

We want to get a maximum transfer of flux through the circuit. Usually, the pick up coil geometry, and it inductance is determined by the experiment requirements. We then want to know what value of L_i to use, to get a maximum transfer for fixed value of L_p , L_ℓ , L_s , and k . By taking the derivative of the transfer equation and setting to zero, we find the maximum occurs when $L_i = L_p + L_\ell$. The maximum value of the transfer ratio is:

$$\left. \frac{\phi_x}{\phi_s} \right]_{max} = (k_{is} N_p) \left\{ L_s (L_p + L_\ell) \right\}^{1/2} / 2(L_p + L_\ell)$$

If we make the additional assumption, that the lead inductance is negligible and that the pick up coil has one turn, then:

$$\left. \frac{\phi_s}{\phi_x} \right]_{max} = k_{is} (L_s/L_p)^{1/2}.$$

A unity value for the transfer ratio can occur if the coupling constant is unity, and if $L_s = L_p$. Since the pick up coil inductance is usually much greater than the SQUID inductance, there is normally a substantial

loss in flux due to the flux transformer. (Note: If $L_p < L_s$, the coupling factor could be greater than unity. This is not a practical solution to the usual problem, because the main reason for a flux transformer is to transform from a high inductance coil to a low inductance SQUID.)

III. Inductance Calculations for Superconducting Circuits

The calculation of inductance values for superconducting structures is complicated, and for our purposes, not necessary. From the previous section we know that our pick up coils will have one or two turns, and should have as small an inductance as possible. To get a small value, the pick up loop should be placed close to the superconducting sphere. To get the smallest possible value for a given spacing, the loop should be a flat band, like a wedding ring around the sphere. This band will form a "Microstrip" transmission line having a length of $2\pi r$. The characteristic impedance of the line will be:¹⁵

$$Z_0 = 377 \text{ (s/w) ohms}$$

where s = spacing between the ball and the band

w = width of the band.

The dielectric is assumed to be a vacuum. The capacitance and inductance per centimeter of line would be:¹⁶

$$C = (1/3Z_0) \times 10^{-10} \text{ Farad/cm}$$

$$L = (Z_0/3) \times 10^{-10} \text{ henry/cm}$$

Therefore, the total inductance of a band around the sphere will be

$$L_T = 7.90 \times 10^{-8} (s/w) r \text{ Henry}$$

where s/w = the spacing to width ratio for the band,
r = radius of the band in meters.

For a 38 mm diameter sphere and a s/w ratio of 0.1,

$$L_T = 1.50 \times 10^{-10} \text{ Henry.}$$

The value of the total inductance will be independent of the position of the sphere inside the loop, as long as the center of the sphere remains in the plane of the loop. If the center of the sphere moves up and down, however, the average spacing will change, and the inductance will change. This change would be a minimum if the band were about the center of the sphere, but in the current gyro design, the loop must be moved about 1 mm above or below the midplane (Fig. 4). Assume the sphere moves perpendicular to the readout loop plane by an amount d. The change in spacing, Δs , will be:

$$\Delta s \approx d \tan \theta$$

where $\sin \theta = \frac{h}{r+s}$

and h = distance the readout loop lies above the midplane,
 r = radius of the sphere,
 s = average spacing between the readout loop and the sphere.

For the existing design, we can use the small angle approximation:

$$\begin{aligned} \Delta s &= dh/r \\ &= 0.053 d. \end{aligned}$$

If the suspension system can keep the sphere centered to $\pm d = \pm 10 \mu$ in, then:

$$\Delta L = \pm 0.35\%.$$

If two loops, one above and one below the mid plane, were connected in series adding, the inductance changes would compensate (to first order, which is the limit of the equations we have used).

IV. Filter Circuits in Flux Transformers

The gyroscope electrostatic suspension and position sensing circuits introduce spurious signals into the flux transformer of SQUID (20 kHz and 1 MHz). In the lab, where the rotor must be supported against gravity, these signals are so large that an unprotected SQUID will not operate. In order to operate in 1-g, we must introduce filtering into the system. In space, the support signals will be much smaller, and this filtering will not be necessary.

The simplest filter would be a normal metal tube placed between the sample (superconducting sphere) and the pick up loop. The R/L ratio of the tube would set the upper pass frequency, and steady signals would not be affected. The tube could also be placed between the SQUID input coil and the SQUID, or a second transformer could be wound in the flux transformer leads. All these methods would affect the degree of coupling possible, due to the physical size of the tube.

If the sphere were actually placed in the SQUID loop itself, the filter tube could be placed between the loop and the sphere. This would certainly mean that the spacing between the loop and ball would be greater,

with a larger value of inductance.

The presence of a normal resistance in a superconducting circuit means that Johnson noise will be introduced. The size and frequency spectrum of this noise has been calculated by Zimmerman¹⁷ and by Jackel, et.al.¹⁸ The noise will severely limit the available sensitivity, and these filter circuits should not be used unless absolutely necessary.

V. Overall Sensitivity of SQUID Detector Systems

The magnetic flux sensitivity of a SQUID detector depends on its inductance. We assume that the independent SQUID parameter, such as the rf coupling constant, etc. are set to an optimum value, as they are usually easily adjusted. The critical current of the junction would also be adjusted to its optimum value ($i_c \sim \phi_0/L_s$). If this is done, the overall sensitivity is:¹⁹

$$S_s \propto L_s^{-1/2}.$$

If we use a flux transformer, the loss ratio would also enter in the equation:

$$S_{FT} = S_s (\phi_s/\phi_x)$$

$$\propto k_{is} N_p (L_p + L_g)^{-1/2}$$

We have assumed that the flux transformer coupling is optimized (the quantities are defined in Sec. II). In this calculation we have assumed that a fixed amount of flux is linked by the pick up coil, regardless of its inductance. This is certainly not the case for magnetic field

detectors using SQUIDS, so our results would not apply. There is also a maximum value of L_s for any SQUID action at all. This is due to thermal fluctuations in the current in the SQUID. The maximum L_s is roughly 1×10^{-8} H_y at 4 K.

The equivalent flux noise generated in a SQUID detector depends on the details of the rf readout circuit and the particular junction used. Theoretically, the noise has the form²⁰⁻²²

$$N_\phi \propto L_s^x$$

where

$$1/2 \leq X \leq 5/6.$$

The value of X used depends on what particular noise source in the SQUID is dominant. If the intrinsic SQUID noise dominates, then $X = 1/2$. If the noise in the r.f. amplifier dominates, then $X = 2/3$. If the Johnson noise generated in the rf tank circuit dominates, then $X = 5/6$. The usual SQUID system is dominated by amplifier noise. It is not certain that the intrinsic noise level has ever been observed.

The overall signal to noise ratio of a complete SQUID system would be:

$$S/N \propto L_s^{-(x+1/2)} \text{ Isolated SQUID}$$

$$S/N \propto 1/2 k_{is} N_p L_s^{-x} (L_p + L_\ell)^{-1/2} \text{ SQUID with Flux Transformer}$$

$$1/2 \leq X \leq 5/6$$

A plot of the theoretical values of noise in a SQUID system is given in Figure 5. Typical values of the various SQUID parameters were selected for the equations, and these are also given at the plot. The

values for two existing SQUID systems are also given on the plot for comparison. All the noise values are for a 1 Hz bandwidth and assume a 20 MHz rf. drive signal.

If the SQUID noise were "white", we could increase the sensitivity (reduce the noise) by reducing the bandwidth of the system. However, if the noise is of the form, f^{-n} , where $n \geq 1$; then bandwidth reduction will not improve the sensitivity. Measured values of the frequency spectrum of two different SQUIDS are given in Figure 6. This shows that a bandwidth of 1×10^{-2} Hz is probably the smallest value that can be used, so the best sensitivity improvement factor would be, $\sqrt{100} \sim 10$.

VI. Conclusions

The signal that is to be measured in a superconducting gyroscope is:

$$\begin{aligned}\phi_m &= \phi_{Lm} \sin \theta \\ &= (5.50 \times 10^3)(r^2\omega) \sin \theta \text{ Flux-quanta}\end{aligned}$$

where

r = radius of sphere in meters

ω = rotational speed in radians/second

θ = angle between spin axis and the plane of the readout loop.

For maximum sensitivity, the gyro should be set up so that θ is small. In this case $\sin \theta \sim \theta$, and the readout is linear in angle.

We will want to make the readout as sensitive as possible, so we will place the SQUID directly around the gyroscope rotor, and dispense with a flux transformer (this is possible as long as the total inductance

of the loop is less than 1×10^{-8} Hz).

To find the minimum detectable angular change, we equate the SQUID noise to the signal. Assuming a signal to noise ratio of one;

$$\phi_m = N_\phi$$

$$(5.50 \times 10^3)(r^2\omega) \theta_{MDS} \approx K_N L_s^x$$

where

$$1/2 \leq x \leq 5/6$$

K_N = noise constant for the SQUID.

However, for a "wedding band" SQUID;

$$L_s = (7.89 \times 10^{-6})(s/w)r \text{ Henry.}$$

Substituting the value of L_s and solving for θ_{MDS} :

$$\theta_{MDS} = K_N \left\{ (7.89 \times 10^{-6})(s/w)r \right\}^x / (5.50 \times 10^3)(r^2\omega)$$

To work out a case for illustration, we will assume the smallest value for x , $x = 1/2$. If we use the published data for the "best" rf SQUID ($L_s = 3 \times 10^{-10}$ Hz, $\phi_N = 1 \times 10^{-4} \phi_0$), we find that $K_N = 0.014$. Putting in these values we find that:

$$\theta_{MDS} = 7.15 \times 10^{-9} \left\{ (s/w)^{1/2} r^{-3/2} \omega^{-1} \right\}$$

Putting in the values for the current gyroscope design; $s/w = .1$, $r = 0.019$ meter, $\omega = 628$ radian/second,

$$\begin{aligned} \theta_{MDS} &= 1.37 \times 10^{-9} \text{ radian} \\ &= 0.283 \times 10^{-3} \text{ arc second} \end{aligned}$$

This value (measured in a 1 Hz bandwidth) will meet the requirements for a measurement of both relativistic effects.

The principal problem with the direct SQUID is the inductance shift due to the ball moving in and out of the plane of the readout loop. If the inductance changed by 0.53% (corresponding to a 10μ in displacement) the scale factor of the readout would also change by 0.53%.

There are two ways to set up the experiment so the shifting scale factor would not be a problem. First, we could null the flux in the SQUID with an external coil, and as long as its scale factor was constant, the scale factor of the SQUID would not matter (the sensitivity would be changed slightly). A second way would be to connect two SQUIDS in series adding, so the inductance changes would cancel out. This could be done either in the superconducting circuit or in the rf readout circuit.

Other ways to use a SQUID with a non-constant scale factor would be to improve the centering performance of the suspension or to use an AGC circuit, which constantly adjusts the gain against a known external signal (such as the orbital aberration).

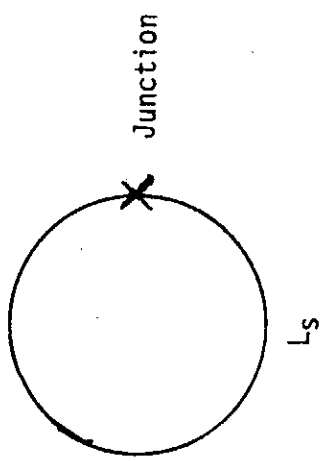
The best method of using the SQUID, and correcting for the scale factor shift, is a subject for system analysis, and can not be answered solely on the basis of SQUID parameters. We have shown that the direct SQUID, with no improvement over existing units, has more than enough sensitivity to meet the requirements of the proposed flight experiment.

REFERENCES

1. London, F., "Superfluids Vol. 1" (Dover, 1960) p. 83.
2. Hildebrandt, A. F., Phys. Rev. Lett., 12, 190 (1964).
3. Hendricks, J. B., C. R. King, and H. E. Rorschach, "Conf. on Low Temp. Physics-LT-9" (Plenum Press-1965) p. 459.
4. Bol, M., and W. M. Fairbank, ibid, p. 471.
5. N. F. Brinkman, Phys. Rev., 184 460 (1969).
6. Anderson, P. W., "Progress in Low Temperature Physics, Vol. V"
(J. Wiley & Sons, 1967) p. 32.
7. Clarke, J., Proc. IEEE, 61, 8 (1973).
8. Goodman, W. L., V. W. Hesterman, L. H. Rorden, and W. S. Goree,
Proc. IEEE, 61, 20 (1973).
9. Zimmerman, J. E. J. Appl. Phys., 42, 30 (1971).
10. Zimmerman, J. E. J. Appl. Phys., 42, 4483 (1971).
11. Webb, W. W., Trans. IEEE, MAG-8, 57 (1972).
12. Giffard, R. P., R. A. Webb, and J. C. Wheatley, J. Low Temp. Phys.,
6, 533 (1972).
13. SHE Corporation, 4174 Sorrento Valley Blvd., San Diego, CA 92121 -
1974 Product Catalog.
14. Clarke, J., W. N. Goubau, and M. B. Ketchen, Appl. Phys. Lett., 27,
155 (1975).
15. "Reference Data for Radio Engineers, 5th Ed.", (H. W. Sams and Co.,
1968) p. 22-26.
16. Ref. 15, p. 22-2.

17. Zimmerman, J. E., *Cryogenics*, 15, 27 (1972).
18. Jackel, L. D., and R. A. Buhrman, *J. Low. Temp. Phys.*, 19, 234 (1975).
19. Falco, C. M. and W. H. Parker, *J. Appl. Phys.* 46, 3238 (1975).
20. Kurkijarvi, J., *Phys. Rev.*, B6, 832 (1972).
21. Kurkijarvi, J., *J. Appl. Phys.*, 44, 3729 (1973).
22. Ref. 18, p. 228.

Figure 1-1
Equivalent Circuit of a SQUID



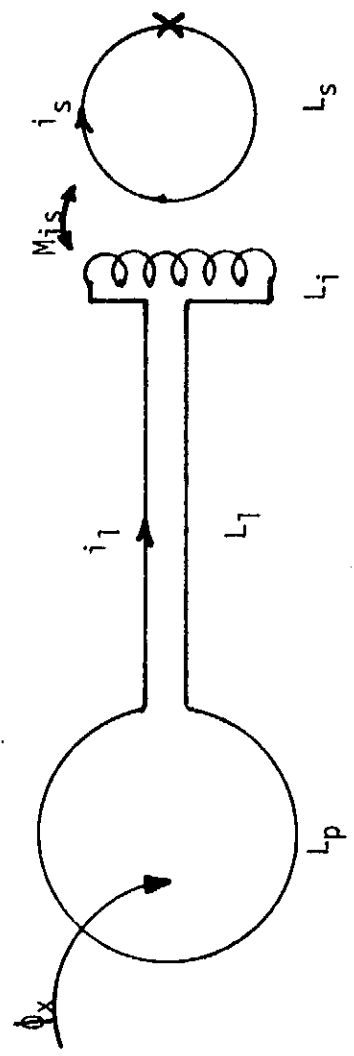


Figure 1-2
A Flux Transformer Coupled SQUID

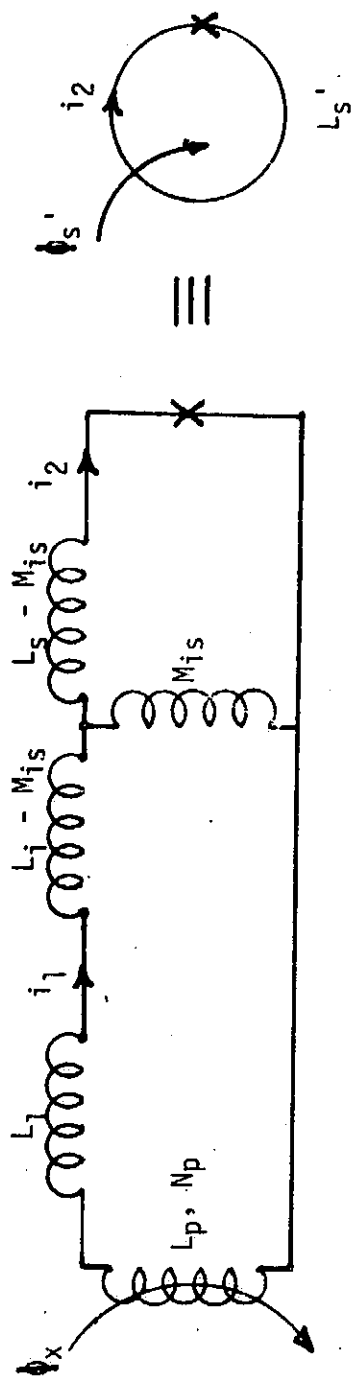


Figure 1-3
Transformer Equivalent of a Flux Transformer
Coupled SQUID

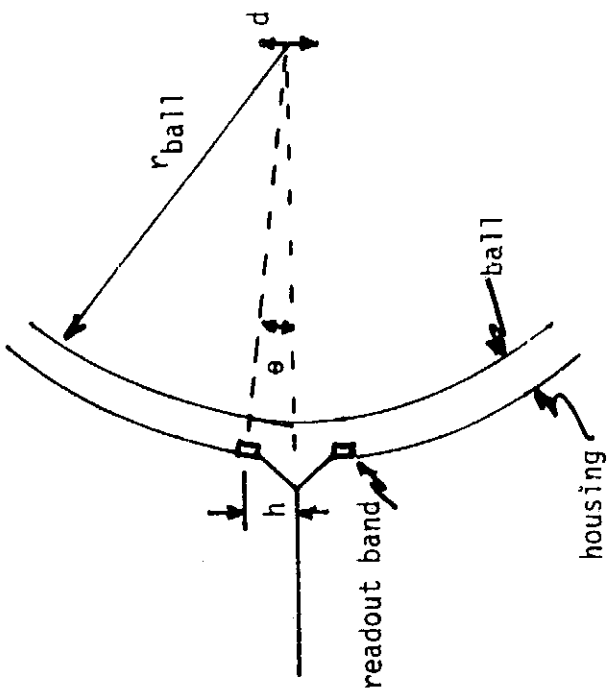


Figure 1-4
Detail of the Superconducting Gyroscope
(cross section)

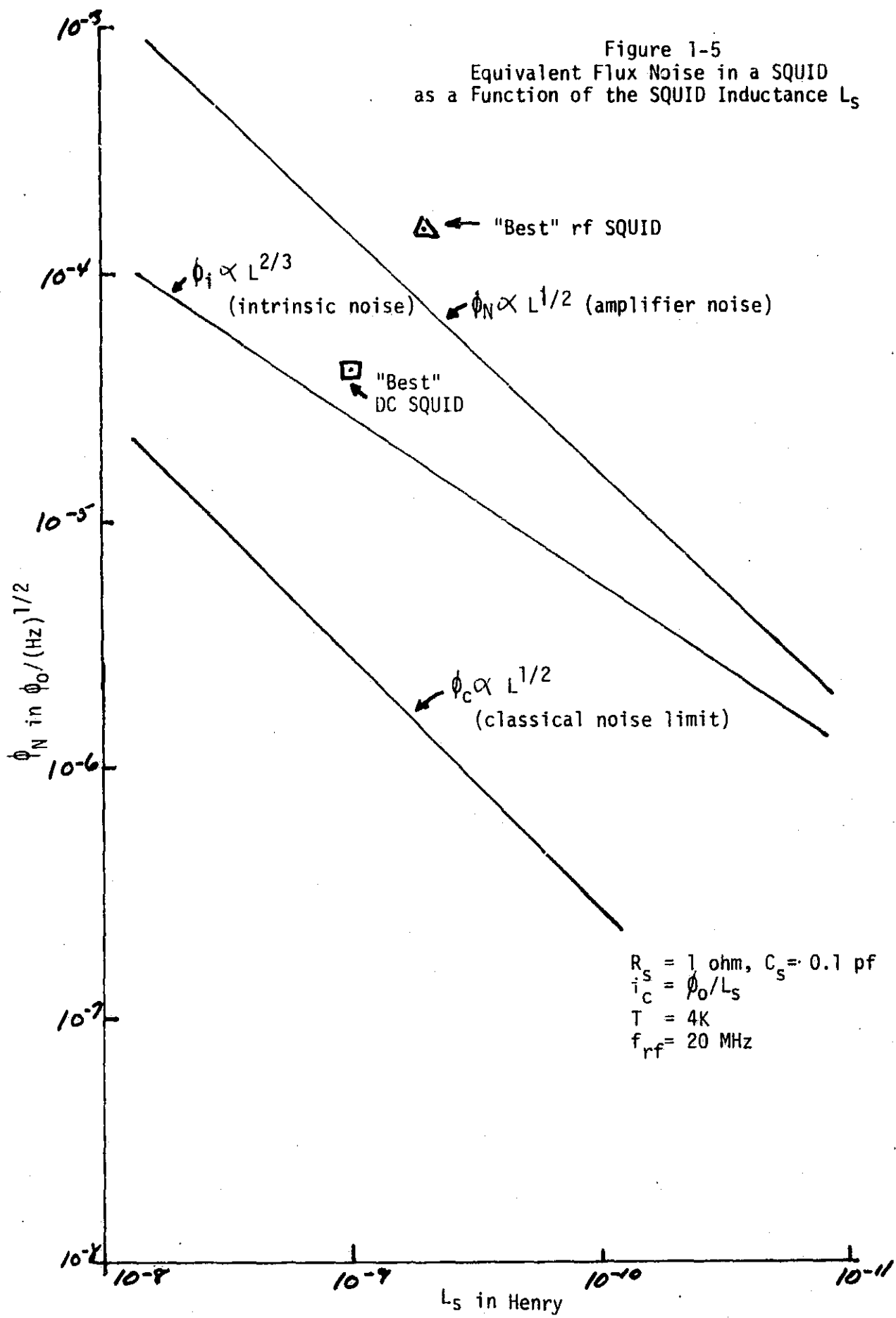
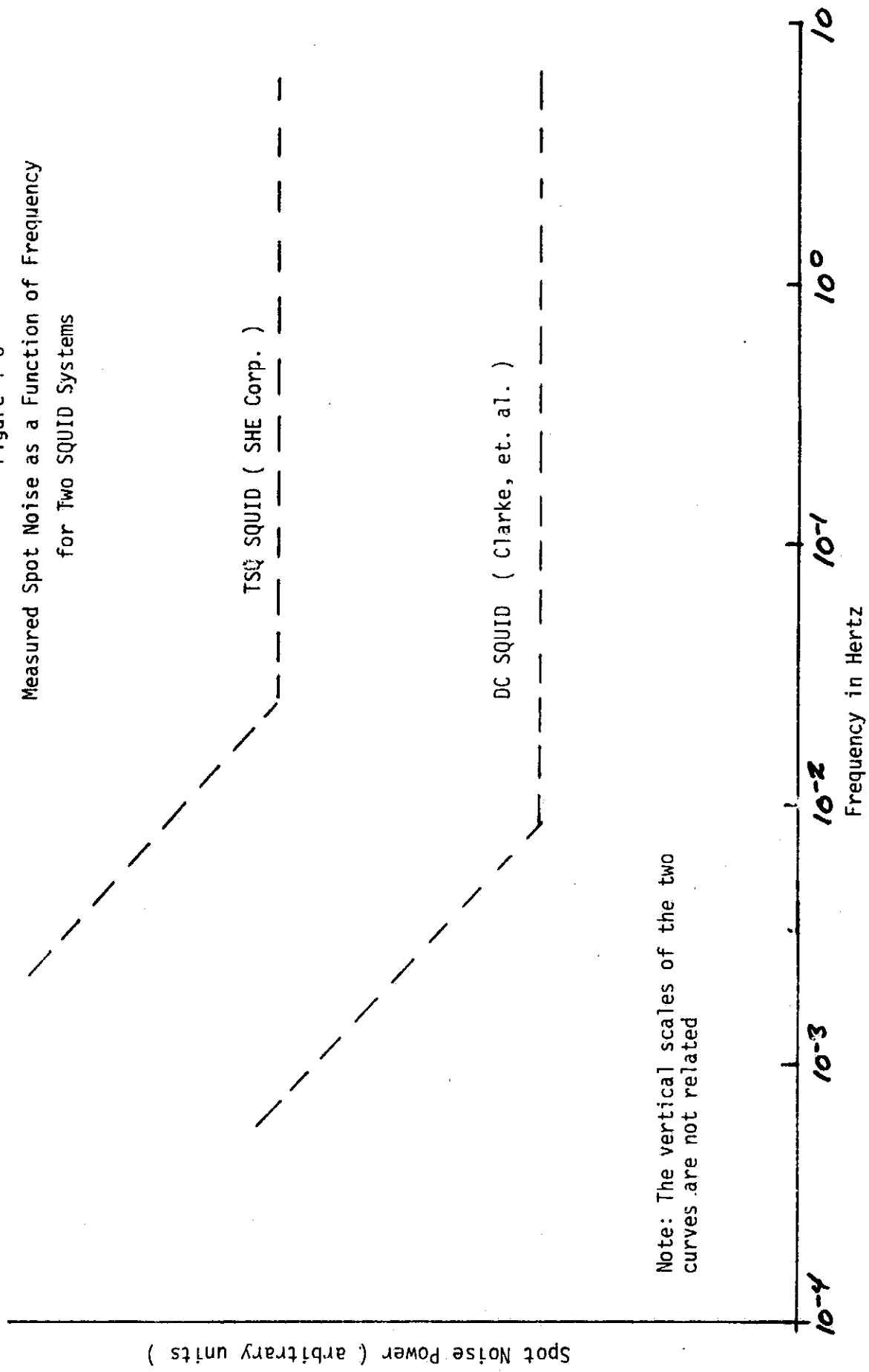


Figure 1-6
Measured Spot Noise as a Function of Frequency
for Two SQUID Systems



Note: The vertical scales of the two curves are not related

Chapter 2 - DEPENDENCE OF GAS SPIN-UP TORQUE ON CHANNEL AND GAS PROPERTIES

I. Introduction

The gas spin-up technique for the relativity gyroscopic has been proven feasible in experiments at Marshall Space Flight Center and at Stanford University. There is, however, a need for a better understanding of the parameters involved in the technique in order to facilitate possible improvement in performance or to assess the effect of changes in channel design which may be required. The following will report on work which has provided the necessary relationship between the spin-up torque and the channel geometry. The gas properties are also included as factors in this theoretical study even though the final system is to be limited to the use of Helium gas at near 4°K.

The results are presented in parametric form which readily illustrates the effect of channel geometry and gas properties on the torque. Experiments performed using gases other than Helium at higher temperature can be used to predict the performance for Helium at 4°K. In addition, the effect of changes in channel cross section and channel length on the parameters can be employed to predict the effect on the torque.

II. Channel Flow Assumptions

In a previous report an approximate method for calculating the torque on the ball was presented. In this work, a more accurate calculation is made, but many of the same assumptions and basic equations are employed which are duplicated here for completeness.

a. Channel Curvature Effects

The spin-up channel for the relativity gyro consists of a groove cut into the spherical cavity wall such that the center line of the groove lies in the equatorial plane of the gyro. The channel is then a curved channel

having an approximate radius of curvature, r , equal to the gyro ball radius, .01905 m. Since the hydraulic diameter, R , of a typical channel is near 2×10^{-3} m, the ratio of hydraulic radius to the radius of curvature is 0.1 or less. For turbulent flow, as is expected at low temperature, the resistance coefficient is given as a function of the Reynolds number R_e and the radius ratio, R/r in reference 1

$$\frac{f}{f_0} = 1 + .075 R_e^{1/4} \left(\frac{R}{r} \right)^{1/2} \quad (1)$$

Since Reynolds numbers of order 1000 are expected, f/f_0 is 1.13 which means that curvature will be expected to increase the friction factor by about 10%. The primary effect will be to decrease the flow rate slightly. The torque on the ball may not be increased, however, since the curvature also results in a gradient of flow properties radially from the center of curvature. This effect will likely cause a decrease in shear force at the ball surface.

In view of the competing affects encountered when curvature is considered, and since the increase in friction coefficient is only 10%, the curvature effects will be neglected in this analysis. The nature of the gradients in flow properties due to curvature will be investigated and possibly included in a future analysis of the flow problem.

b. Geometry of Channel Entrance and Exit

As a result of the above discussion, the channel will be assumed to be straight. The geometry of existing and proposed channels at Marshall Space Flight Center all consist of a converging entrance and exit paths. The centerline of these paths with respect to the channel centerline are not tangential and vary from about 30° in the current design to a high of 90° in a recently proposed design. For the present study, the nature of the pressure drop in the curved entrance and exit paths will not be considered. Instead, the flow into the channel will be assumed to be isentropic with

a stagnation pressure, P_0 . If the pressure downstream of the exit is much lower than P_0 , the exit geometry will not be of importance as long as it is a diverging type.

c. Flow Assumptions

For downstream pressures an order of magnitude or lower than the stagnation pressure, the flow within the channel can be assumed to be choked with a Mach number of unity at the exit to the channel. The channel geometry as discussed above is such that the channel is then entirely subsonic. Supersonic flow could not be maintained in the gyro applications since friction effects would cause a shock to form in the channel which could likely result in unstable operation.

The flow is further assumed to be adiabatic which means that no heat is gained or lost by the gas. This is an assumption which simplifies the calculation but one which should be investigated more closely in future work. The gas will tend to be cooled by the surroundings since the gyro and cavity will be at the stagnation temperature of the gas or at a lower temperature. The effect of friction is to cause an increase in the stagnation temperature of the gas which would result in some heat transfer from the gas to the surroundings at points in the channel. This cooling in a subsonic flow will cause conditions of generally higher pressure and lower velocities than for adiabatic flow. This effect is expected to be negligible for application to the flow calculation but may be important in future calculation of temperature inside the channel during spin-up and the effects this could have on maintaining super conductivity conditions.

The flow will also be assumed to satisfy continuity for the purpose of simplifying the analysis. The leakage of gas out of the channel into the gyro cavity has been shown to be of order 10% for the typical pressure, temperature, and spin-up channel geometry. Future studies will investigate the effect of this leak rate on the channel flow. The effect is expected to give less torque on the ball.

III. Basic Relationships for Gyro Spin-up Torque

The purpose of this work is to determine the shear force acting on the gyro ball during spin-up. The approach taken is that the average shear force, τ , acting on the walls of the channel (including the ball surface as one side of the boundary) can be obtained from the pressure drop, ΔP , across the ends of the channel. The equation is given by

$$\tau = \frac{\Delta PA}{LC} \quad (2)$$

where A is the cross section area of the channel (assumed constant), L is the length of the channel, and C is the perimeter length of the channel cross section. The total force acting on the ball is given by the average shear given above times the area of the ball exposed in the channel, A_b , given by

$$A_b = LW_b \quad (3)$$

where W is the width of the channel at the ball surface. Therefore F_b is given by

$$F_b = \tau A_b = \frac{\Delta PA}{C} W_b \quad (4)$$

The spin-up torque is given by the force F_b acting at the radius of the gyro ball R_b

$$T_b = F_b R_b = \frac{\Delta PA W_b R_b}{C} \quad (5)$$

The determination of ΔP is needed to evaluate the spin-up torque.

IV. Determination of ΔP

The friction between the gas and the channel walls causes the momentum of the gas to be reduced as a function of position along the channel. Differential relationships can be derived which express the corresponding changes in pressure, velocity, temperature, etc. which occur as a result (see Reference 2). As is customary, the effect on Mach number is first given which can be used to compute the changes in the other quantities.

The local shear force acting at the surface is given

$$\tau = 1/2 \rho V^2 f \quad (6)$$

where f is called the local coefficient of friction. The effect on Mach number of this friction force acting on the flow over a length L is given by

$$4\bar{f} \frac{L}{D} = \frac{1-M^2}{kM^2} + \frac{k+1}{2k} \ln \frac{(k+1)M^2}{2(1+\frac{k-1}{2}M^2)} \quad (7)$$

where the flow is assumed to be $M=1$ at the exit. The quantity k is the ratio of specific heats of the gas, D is the hydraulic diameter given by

$$D = \frac{4A}{C} \quad (8)$$

and \bar{f} is the mean friction coefficient given by

$$\bar{f} = \frac{1}{L} \int_0^L f dL \quad (9)$$

the quantity M in equation 7 is the Mach number at the entrance to the channel of length L . The Mach number will be less than unity as discussed earlier.

The pressure ratio of inlet, P_i , to exit, P_e , is given by

$$\frac{P_i}{P_e} = \frac{1}{M} \sqrt{\frac{k+1}{2(1+\frac{k-1}{2}M^2)}} \quad (10)$$

The pressure drop is then given by

$$\Delta P = P_i - P_e = P_i \left(1 - \frac{P_e}{P_i} \right) \quad (11)$$

The pressures in the above are measured at the beginning of the constant area section of the channel and at the end of that channel. The P_i will not be equal to P_o because the gas will have a velocity M at that point. A relationship between P_o and P_i can be obtained from isentropic flow and the flow up to the channel beginning is assumed isentropic for this reason. The value of P_i is related to P_o by

$$P_i = P_o \left(1 + \frac{k-1}{2} M^2\right)^{\frac{k}{k-1}} \quad (12)$$

The equations (10) and (12) substituted into equation (11) gives a relationship between the entrance mach number M and the pressure drop P for a given P_o

$$P = P_o \left(1 + \frac{k-1}{2} M^2\right)^{\frac{k}{k-1}} \quad 1 - M \quad \sqrt{\frac{2 \left(1 - \frac{k-1}{2} M^2\right)}{k+1}} \quad (13)$$

The value of M at the entrance will depend upon the friction factor, f , as indicated in equation 7. The friction factor, in turn, depends on the speed of the flow and also depends upon the type of flow, i.e., laminar or turbulent. Since under room temperature conditions the flow is laminar and under liquid helium temperature the flow is turbulent, both cases will be considered.

The friction factor has been found to be expressible as a function of Reynolds number alone. The Reynolds number for pipe flow is defined as

$$R_e = \frac{W}{A} \frac{D}{\mu} \quad (14)$$

where μ is the viscosity of the gas and W is the mass flow rate. Since continuity is being assumed, W/A will be constant and R_e will be constant except for possible changes in μ . The viscosity μ is a function of temperature which varies along the channel length. Instead of treating the variation in viscosity, an average value of viscosity will be assumed so that the average friction factor defined in equation (9) can be written

$$\bar{f} = f \frac{W}{A} \frac{D}{\bar{\mu}} \quad (15)$$

The effect of this assumption is not expected to be significant since the variation in temperature is small.

The mass flow rate W required in equation (14) can be written as a function of Mach number at the channel entrance also

$$\frac{W}{A} = \sqrt{\frac{k}{R}} \sqrt{T_0} \frac{M}{\left(1 + \frac{k-1}{2} M^2\right)} \frac{k+1}{2(k-1)} \quad (16)$$

where R is the gas constant and T_0 is the stagnation temperature. Equation (16) is an isentropic relationship.

The friction factor can now be written as a function of entrance Mach number using equations (15) and (14). Once the relationship between f and R_e is given, two types of flows are of interest, laminar and turbulent. For laminar flow

$$f_{\text{laminar}} = \frac{16}{R_e} \quad (17)$$

while for turbulent flow

$$f_{\text{turbulent}} = \frac{0.49}{(R_e)^{1/4}} \quad (18)$$

The flow type is determined by the Reynolds number where

$$\text{laminar flow for } R_e \leq 3000$$

$$\text{turbulent flow for } R_e \geq 5000$$

the transition from laminar to turbulent occurs somewhere within the range of 3000 to 5000 region which will not be considered in this work.

Equations (17), (16) and (14) are substituted into equation (7) to provide a relationship for laminar flow between the entrance Mach number and a number of parameters. These parameters can all be collected into a single term called F_L

$$F_L = \frac{L}{D} \frac{\mu}{D} \sqrt{\frac{RT_0}{P_0}} = \frac{1}{64} \left[\frac{1}{k} \left(\frac{1-M^2}{M^2} \right) + \frac{k+1}{2k} \ln \left(\frac{\frac{k+1}{2} M^2}{1 + \frac{k-1}{2} M^2} \right) \right] \frac{k}{\left(1 + \frac{k-1}{2} M^2\right) \frac{k+1}{2(k-1)}} \quad (19)$$

The same procedure is followed for the turbulent flow case using equation (18), (16), and (14) in equation (7), a turbulent flow parameter F_T is obtained

$$F_T = \frac{L}{D} \left(\frac{H}{D} \right)^{1/4} \left(\frac{\sqrt{RT_o}}{P_o} \right)^{1/4} = \frac{1}{1.96} \left[\frac{1}{k} \left(\frac{1-M^2}{M^2} \right) + \frac{k+1}{2k} \ln \left(\frac{\frac{k+1}{2} M^2}{1 + \frac{k-1}{2} M^2} \right) \right] \frac{k^{1/8} M^{1/4}}{\left(1 + \frac{k-1}{2} M^2 \right)^{8(k-1)}} \quad (20)$$

Equation (19) and (20) provide the relationship between L , D , μ , R , T_o , and P_o and entrance Mach number M that is needed to find P in equation (13).

V. Method of Solution

The use of Mach number has resulted in relationships of the form

$$F_T = F_T(M, k); \text{ see equation (20)}$$

$$F_L = F_L(M, k); \text{ see equation (19)}$$

$$\Delta P/P_o = f(M, k); \text{ see equation (13)}$$

If equations (20) and (19) could be solved for M , those results could be used in equation (13) to obtain results of the form

$$\left. \frac{\Delta P}{P_o} \right|_T = f\{M(F_T, k)\} \quad (21)$$

$$\left. \frac{\Delta P}{P_o} \right|_L = f\{M(F_L, k)\} \quad (22)$$

where the relative pressure drop is obtained as a function of F_T or F_L . These results could then be employed in equation (5) to obtain the spin-up torque acting on the ball

$$\left. T_b \right|_T = \frac{AW_b R_b P_o}{C} f\{M(F_T, k)\} \quad (23)$$

$$\left. T_b \right|_L = \frac{AW_b R_b P_o}{C} f\{M(F_L, k)\} \quad (24)$$

The relationships given in equation (21) and (22) are seen to be of central importance.

An analytic solution of equations (19) and (20) was attempted but a solution could not be found for the full range of Mach numbers. Series expressions and polynomial fits

can be employed but the results are found valid only for a limited range of Mach numbers. Since the flow of interest in this work involves changes of Mach number from zero to unity such approximations are not useful. In view of these difficulties, the results were obtained numerically and will be presented both in tabular and graphical form.

The numerical solution of the equation is achieved by obtaining values of F_T and F_L for a range of specific Mach numbers from zero to unity and a specific value of k employing equations (19) and (20). Then, for these same Mach numbers, values of $\Delta P/P_0$ are obtained from equation (13). This procedure is extremely accurate and is simple enough to perform using a desk top scientific calculator. Tables were prepared for the turbulent and laminar flow cases for different k values corresponding to Helium and Nitrogen, the two gases planned for use during spin-up. Results have been obtained for $k = 1.4$ and $k = 1.66$ and these are given here in graphical form in Figures 1, 2, 3, and 4.

VI. Results

The plots given in figure (1) and (2) give the results obtained for the laminar and turbulent flow case for $k = 1.4$ which is the value of k for Nitrogen. The quantity $\Delta P/P_0$ is seen to asymptotically approach zero for small values of F_T or F_L and approaches unity for high values of these quantities. Figures (3) and (4) are similar plots for a value of $k = 1.66$ which corresponds to Helium gas. In addition, Tables 1 and 2 give the values of $\Delta P/P_0$, F_T , F_L , and the flow rate quantity $W\sqrt{RT_0/AP_0}$ as a function of Mach number M for the case of $k = 1.4$ and $k = 1.66$ respectively.

VII. Discussion of Results

The fortunate feature of the results obtained is that a single parameter, either F_T or F_L , governs the resultant $\Delta P/P_0$. This feature allows for the study of the effect on spin-up torque of changes in any of the quantities which make up the parameters F_T and F_L . These quantities are L , D , μ , R , T_0 , and P_0 . Therefore, one can consider the effect of changing the channel geometry which would involve L and D or the effect of changing the type of gas used during spin-up or the stagnation conditions which would effect F_T or F_L through the viscosity, the gas constant R and the stagnation values T_0 and P_0 and of course the value of k .

The results show one feature of particular interest. Since the values of $\Delta P/P_0$ approach an asymptotic value of 1 for high values of F_T or F_L , significant changes in $\Delta P/P_0$ are not possible once this limit has been reached. Only in the middle ranges of F_T and F_L will one be able to influence the $\Delta P/P_0$ values by changes in gas or geometry. Therefore, it is important to first determine what magnitudes of F_T and F_L which correspond to the present design and operating conditions.

Sample Calculations

For purposes of illustration of the use of the results obtained, consider the current Marshall Space Flight Center design for the channel. For this design the following values apply:

$$\begin{aligned} L &= .11703 \text{ m} \\ D &= .197348 \times 10^{-2} \text{ m} \\ A &= 5.83 \times 10^{-6} \text{ m}^2. \end{aligned} \quad (25)$$

For the room temperature runs using N_2 , the following gas properties were typical,

$$\begin{aligned} P_0 &= 866.59 \text{ n/m}^2 \\ T_0 &= 297 \text{ K} \\ R &= (8.3143 \times 10^3 / 28) \text{ J/K}^\circ \cdot \text{kgm} \\ \bar{\mu} &= 1.781 \times 10^{-5} \text{ n} \cdot \text{sec/m}^2 \end{aligned} \quad (26)$$

Under these conditions the value of F_L (the flow is laminar for reasons discussed in an earlier report) is found to be

$$F_L = .190808$$

Referring to the Figure 1 or Table 1 which gives $\Delta P/P_0$ as a function of F_L for $k=1.4$ (corresponding to N_2) one finds that

$$\Delta P/P_0 (F_L = .1908, k = 1.4) = .94176 \quad (28)$$

which means that under these conditions the current design is obtaining nearly the maximum ΔP possible.

Consider now the operation at 4°K with He for the same channel. For this case it has been shown before that the flow will be turbulent and since k for He is

1.66 the curve F_T for $K = 1.66$ is the one of interest. (see Figure 4 or Table 2). Consider the same pressure as before so that the values are now

$$\begin{aligned} P_0 &= 866.59 \text{ N/m}^2 \\ T_0 &= 4 \text{ K}^\circ \\ R &= (8.31434 \times 10^3 / 4) \text{ J/K}^\circ \cdot \text{kgm} \\ \mu &= 2.04815 \times 10^{-6} \text{ N} \cdot \text{sec/m}^2 \end{aligned} \quad (29)$$

using the same D and L values one obtains for F_T

$$F_T = 6.22 \quad (30)$$

Going now to the results for $\Delta P/P_0$ as a function of F_T for $k = 1.66$ one obtains

$$\Delta P/P_0 (F_T = 6.22, k = 1.66) = .712 \quad (31)$$

This result shows first that the torque acting on the ball will be about 75% of the value at room temperature with Nitrogen since we find that the $\Delta P/P_0$ has decreased for the Helium case under the same stagnation pressure conditions. In an earlier report using approximate methods a reduction of about 50% had been predicted. Another conclusion which can be drawn from the above result is that improvement in performance may be possible since the value of $\Delta P/P_0$ is only 0.712.

One design change which has been suggested is a triangular channel gravity having the following properties

$$\begin{aligned} L &= .11703 \text{ m} \\ D &= .084168 \times 10^{-2} \text{ m} \\ A &= 1.0322 \times 10^{-6} \text{ m}^2 \end{aligned} \quad (32)$$

Consider operation of this channel at 4K° with Helium. For this case the value of F_T is found to be

$$F_T = 32.84 \quad (33)$$

Going to the results for $\Delta P/P_0$ vs. F_T for $k = 1.66$ we find (see Figure 4 or Table 2)

$$\Delta P/P_0 (F_T = 32.84, k = 1.66) = .835 \quad (34)$$

which shows that the $\Delta P/P_0$ value has been improved by this design. However, since the cross section area and width of the channel at the ball surface have decreased,

the torque imparted to the ball will be shown to decrease. The torque on the ball is given by

$$T_b = \frac{\Delta P A W_b R_b}{C} \quad (35)$$

A comparison of the torque imparted by the present design, $T_{b_{\text{Present}}}$, to the torque imparted by the triangular design is given by, assuming the same stagnation pressure,

$$\begin{aligned} T_{b_{\text{Triangular}}} &= T_{b_{\text{Present}}} \frac{P_{\text{Tri.}}}{P_{\text{Pres.}}} \frac{A_{\text{Tri.}}}{A_{\text{Pres.}}} \frac{W_{b_{\text{Tri.}}}}{W_{b_{\text{Pres.}}}} \frac{C_{\text{Pres.}}}{C_{\text{Tri.}}} \\ &= T_{b_{\text{Present}}} \frac{.835}{.712} \frac{1.03 \times 10^{-6}}{5.83 \times 10^{-6}} \frac{.2032}{.4064} \frac{1.0948}{.49057} = .23 T_{b_{\text{Present}}} \end{aligned} \quad (36)$$

This shows that the triangular design would produce about 1/4 as much torque.

The triangular design has an advantage, in that, the gas mass flow rate is lower due to the higher friction effects and the smaller cross section area. The results for W are given in Tables 1 and 2 and are also plotted with respect to F_T and F_L for the case of $k = 1.66$ and $k = 1.4$ in Figures 5 and 6.

$$\frac{W}{A_{\text{Pres.}}} \quad (F_T = 6.22, k = 1.66) \quad .493 \quad (37)$$

while

$$\frac{W}{A_{\text{Tri.}}} \quad (F_T = 32.84, k = 1.66) \quad .280 \quad (38)$$

therefore,

$$\frac{W_{\text{triangular}}}{W_{\text{present}}} = \frac{.280}{.493} \frac{A_{\text{triangular}}}{A_{\text{present}}} = .09476 \quad (39)$$

which shows a factor of 10 lower mass flow rate with the triangular design.

Conclusions and Future Work

The sample calculations made in the last section show the utility of the results that have been obtained. In particular the consideration of design changes on the basis of flow rates or torque magnitude is greatly facilitated. The tables and plots provided should be sufficient for most design usages but a computer program is available should more exact values be needed.

Due to the assumptions made, the results tend to overestimate the torque and mass flow rates. The degree of overestimation is difficult to calculate but may be of the order 20% since nearly 10% of the gas leaks from the channel and other effects such as curvature and non-adiabatic flow may contribute. Comparison with experiment will indicate the degree of error and more accurate studies are possible if required. The experimental results could possibly provide a correction factor which could be applied in the theoretical work.

Activities and Results

VIII. 1. Gyro Spin Testing

a. Beryllium Rotor Tests

Due to some delays in obtaining the Nb coated quartz rotor, testing of the S-77 housing design was made first using a Beryllium rotor.

The Beryllium rotor at room temperature has a total clearance of 255 μ . However, as the temperature is lowered to near 4K, the clearance becomes much larger due to the difference in expansion coefficients of the quartz housing and the Beryllium rotor. A total clearance of near 500 μ is predicted at 4K.

The cool down with LN_2 of the S-77 housing with the Beryllium rotor began on July 7 after room temperature tests showed the rotor could be levitated and was free in the housing. At LN_2 temperature, however, the rotor was apparently not free in the housing and could not be levitated. Fearing that the teflon support had broken again, the system was warmed to room temperature and the gyro removed for careful inspection.

The rotor was found to be free, and no failures in the mechanical supports were found. We speculated that a layer of frost may have coated the ball during the cool down to LN_2 temperature. New indium seals were installed and all other seals were tightened so as to cure any Leaks that may have caused the frost.

A second cool down to LN₂ temperature with the Beryllium rotor began July 12. The rotor was suspended and spun at about 10 Hz at room temperature before the cool down began. The suspension system was left on during the cool down. LH_e was transferred later in the day and a spin up to higher speeds was attempted when the temperature monitor indicated that the housing was at 4K.

A spin up to over 100 Hz was achieved in the test described above at a pressure of 2.7 Torr and a gas flow rate of near 30 scc/min. The high vacuum pressure was near 3×10^{-6} Torr. A speed of 100 Hz was reached in a total time of 7.55 min. with accelerated rates of the order of .2 Hz/sec.

Subsequent analysis of the above results tend to indicate that the Beryllium rotor was not at 4K during the spin up but was likely in the 100 to 200 K range. Since the rotor was levitated during the cool down, the heating caused by radiation from the electrodes and resistive heating in the rotor likely balanced the radiation loss to the 4K environment, to maintain a much higher temperature. This theory is supported also by the dynamics of the spin ups, which correspond to temperatures like room temperature rather than 4K. Final confirmation of this theory was made on July 13 after the rotor had been allowed to cool (unsuspended) through the night to 4K. The rotor could not be levitated (likely due to the larger clearance at 4K) and the gas flow indicated a substantially larger rotor-to-housing clearance, since the high vacuum reading was near 10^{-4} Torr for the same flow rates used the previous day. The rotor had obviously not cooled enough in the July 12 test to produce the expected 500 μ clearance.

b. Quartz Rotor Spin Test

The Nb coated quartz rotor was installed on July 15, 1977.

Since the Beryllium rotor test had shown the importance of rotor temperature on the results, a platinum thin film thermometer was installed in the gas exit line in order to monitor the gas temperature after it passed through the spin up channel. There is no concern about the entering gas temperature, since the room temperature gas is first passed through over eight feet of 1/8" copper tubing which is immersed in the liquid helium bath. At typical flow rates of less than 100 scc/min, the temperature of the gas quickly reaches the temperature of the helium bath. However, if the gyro rotor is at a higher temperature, the gas quickly reaches the temperature of the rotor, because of the low flow rates. Thus, the downstream temperature monitor gives a measure of the gyro rotor temperature.

Cool down for quartz rotor tests began on July 18, 1977. By running gas through the channel, the temperature of the rotor could be monitored during the cool down, which showed that the rotor cooled much slower than the rest of the system. The system was backfilled with He to a pressure of 20 Torr to speed up the cooling. The gyro was levitated, and spun up briefly at LN₂ temperature in order to insure that the gyro rotor was free. The suspension was turned off and cool down to LHe temperature began on July 19, 1977.

After all indications that both the housing and the rotor were at 4.2K, spin up was attempted in the afternoon on July 19, 1977. A few spin ups to near 25 Hz were achieved during the initial periods of balancing and adjusting of the suspension system to reduce arcing. Since considerable arcing occurred at pressures above .8 Torr, the gas flow was adjusted to between .65 and .8 Torr, with a flow rate of near 40 scc/min.

Spin up to 106 Hz was achieved after 35 minutes of continuous application of spin up gas. Data on the spin rate was obtained by periodically recording the optical readout signal on an oscilloscope. A plot of this data is given in Figure 1. The test was terminated at a speed of 106 Hz, because an arc occurred which caused the rotor to touch the side of the housing. The gyro could not be levitated after this, so the tests were terminated to allow warm up to room temperature.

c. Spin Test Results

The spin up data shown in Figure 7 indicates that the ultimate speed of the gyro had yet to be reached when the suspension failure occurred. This acceleration rate which is also shown on Figure 7 shows that the gyro was still accelerating at a rate of near 1.5 Hz/min.

Since the gyro spin up is dynamically a first order system, the spin history can be accurately represented as

$$\omega(t) = \omega_f (1 - a_f e^{-b_f t})$$

where ω_f is the ultimate spin speed, a_f is a factor such that $a_f \omega_f$ equals the speed at $t = 0$, and b_f is the rate factor. Figure 8 shows a plot of the equation

$$\omega(t) = 160 (1 - .99 e^{-.031t})$$

along with the July 19, 1977 spin up data. The results show a reasonable fit of the above equation to the data and a maximum speed of 160 Hz. Since the acceleration data is noisy, due to data reduction errors, a bound on the maximum spin speed can be taken to be

$$145 < \omega_f < 195$$

Since the temperature of the spin up has been shown to be an important factor, an analysis has been performed to provide some indication

of the temperature from the spin up data. The following analysis shows that the temperature was likely near 5K. The dynamics of the spin up process, as has been reported in past progress reports, provides the following expression for the maximum spin speed, ω_{\max} , reached by the gyro for a given spin up torque level, T_i :

$$\omega_{\max} = T_i \sqrt{\left(\frac{\mu A_e r^2}{\delta} + \frac{\pi P_c r^4}{\sqrt{2 RT}} \right)}$$

where μ is the gas viscosity, A_e is the area of the channel lip, r is the rotor radius, δ is the spacing between the channel lip area (A_e) and the rotor surface, P_c is the cavity background pressure, and T is the temperature. The first term in the brackets is a viscous drag term due to the high pressure gas between the channel lip area and the rotor surface. The second term is a rarefied gas drag torque due to the low pressure gas in the cavity region of the gyro. Figure 9 shows a plot of ω_{\max} vs. temperature as given by the above equation for constant values of T_i and for the physical quantities corresponding to the S-77 gyro housing with the Nb coated quartz rotor. $P_c = 10^{-3}$ torr was chosen as representative of the conditions during the spin up, although this pressure is not measured directly. For the purposes of this analysis, the values of P_c is not critical to the conclusions reached.

Also shown on Figure 9 as dashed lines are the values for $T_i = 43$ dyne-cm and $\omega_{\max} = 160$ Hz obtained from the analysis of the spin up data. These data points show an intersection at near 5K. The initial torque value was obtained from the data shown in Figure 1 from the equation

$$T_i = I \dot{\omega}(0)$$

where

$$I = m \frac{2}{5} r^2 = 9.246 \times 10^{-6} \text{ kg m}^2$$

and $\omega(0)$ is the initial acceleration rate. Due to the errors in data analysis the value of Γ_i is bounded by

$$40 < \Gamma_i < 55, \text{ dyne-cm}.$$

Thus, taking the bounds on Γ_i and the bounds on ω_{\max} , the temperature is found to be bounded by

$$4.2 < T < 9, \text{ K.}$$

6

The above results agree with the temperature probe which was located in the gas line. This probe, which dissipated approximately 1.0 mw, showed that the temperature was less than 15K. Self heating likely accounts for much of the temperature registered by the monitor. A different probe is being prepared for future tests.

d. Housing Damage

The housing was damaged by the sudden drop of the gyro rotor caused by the suspension failure at over 100 Hz spin speed. The rotor was not damaged, however. Both halves of the gyro housing were found to have a plane sheared to a depth of about 1/8" in the area opposite the drive channel. This is a region which is directly above the electrode, opposite the drive channel. This region has a sharp lip, which remains after cutting the electrode groove, and the .060 x .030 ring around the housing half. (See drawings of housing in June progress report.) The sheared region did not propagate into the electrode, which means that the housing can be used again. The pins which hold the two halves together were also found to be sheared, which is the reason the gyro could not be levitated after the suspension failure. New pins will be made, and the housing will be reassembled for future testing, after the sharp edges have been removed from the housing interior.

References

1. Schlichting, H., Boundary Layer Theory, 4th ed., McGraw-Hill, 1960.
2. Shapiro, A. H., Compressible Fluid Flow, Vol. I and Vol. II, Ronald Press, 1954.

Table 2-1 - Channel Flow Relationships for $k = 1.4$

M	$\Delta P/P_0$	$F_L = \frac{L}{D} \frac{\mu}{D} \frac{\sqrt{RT_0}}{P_0}$	$F_T = \frac{L}{D} \left(\frac{\mu \sqrt{RT_0}}{DP_0} \right)^{1/4}$	$\frac{W \sqrt{RT_0}}{A P_0}$
.000100	.99991+00	.13206+03	.38009+08	.11832+03
.001000	.99909+00	.13205+02	.67589+06	.11832+02
.002000	.99818+00	.66023+01	.20093+06	.23664+02
.003000	.99727+00	.44012+01	.98824+05	.35496+02
.004000	.99636+00	.33006+01	.59729+05	.47328+02
.005000	.99545+00	.26402+01	.40714+05	.59168+02
.006000	.99455+00	.21998+01	.29370+05	.75991+02
.007000	.99364+00	.18853+01	.22423+05	.82823+02
.008000	.99274+00	.16493+01	.17747+05	.94654+02
.009000	.99184+00	.14658+01	.14439+05	.10648+01
.010000	.99094+00	.13189+01	.12005+05	.11831+01
.020000	.98202+00	.65743+00	.35586+04	.23659+01
.030000	.97322+00	.43631+00	.17428+04	.35477+01
.040000	.96456+00	.32533+00	.10477+04	.47283+01
.050000	.95502+00	.25846+00	.70433+03	.59072+01
.060000	.94759+00	.21366+00	.50809+03	.70840+01
.070000	.93928+00	.18149+00	.38470+03	.82582+01
.080000	.93108+00	.15723+00	.30172+03	.94295+01
.090000	.92299+00	.13826+00	.24306+03	.10597+00
.100000	.91500+00	.12298+00	.19995+03	.11761+00
.110000	.90710+00	.11041+00	.16729+03	.12921+00
.120000	.89930+00	.99874+01	.14191+03	.14077+00
.130000	.89159+00	.90902+01	.12177+03	.15227+00
.140000	.88397+00	.83167+01	.10551+03	.16372+00
.150000	.87643+00	.76424+01	.92187+02	.17511+00
.160000	.86896+00	.70490+01	.81125+02	.18644+00
.170000	.86157+00	.65226+01	.71836+02	.19770+00
.180000	.85425+00	.60522+01	.63958+02	.20889+00
.190000	.84699+00	.56292+01	.57219+02	.22001+00
.200000	.83979+00	.52468+01	.51409+02	.23105+00
.210000	.83266+00	.48993+01	.46363+02	.24201+00
.220000	.82557+00	.45821+01	.41955+02	.25289+00
.230000	.81853+00	.42915+01	.38082+02	.26368+00
.240000	.81154+00	.40242+01	.34660+02	.27438+00
.250000	.80459+00	.37775+01	.31624+02	.28498+00
.260000	.79768+00	.35494+01	.28918+02	.29549+00
.270000	.79080+00	.33377+01	.26497+02	.30589+00
.280000	.78395+00	.31408+01	.24322+02	.31619+00
.290000	.77712+00	.29573+01	.22363+02	.32638+00
.300000	.77031+00	.27860+01	.20592+02	.33647+00
.310000	.76352+00	.26257+01	.18987+02	.34644+00
.320000	.75674+00	.24755+01	.17528+02	.35629+00

Table 2-1 Channel Flow Relationships for k = 1.4

(continued)

M	$\Delta P/P_o$	$F_L = \frac{L}{D} \frac{\bar{\mu}}{D} \frac{\sqrt{RT_o}}{P_o}$	$F_T = \frac{L}{D} \left(\frac{\bar{\mu}}{D} \frac{\sqrt{RT_o}}{P_o} \right)^{1/4}$	$\frac{W}{A} \frac{\sqrt{RT_o}}{P_o}$
.330000	.74997+00	.23346-01	.16199+02	.36602+00
.340000	.74320+00	.22021-01	.14986+02	.37563+00
.350000	.73642+00	.20775-01	.13876+02	.38512+00
.360000	.72964+00	.19601-01	.12859+02	.39448+00
.370000	.72285+00	.18495-01	.11924+02	.40371+00
.380000	.71605+00	.17451-01	.11064+02	.41281+00
.390000	.70922+00	.16464-01	.10272+02	.42178+00
.400000	.70237+00	.15532-01	.95410+01	.43061+00
.410000	.69549+00	.14651-01	.89658+01	.43938+00
.420000	.68858+00	.13916-01	.83866+01	.44786+00
.430000	.68162+00	.13026-01	.76617+01	.45627+00
.440000	.67463+00	.12278-01	.71249+01	.46464+00
.450000	.66758+00	.11569-01	.66266+01	.47266+00
.460000	.66048+00	.10896-01	.61637+01	.48064+00
.470000	.65331+00	.10259-01	.57332+01	.48847+00
.480000	.64609+00	.96543-02	.53326+01	.49615+00
.490000	.63879+00	.90808-02	.49594+01	.50368+00
.500000	.63141+00	.85367-02	.46117+01	.51105+00
.510000	.62396+00	.80205-02	.42875+01	.51828+00
.520000	.61641+00	.75307-02	.39849+01	.52535+00
.530000	.60877+00	.70660-02	.37026+01	.53224+00
.540000	.60104+00	.66251-02	.34389+01	.53902+00
.550000	.59319+00	.62069-02	.31925+01	.54563+00
.560000	.58524+00	.58103-02	.29623+01	.55207+00
.570000	.57714+00	.54342-02	.27471+01	.55836+00
.580000	.56896+00	.50776-02	.25459+01	.56449+00
.590000	.56064+00	.47397-02	.23578+01	.57046+00
.600000	.55217+00	.44195-02	.21819+01	.57628+00
.610000	.54356+00	.41163-02	.20173+01	.56193+00
.620000	.53479+00	.38293-02	.18635+01	.58743+00
.630000	.52587+00	.35577-02	.17196+01	.59276+00
.640000	.51678+00	.33008-02	.15851+01	.59794+00
.650000	.50752+00	.30581-02	.14593+01	.60296+00
.660000	.49807+00	.28268-02	.13418+01	.60782+00
.670000	.48844+00	.26124-02	.12320+01	.61252+00
.680000	.47860+00	.24083-02	.11295+01	.61707+00
.690000	.46857+00	.22159-02	.10338+01	.62145+00
.700000	.45831+00	.20348-02	.94446+00	.62568+00
.710000	.44784+00	.18645-02	.86121+00	.62976+00
.720000	.43713+00	.17045-02	.78364+00	.63368+00
.730000	.42618+00	.15543-02	.71142+00	.63744+00
.740000	.41499+00	.14135-02	.64426+00	.64105+00

Table 2-1 Channel Flow Relationships for $k = 1.4$

(continued)

M	$\Delta P/P_0$	$F_L = \frac{L}{D} \frac{\bar{\mu}}{D} \frac{\sqrt{RT_0}}{P_0}$	$F_T = \frac{L}{D} \left(\frac{\bar{\mu}}{D} \frac{\sqrt{RT_0}}{P_0} \right)^{1/4}$	$\frac{W}{A} \sqrt{\frac{RT_0}{P_0}}$
.750000	.40353+00	.12818-02	.58186+00	.64450+00
.760000	.39181+00	.11586-02	.52395+00	.64781+00
.770000	.37980+00	.10437-02	.47027+00	.65096+00
.780000	.36751+00	.93672-03	.42060+00	.65396+00
.790000	.35492+00	.83723-03	.37470+00	.65681+00
.800000	.34202+00	.74495-03	.33238+00	.65952+00
.810000	.32880+00	.65954-03	.29342+00	.66208+00
.820000	.31524+00	.58072-03	.25765+00	.66449+00
.830000	.30134+00	.50818-03	.22489+00	.66676+00
.840000	.28709+00	.44163-03	.19497+00	.66888+00
.850000	.27247+00	.38082-03	.16775+00	.67087+00
.860000	.25747+00	.32548-03	.14308+00	.67271+00
.870000	.24208+00	.27535-03	.12081+00	.67442+00
.880000	.22628+00	.23020-03	.10083+00	.67598+00
.890000	.21007+00	.18979-03	.82996-01	.67742+00
.900000	.19343+00	.15390-03	.67206-01	.67872+00
.910000	.17633+00	.12232-03	.53345-01	.67988+00
.920000	.15878+00	.94832-04	.41310-01	.68092+00
.930000	.14076+00	.71244-04	.31004-01	.68183+00
.940000	.12224+00	.51360-04	.22332-01	.68261+00
.950000	.10323+00	.34998-04	.15206-01	.68327+00
.960000	.83686-01	.21979-04	.95442-02	.68380+00
.970000	.63611-01	.12132-04	.52657-02	.68421+00
.980000	.42983-01	.52909-05	.22957-02	.68456+00
.990000	.21785-01	.12980-05	.56308-03	.68467+00
.991000	.19633-01	.10494-05	.45523-03	.68469+00
.992000	.17475-01	.82750-06	.35898-03	.68469+00
.993000	.15312-01	.63241-06	.27434-03	.68470+00
.994000	.13142-01	.46382-06	.20121-03	.68471+00
.995000	.10967-01	.32155-06	.13949-03	.68472+00
.996000	.87855-02	.20530-06	.89060-04	.68472+00
.997000	.65981-02	.11522-06	.49982-04	.68473+00
.998000	.44048-02	.51109-07	.22171-04	.68473+00
.999000	.22054-02	.12728-07	.55213-05	.68473+00
1.000000	.000000	.000000	.000000	.68473+00

Table 2-2 Channel Flow Relationships for k = 1.66

M	$\Delta P/P_0$	$F_L = \frac{L}{D} \frac{\mu}{D} \frac{\sqrt{RT_o}}{P_o}$	$F_T = \frac{L}{D} \left(\frac{\mu}{D} \frac{\sqrt{RT_o}}{P_o} \right)^{1/4}$	$\frac{W}{A} \frac{\sqrt{RT_o}}{P_o}$
.000100	.99991+00	.12127+03	.32745+08	.12884-03
.001000	.99913+00	.12127+02	.58229+06	.12884-02
.002000	.99827+00	.60632+01	.17311+06	.25768-02
.003000	.99741+00	.40418+01	.85138+05	.38652-02
.004000	.99654+00	.30311+01	.51456+05	.51536-02
.005000	.99569+00	.24245+01	.34817+05	.64419-02
.006000	.99483+00	.20201+01	.25302+05	.77303-02
.007000	.99397+00	.17312+01	.19317+05	.90186-02
.008000	.99312+00	.15145+01	.15288+05	.10307-01
.009000	.99226+00	.13460+01	.12438+05	.11595-01
.010000	.99141+00	.12111+01	.10341+05	.12803-01
.020000	.98298+00	.60353+00	.30648+04	.25761-01
.030000	.97471+00	.40039+00	.15004+04	.38629-01
.040000	.96659+00	.29841+00	.90157+03	.51482-01
.050000	.95861+00	.23694+00	.60582+03	.64314-01
.060000	.95078+00	.19576+00	.43678+03	.77120-01
.070000	.94308+00	.16617+00	.33051+03	.89896-01
.080000	.93551+00	.14386+00	.25905+03	.10264+00
.090000	.92807+00	.12639+00	.20854+03	.11533+00
.100000	.92074+00	.11234+00	.17143+03	.12799+00
.110000	.91354+00	.10077+00	.14331+03	.14059+00
.120000	.90644+00	.91067-01	.12147+03	.15314+00
.130000	.89946+00	.82808-01	.10415+03	.16563+00
.140000	.89257+00	.75686-01	.90165+02	.17805+00
.150000	.88578+00	.69479-01	.78709+02	.19040+00
.160000	.87908+00	.64017-01	.69200+02	.20268+00
.170000	.87247+00	.59172-01	.61220+02	.21488+00
.180000	.86594+00	.54843-01	.54454+02	.22700+00
.190000	.85949+00	.50952-01	.48669+02	.23903+00
.200000	.85312+00	.47435-01	.43684+02	.25096+00
.210000	.84681+00	.44240-01	.39357+02	.26280+00
.220000	.84056+00	.41325-01	.35578+02	.27454+00
.230000	.83437+00	.38656-01	.32260+02	.28618+00
.240000	.82824+00	.36202-01	.29330+02	.29771+00
.250000	.82215+00	.33940-01	.26732+02	.30912+00
.260000	.81610+00	.31848-01	.24418+02	.32042+00
.270000	.81010+00	.29908-01	.22349+02	.33160+00
.280000	.80412+00	.28106-01	.20492+02	.34266+00
.290000	.79818+00	.26428-01	.18820+02	.35359+00
.300000	.79226+00	.24863-01	.17310+02	.36439+00
.310000	.78635+00	.23399-01	.15943+02	.37505+00
.320000	.78046+00	.22030-01	.14701+02	.38558+00

Table 2-2 Channel Flow Relationships for k = 1.66

(continued)

M	$\Delta P/P_o$	$F_L = \frac{L}{D} \frac{\bar{H}}{D} \sqrt{\frac{RT_o}{P_o}}$	$F_T = \frac{L}{D} \left(\frac{\bar{H}}{D} \sqrt{\frac{RT_o}{P_o}} \right)^{1/4}$	$\frac{W}{A} \sqrt{\frac{RT_o}{P_o}}$
.330000	.77457+00	.20746-01	.13571+02	.39598+00
.340000	.76869+00	.19540-01	.12540+02	.40623+00
.350000	.76280+00	.18408-01	.11597+02	.41638+00
.360000	.75691+00	.17342-01	.10734+02	.42629+00
.370000	.75099+00	.16339-01	.99417+01	.43610+00
.380000	.74506+00	.15393-01	.92137+01	.44576+00
.390000	.73910+00	.14501-01	.85436+01	.45526+00
.400000	.73311+00	.13660-01	.79260+01	.46468+00
.410000	.72708+00	.12865-01	.73558+01	.47379+00
.420000	.72100+00	.12113-01	.68289+01	.48282+00
.430000	.71498+00	.11403-01	.63413+01	.49169+00
.440000	.70869+00	.10731-01	.58897+01	.50039+00
.450000	.70245+00	.10096-01	.54710+01	.50893+00
.460000	.69613+00	.94941-02	.50824+01	.51720+00
.470000	.68974+00	.89246-02	.47215+01	.52550+00
.480000	.68326+00	.83854-02	.43861+01	.53353+00
.490000	.67670+00	.78748-02	.40741+01	.54140+00
.500000	.67003+00	.73913-02	.37836+01	.54909+00
.510000	.66327+00	.69333-02	.35132+01	.55662+00
.520000	.65639+00	.64996-02	.32611+01	.56397+00
.530000	.64939+00	.60888-02	.30262+01	.57115+00
.540000	.64226+00	.56999-02	.28071+01	.57815+00
.550000	.63500+00	.53316-02	.26027+01	.58498+00
.560000	.62760+00	.49829-02	.24119+01	.59164+00
.570000	.62005+00	.46529-02	.22339+01	.59813+00
.580000	.61234+00	.43497-02	.20676+01	.60444+00
.590000	.60446+00	.40454-02	.19124+01	.61058+00
.600000	.59640+00	.37661-02	.17675+01	.61654+00
.610000	.58816+00	.35022-02	.16321+01	.62233+00
.620000	.57973+00	.32528-02	.15057+01	.62795+00
.630000	.57109+00	.30174-02	.13877+01	.63340+00
.640000	.56224+00	.27951-02	.12775+01	.63867+00
.650000	.55317+00	.25855-02	.11747+01	.64378+00
.660000	.54387+00	.23879-02	.10787+01	.64871+00
.670000	.53432+00	.22018-02	.98918+00	.65348+00
.680000	.52452+00	.20266-02	.90571+00	.65808+00
.690000	.51445+00	.18619-02	.82791+00	.66251+00
.700000	.50412+00	.17071-02	.75545+00	.66677+00
.710000	.49349+00	.15618-02	.68799+00	.67087+00
.720000	.48257+00	.14256-02	.62524+00	.67431+00
.730000	.47134+00	.12981-02	.56691+00	.67858+00
.740000	.45979+00	.11787-02	.51275+00	.68219+00
.750000	.44791+00	.10673-02	.46251+00	.68565+00

Table 2-2 Channel Flow Relationships for $k = 1.66$

(continued)

M	$\Delta P/P_o$	$F_L = \frac{L}{D} \frac{\bar{H}}{D} \sqrt{\frac{RT_o}{P}}$	$F_T = \frac{L}{D} \left(\frac{\bar{H}}{D} \sqrt{\frac{RT_o}{P_o}} \right)^{1/4}$	$\frac{W}{A} \sqrt{\frac{RT_o}{P_o}}$
.760000	.43568+00	.96332-03	.41596+00	.68894+00
.770000	.42309+00	.86651-03	.37289+00	.69208+00
.780000	.41013+00	.77654-03	.33309+00	.69506+00
.790000	.39679+00	.69306-03	.29638+00	.69789+00
.800000	.38305+00	.61579-03	.26258+00	.70057+00
.810000	.36889+00	.54442-03	.23152+00	.70310+00
.820000	.35431+00	.47868-03	.20305+00	.70548+00
.830000	.33928+00	.41830-03	.17702+00	.70771+00
.840000	.32380+00	.36303-03	.15329+00	.70980+00
.850000	.30785+00	.31262-03	.13173+00	.71175+00
.860000	.29140+00	.26682-03	.11222+00	.71355+00
.870000	.27445+00	.22543-03	.94647-01	.71522+00
.880000	.25698+00	.18822-03	.78896-01	.71675+00
.890000	.23897+00	.15498-03	.64868-01	.71815+00
.900000	.22041+00	.12551-03	.52466-01	.71941+00
.910000	.20127+00	.99628-04	.41597-01	.72059+00
.920000	.18154+00	.77144-04	.32176-01	.72155+00
.930000	.16119+00	.57884-04	.24120-01	.72243+00
.940000	.14022+00	.41679-04	.17354-01	.72319+00
.950000	.11859+00	.28367-04	.11804-01	.72382+00
.960000	.96300-01	.17794-04	.74002-02	.72433+00
.970000	.73315-01	.98102-05	.40782-02	.72473+00
.980000	.49617-01	.42737-05	.17761-02	.72503+00
.990000	.25187-01	.10473-05	.43517-03	.72517+00
.991000	.22702-01	.84664-06	.35179-03	.72518+00
.992000	.20210-01	.66753-06	.27737-03	.72519+00
.993000	.17711-01	.51001-06	.21191-03	.72520+00
.994000	.15204-01	.37408-06	.15543-03	.72521+00
.995000	.12689-01	.25915-06	.10768-03	.72521+00
.996000	.10167-01	.16560-06	.68804-04	.72522+00
.997000	.76367-02	.92978-07	.38632-04	.72522+00
.998000	.50989-02	.41183-07	.17111-04	.72523+00
.999000	.25533-02	.10282-07	.42719-05	.72523+00
1.000000	.000000	.000000	.000000	.72523+00

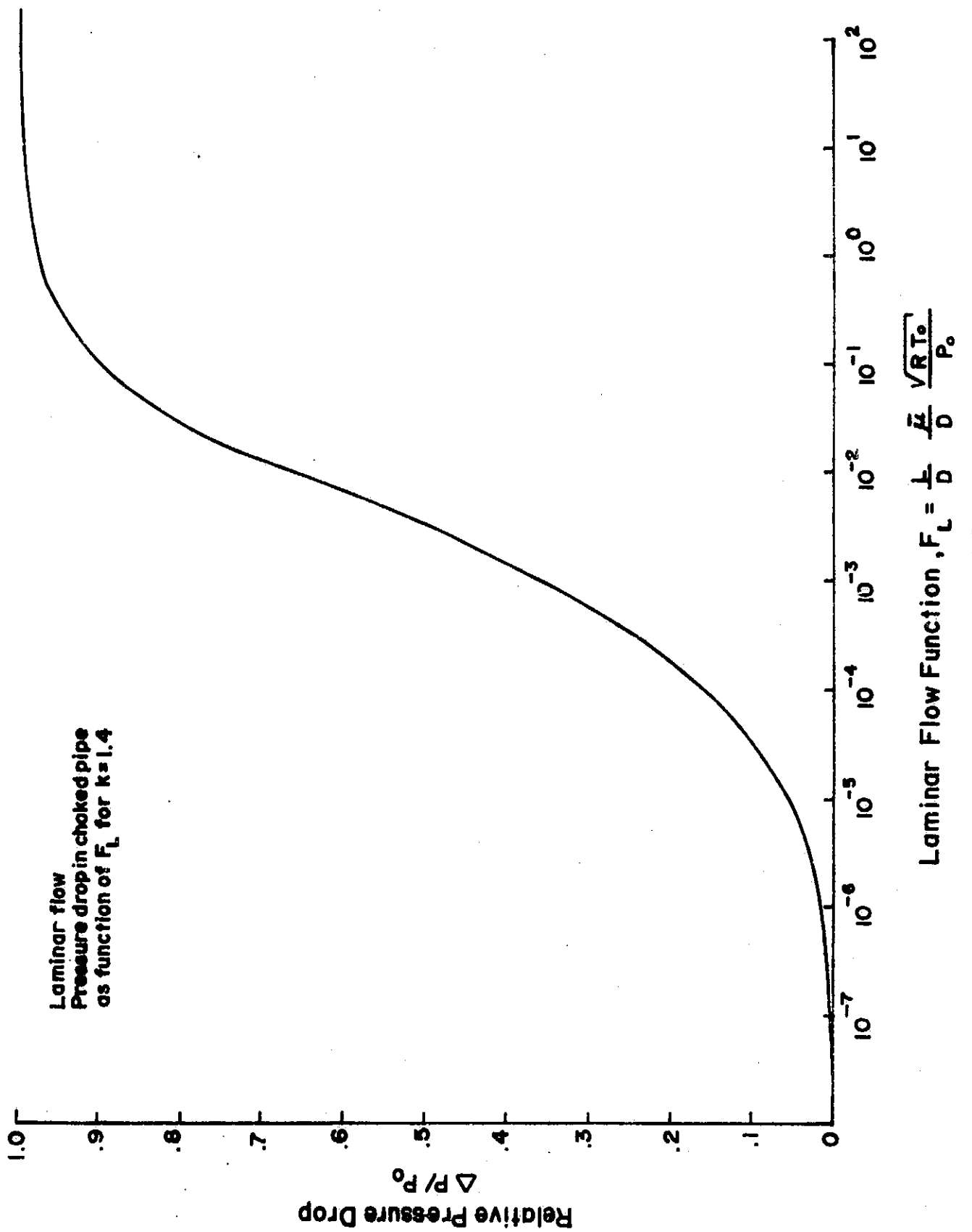


Figure 2-1

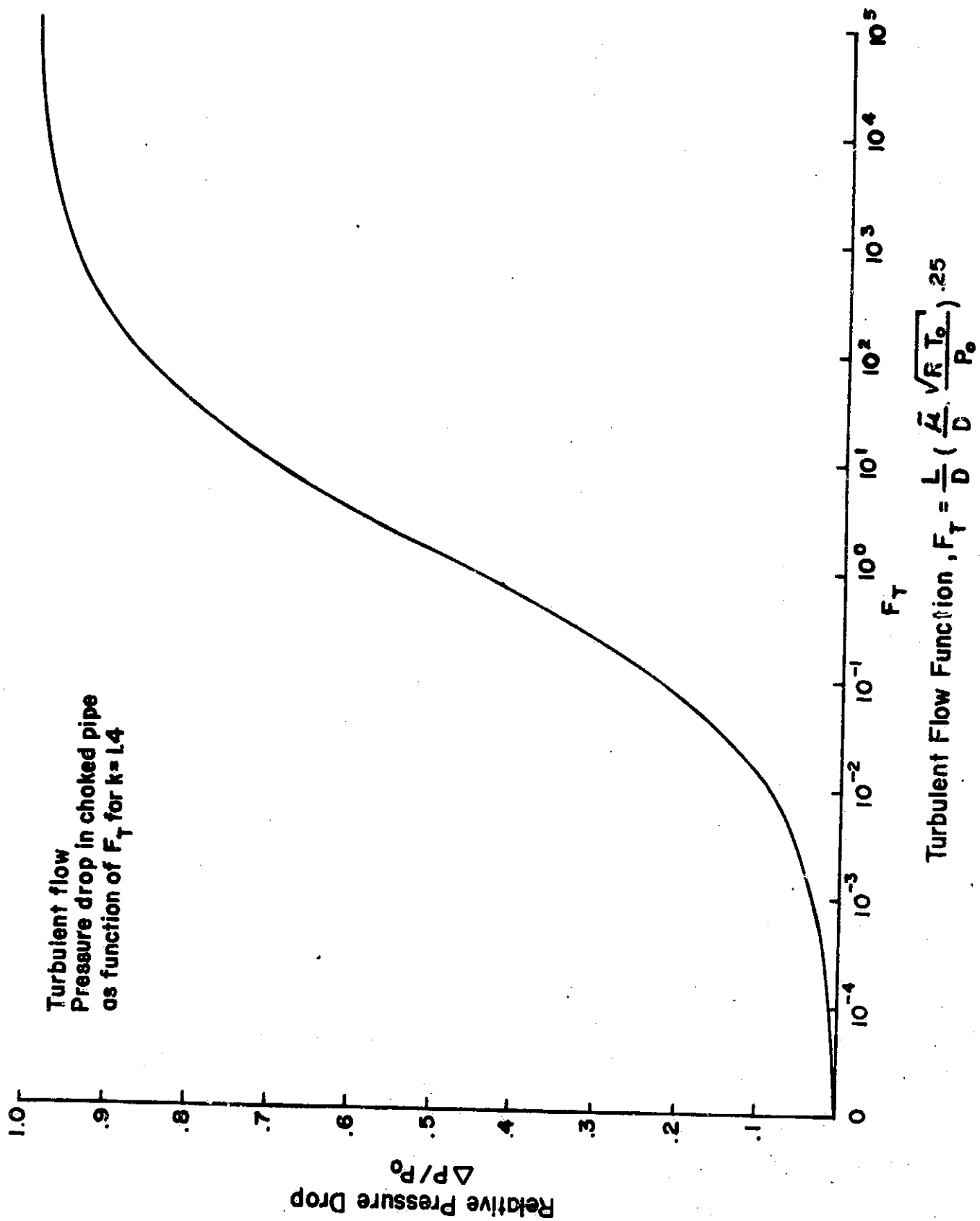


Figure 2-2

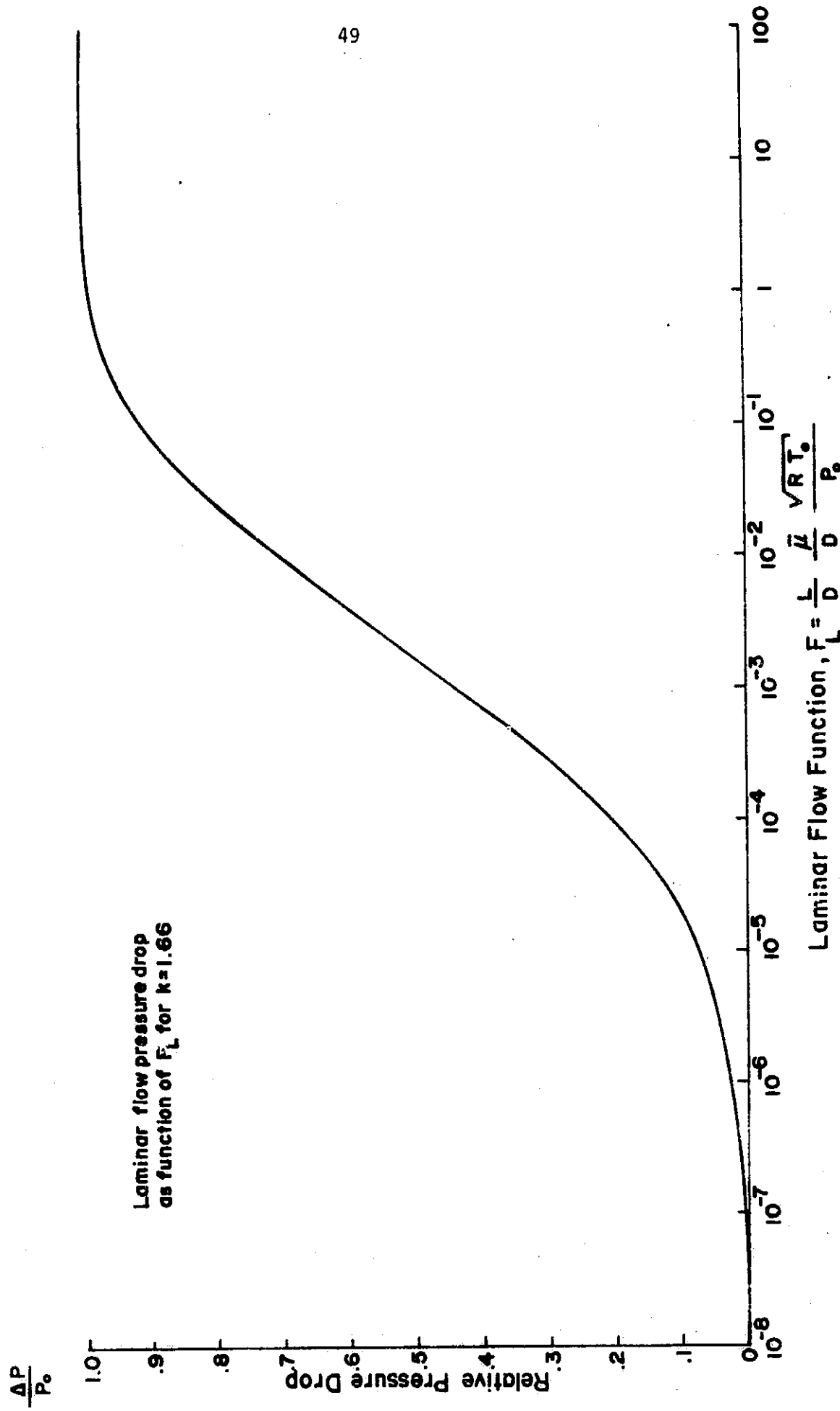


Figure 2-3

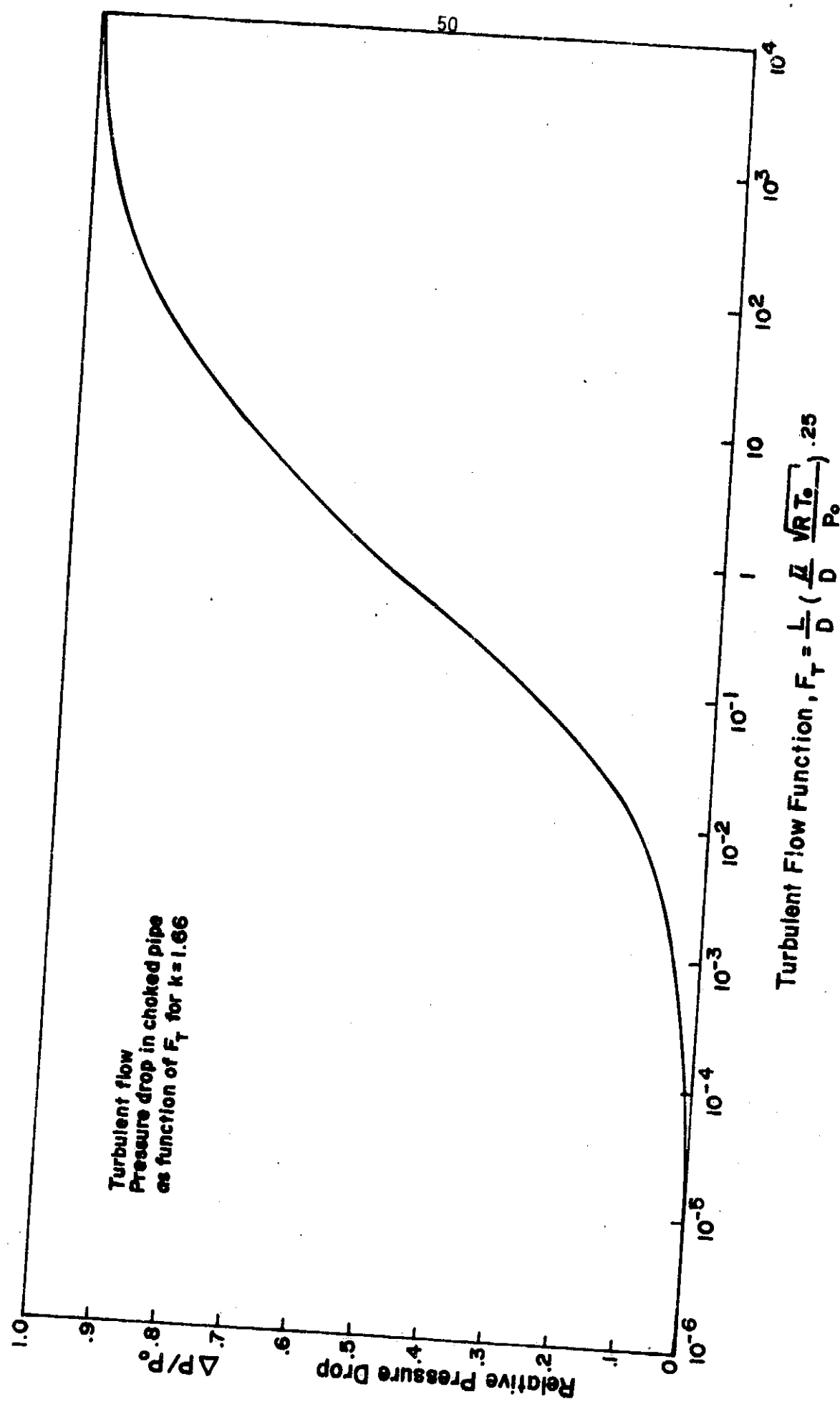


Figure 2-4

Entrance Mach Number and non-dimensional flow rate parameter for Laminar flow in choked pipe as function of F_L for $k = 1.4$

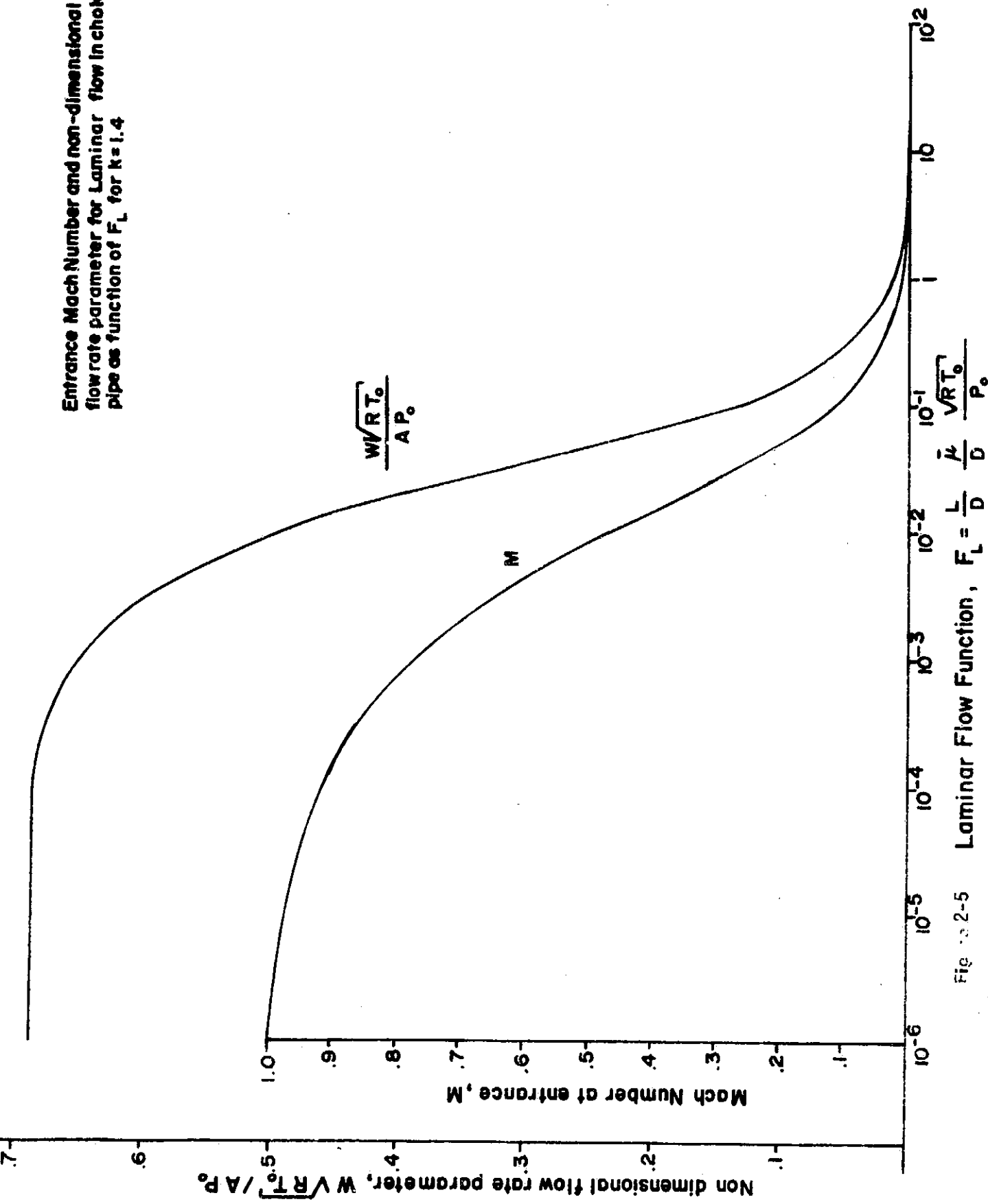


Fig. 2-5 Laminar Flow Function, $F_L = \frac{L}{D} \frac{\bar{\mu}}{D} \frac{\sqrt{R T_e}}{P_0}$

Entrance Mach Number and non-dimensional
flow rate parameter for turbulent flow in choked
pipe as function of F_T for $\kappa = 1.66$

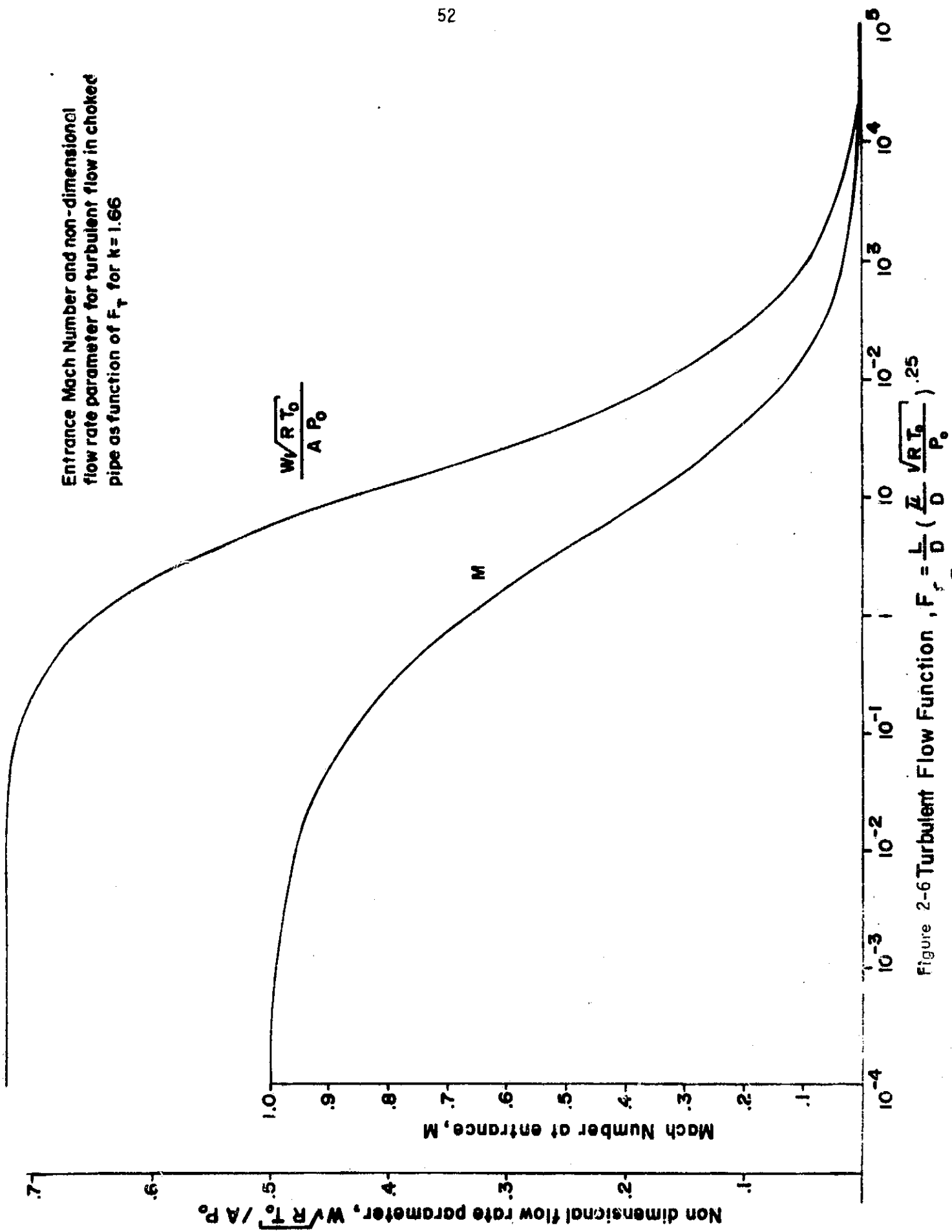


Figure 2-6 Turbulent Flow Function, $F_T = \frac{L}{D} \left(\frac{W\sqrt{RT_0}}{AP_0} \right)^{25}$

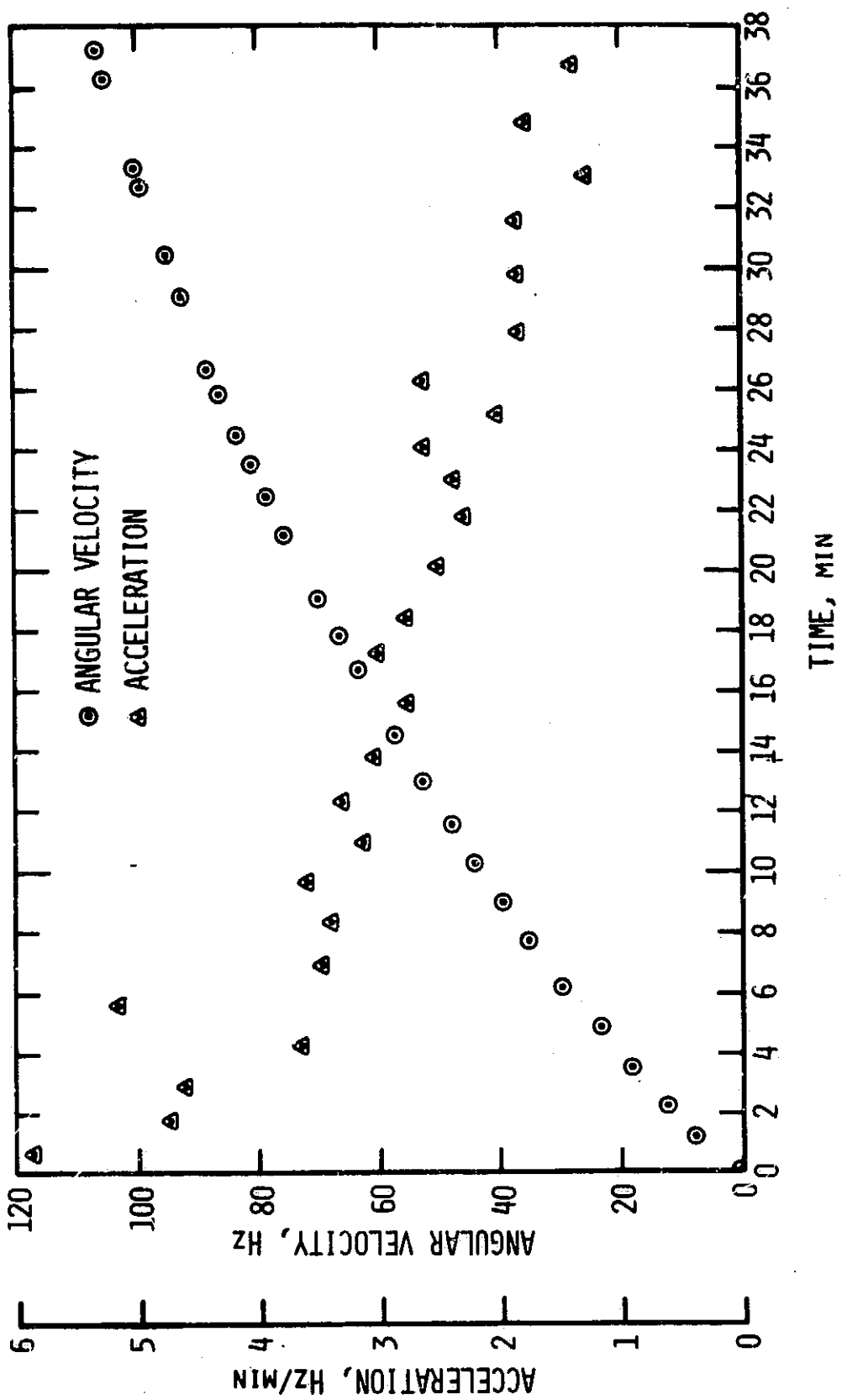


Figure 2-7 Spin Up Test of July 19, 1977 With a Quartz Rotor.

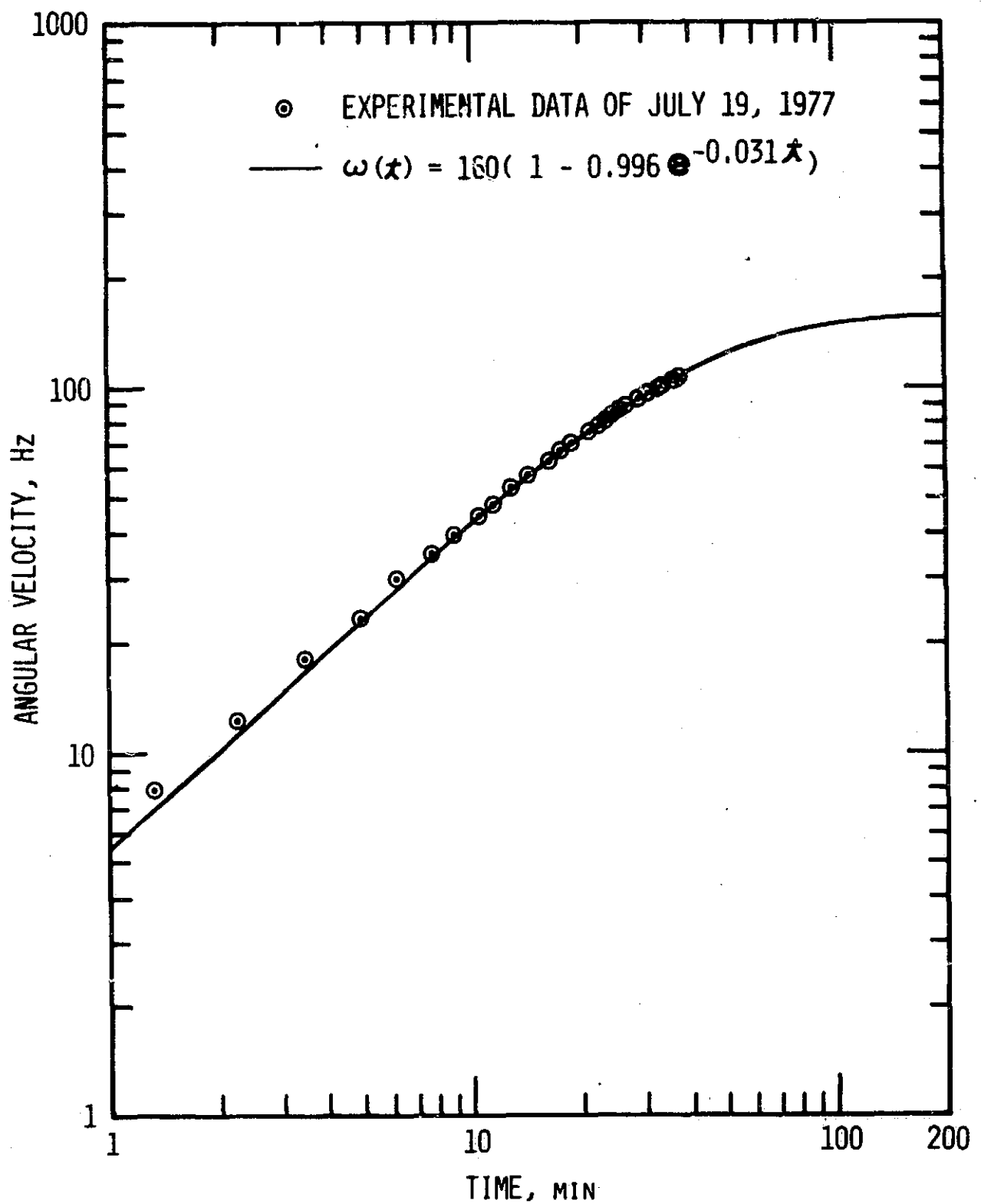


Figure 2-8 Fit of Experimental Data to Equation Describing the Spin History of the Gyro.

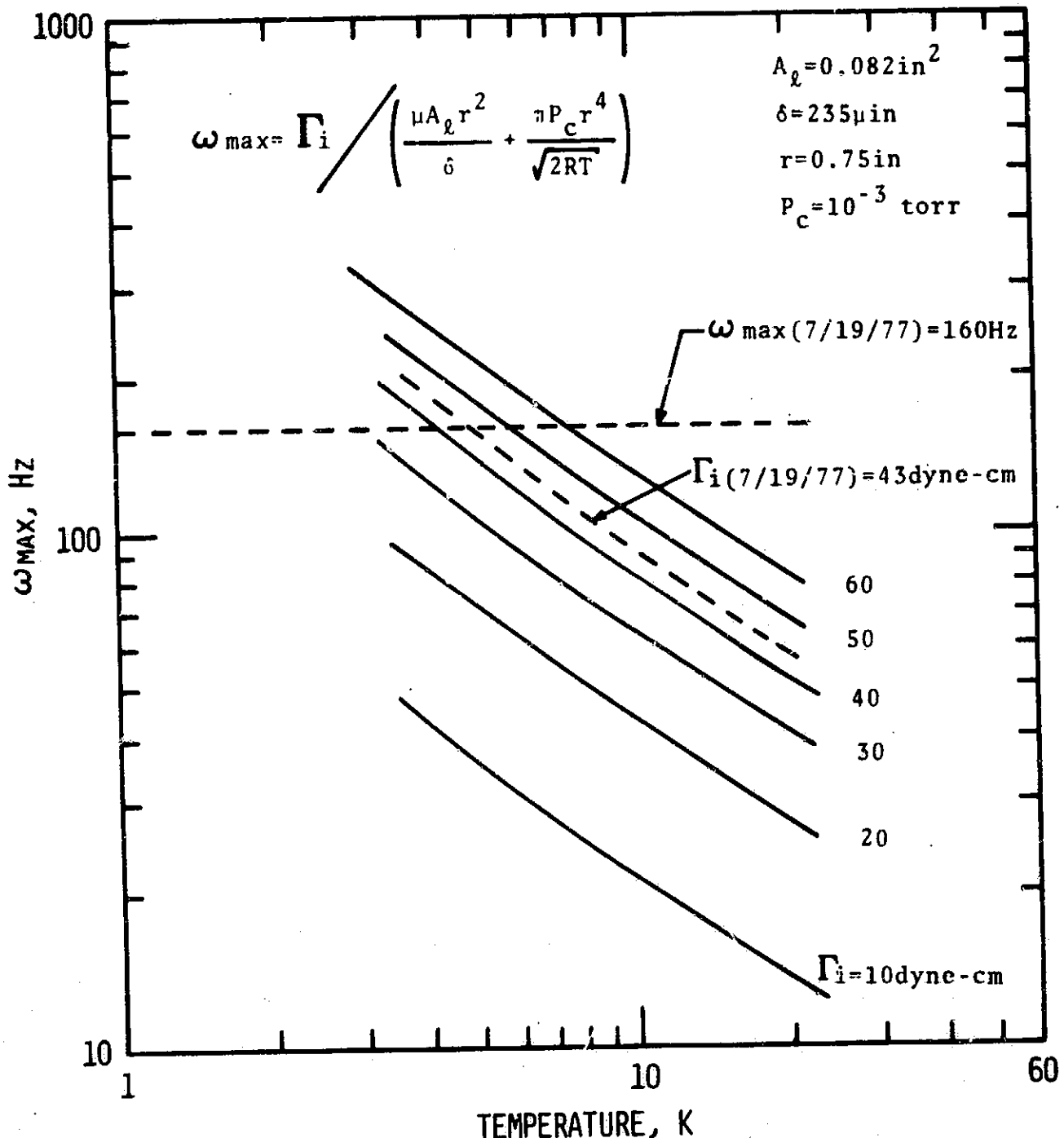


Figure 2-9 ω_{\max} as a Function of Temperature for Constant Values of Initial Torque.

Chapter 3 THEORY OF SUPER FLUID PLUG OPERATION

I. INTRODUCTION

The operating characteristics of a porous plug which has liquid helium on one side and which is pumped on under vacuum on the other side is discussed. Such a device has application to the containment of liquid helium in a zero gravity environment. The plug has the capability of acting as a phase separator and, to some extent, as a temperature control device.

The system to be considered in the work consists of a container of liquid helium which is well isolated. The only means for mass flow out of the container is through a plug made of porous material. The plug is assumed to have liquid helium on the container side while the other side of the plug is evacuated. In the experiment ran on earth under one g, the plug is situated on the bottom of the container. The physical system employed in the evacuation is found to be important to the plug operation. Three cases in particular will be considered: (1) perfect evacuation with zero pressure, (2) evacuation through an choked orifice, and (3) evacuation through a long, small diameter pipe with heating. The last case is the one most likely to occur in practice.

Two distinct ranges of temperature operation are of importance in describing plug flow. (1) Above $T = 2.172^{\circ}\text{K}$ and (2) Below $T = 2.172^{\circ}\text{K}$. The temperature 2.172°K is the point at which liquid helium changes from HeI which exists at the higher temperature range to a second liquid

phase HeII at the lower range of temperature. HeI is a normal liquid phase and the flow of this liquid is described by classical fluid flow relationships. In the HeII phase, however, the fluid exhibits super fluid properties which must be taken into consideration.

For purposes of describing the plug operation, the two-fluid model of the HeII phase is used. The two-fluid model considers HeII to consist of a super fluid component, ρ_s , and a normal fluid component, ρ_n , where the total density of the fluid, ρ , is given by

$$\rho = \rho_s + \rho_n$$

The ratio ρ_n/ρ drops from a value of one at the λ -point and asymptotically approaches zero at 0°K .

The fluid flow of HeII using the two-fluid model is described by the following set of Landau's equations (see for example R. J. Donnelly, Experimental Superfluidity, University of Chicago Press, 1967),

$$\rho_s \frac{\partial \vec{v}_s}{\partial t} + \rho_s (\vec{v}_s \cdot \nabla) \vec{v}_s = - \frac{\rho_s}{\rho} \nabla p + \rho_s SVT + \frac{\rho_n \rho_s}{\partial \rho} \nabla (\vec{v}_n - \vec{v}_s)^2 \quad (1)$$

$$\rho_n \frac{\partial \vec{v}_n}{\partial t} + \rho_n (\vec{v}_n \cdot \nabla) \vec{v}_n = - \frac{\rho_n}{\rho} \nabla p - \rho_s SVT$$

$$- \frac{\rho_n \rho_s}{\partial \rho} \nabla (\vec{v}_n - \vec{v}_s)^2 + \mu \nabla^2 \vec{v}_n \quad (2)$$

The first term on the right hand side represents the reaction of the fluid to pressure forces, the second term is associated with the thermo-mechanical effect, and the third term is a mutual friction dependent on

the motion of one component with respect to the other. Equation (2) contains a fourth term on the right hand side which represents the effect of viscosity. The flow equation for temperature above the λ point can be obtained from equation (2) for the case of $\rho_s = 0$ and $\rho_n = \rho$.

The flow equations are found to reduce considerably for the combination of steady state flow and small VT across the plug. These conditions are reasonable assumptions for plugs made with large pore ($5-10\mu$) material. For small pore material ($.5\mu$), the VT across the plug is found to be large. Also, small pore materials seem to exhibit time dependent behavior which may require non-steady state analysis.

In summary, the description of porous plug operation for liquid helium management is divided into the following items of importance.

1. Type of evacuation
 - a. perfect vacuum
 - b. through orifice
 - c. through pipe with heating
2. Temperature range
 - a. above λ -point
 - b. below λ -point
3. Simplifying assumptions
 - a. steady state
 - b. small VT
4. Velocity range of superfluid
 - a. less than critical velocity
 - b. greater than critical velocity

This report will consider the special case of small VT, steady state operation of a plug evacuated through an ideal orifice over the full temperature range. The results will be reducible to the case of a perfect vacuum evacuation. Future progress reports will consider the case of evacuation through a pipe with heating and large VT across the plug.

II. SMALL VT WITH EVACUATION THROUGH CHOKED ORIFICE

The model of the system to be described is shown in Figure 1. The flow through the orifice is linear in the pressure difference across the orifice. If the pressure downstream of the orifice is small compared to the pressure in the plenum, P_p , the mass flow per unit area through the orifice is given by

$$\dot{m}/A^* = F P_p \quad (3)$$

where \dot{m} is the mass flow rate, A^* is a flow area at the point that Mach Number M=1, and F is given for a choked orifice by

$$F = C_w \sqrt{\frac{1}{RT_p} - \frac{2}{\gamma+1}} \quad (4)$$

where C_w is a orifice discharge coefficient, γ is the ratio of specific heats, R is the gas constant of the gas and T_p is the temperature of the gas in the plenum. For pressure ratios across the orifice of .1 or less, the value of C_w is 0.85.

In normal operation, heat is transferred out of the container through the plug at a rate proportional to the conductivity across the plug. The heat comes from heat leaks into the container due to imperfect

ORIGINAL PAGE IS
OF POOR QUALITY.

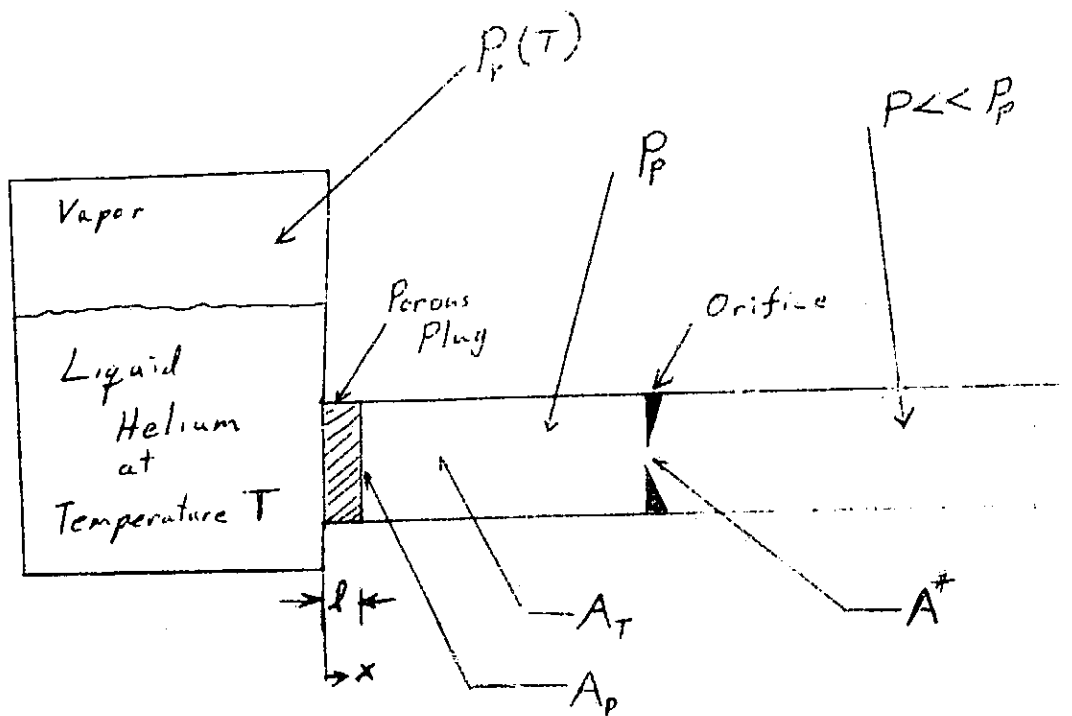


FIGURE 3-1 Model of Super Fluid Plug System Considered in Analysis

isolation or from heat given off by experimental equipment inside the container.

An analytic solution to equations (1) and (2) is obtained for the case of choked orifice and certain assumptions concerning the liquid flow in the plug. One simplification becomes apparent if equation (1) is added to equation (2). The result is

$$\rho_s \frac{\partial \vec{v}_s}{\partial t} + \rho_n \frac{\partial \vec{v}_n}{\partial t} + \rho_s (\vec{v}_s \cdot \nabla) \vec{v}_s + \rho_n (\vec{v}_n \cdot \nabla) \vec{v}_n = - \nabla p + \mu \nabla^2 \vec{v}_n \quad (5)$$

The right hand side of Equation (5) is the incompressible, steady-state Navier-Stokes equation for parallel flow. Parallel flow means that the flow has components in one direction only. If the left hand side of equation (5) can be neglected, the problem is greatly simplified. The first two terms of equation (5) are zero for steady-state conditions. The third and fourth terms are zero for the case of parallel flow and small temperature drop(based on continuity). The assumptions of parallel flow is justified even for flow in a porous material if one considers averages over regions that are large compared to the pore size. The continuity equation for the two-fluid model and parallel flow is

$$v_s \frac{\partial p_s}{\partial x} + \rho_s \frac{\partial v_s}{\partial x} + v_n \frac{\partial p_n}{\partial x} + \rho_n \frac{\partial v_n}{\partial x} = 0 \quad (6)$$

Although the flow is considered incompressible,

$$\rho_n + \rho_s = \text{constant} \quad (7)$$

the individual densities are a strong function of temperature as discussed earlier. For this reason, the derivatives of ρ_s and ρ_n may be finite if a temperature gradient exists. Since heat transfer is taking place, one can neglect these derivatives only if the temperature gradient is small enough to make the resultant density gradient negligible. This condition can be met for plugs with large pores except near T_λ where the density changes are large with respect to temperature. The large pore plugs have a high effective thermal conductivity and therefore a small gradient of temperature as will be discussed later.

Under the assumption of small ΔT and parallel flow, equation (5) becomes

$$\nabla p = \mu \nabla^2 \vec{v}_n \quad (8)$$

where the velocity v_n is determined completely by the pressure drop. If the plug were constructed of smooth channels, such as a bundle of capillary tubes of radius R , the exact solution to the above for laminar pipe flow could be employed to find the volume flow rate given by

$$Q_n = \frac{\pi R^4}{8\mu} \cdot \left(\frac{dp}{dx} \right) \quad (9)$$

which shows that the flow rate is a linear function of the pressure drop. The plugs being considered by NASA at this time, however, are made of packed granular material which cannot be considered to have smooth passages.

For flow through porous material, a relationship similar to equation (9) is available given by Darcy's law (see Muskat, Flow of Homogeneous Fluids)

$$v_n = - \frac{k}{\mu} \frac{dp}{dx} \quad (10)$$

where k is called the permeability of the porous material. Values of k must generally be determined experimentally since reliable theory has not been developed for the irregularly shaped granuals contained in most porous substances. A good approximation, however, can often be made by use of Kozeny's equation

$$k = \frac{1}{5} \frac{p^3}{(1-p) s} \quad (11)$$

where p is the fractional porosity and s is the total surface area of the particles contained in a unit volume of the medium. Fractional porosity is defined as the fractional volume of voids per unit total volume. This can be obtained by weighing a sample made of granuals of known density. The value of s is related to the size of the granuals which varies considerably in most materials.

The important result to this point is that the normal fluid velocity is a function of the pressure drop as given in equation (10). For the experimental apparatus under consideration, the pressure on the liquid side of plug is the vapor pressure associated with the temperature of the liquid. The liquid head above the plug will also contribute to the pressure. The pressure drop across the plug is then given by

$$-\Delta p = P_v(T) + P_h - P_p \quad (12)$$

where $P_v(T)$ is the vapor pressure at temperature T , P_h is the head pressure and P_p is the plenum pressure on the downstream side of the

plug. The pressure P_p is given as a function of mass flow rate in equation (3).

Considering the mass flow rate at the plug which is given by

$$\frac{m}{A_p} = \rho_s v_s + \rho_n v_n \quad (13)$$

where A_p is the area of pores available for flow of liquid in the plug and the densities are for the liquid state. Equation (3) then becomes

$$\rho_s v_s + \rho_n v_n = F P_p \quad (14)$$

and, since

$$m = F A^* P_p$$

then

$$P_p = \frac{A}{A^* F} (\rho_s v_s + \rho_n v_n) \quad (14a)$$

Letting λ be the length of the plug, dp/dx can be written as $\Delta p/\lambda$.

Equation 10 can now be written, using equation (12) and (14a)

$$v_n = \frac{k}{\mu z} \left[p_v(T) + p_h - \frac{A}{A^* F} (\rho_s v_s + \rho_n v_n) \right] \quad (15)$$

which provides a relationship between $\rho_s v_s$ and $\rho_n v_n$ which will be used later.

In order to be consistent with the assumptions of parallel flow and small temperature gradient as used previously, Equation (1) should be written with the left hand side zero and the last term on the right hand side also neglected. Therefore, equation (1) becomes

$$\frac{\rho_s}{\rho} \nabla P = \rho_s S \nabla T$$

or

$$\nabla P = \rho S \nabla T \quad (16)$$

The gradient of T required in equation 16 is a function of temperature range (i.e., above or below T_λ), the plug material, and the pore size as will be discussed.

Heat is transferred across the plug in proportion to the temperature drop and the thermal conductivity of the plug given by

$$\frac{d}{A_T} = K \nabla T \quad (17)$$

where A_T is the total area of the plug and where K is the thermal conductivity of the plug which has contributions from both the liquid K_L , and the solid materials, K_m , given by

$$K = K_m \frac{A_m}{A_T} + K_L \frac{A_L}{A_T} \quad (18)$$

where A_m and A_L are the respective areas of the two materials. Values of K_m as a function of temperature are available in the literature.

Donnelly discusses the effective thermal conductivity of liquid helium below T_λ . Since entropy can only be transported by the normal fluid component, the flow of heat then is restricted if the normal fluid flow is restricted. For the small openings that are encountered in porous materials, viscous effects strongly influence the flow of the normal fluid. Therefore, the smaller the flow spacing, the smaller the thermal conductivity. Donnelly gives as a result, for below T_λ

$$K_L = \frac{\rho^2 S^2 T d^2}{12\mu} \quad (19)$$

where S is the entropy. Since S is a strong function of temperature, K_L , also becomes a strong function of temperature as evidenced by the approximation

$$K_L \approx 1.2 \times 10^5 T^{12.2} d^2 \quad (20)$$

Heat conductivity of helium at 3.3°K is only

$$K_L (3.3^\circ\text{K}) = 6 \times 10^5 \text{ cal/deg/cm/sec} \quad (21)$$

Large pore size then results in extremely high thermal conductivities below T_λ which tends to be the dominant term in equation 18.

The heat that is transferred across the plug is liberated in transforming the liquid into a gas at the surface of the plug. The heat flow then is related to the mass flow rate and the latent heat of vaporization, L , of the helium given by

$$\frac{q}{A_T} = L \frac{\dot{m}}{A_T} \quad (22)$$

Equating the heat flow expression from equation (17) and (22), we obtain

$$K \nabla T = L \frac{\dot{m}}{A_T} \quad (23)$$

Substituting for ∇T in equation (16) using the above we get

$$\nabla P = \rho S \left(\frac{L}{K} \frac{\dot{m}}{A_T} \right) \quad (24)$$

Using equation (12) and (13), and (14) in equation (24).

$$\frac{p_v(T) + p_h - \frac{1}{F} (\rho_s v_s + \rho_n v_n) \frac{A_p}{A^*}}{\ell} = \rho_s \frac{L}{K} (\rho_s v_s + \rho_n v_n) \frac{A_p}{A_T} \quad (25)$$

This equation is solved for \dot{m} directly

$$\frac{\dot{m}}{A_T} = \frac{p_v(T) + p_h}{\frac{\rho S L}{K} + \left(\frac{1}{F A^*} \right)} \quad (26)$$

Equation (26) gives the flow rate through the plug as a function of temperature of the liquid helium. These results are not the same as obtained by Selzer, Fairbank, and Everett given by

$$\dot{m} = \frac{\Delta P K}{\rho S L} \quad (27)$$

Equation (26) is seen to reduce to equation (27) for the special case of $1/F = 0$ which corresponds to the case of zero pressure on the downstream side of the plug. Zero pressure is, however, an unrealistic assumption for laboratory systems. (A factor of length, L/A , is evidently missing from equation (27)).

CRITICAL VELOCITY LIMITING

Equation (26) applies only for superfluid velocities below the critical velocity. In order to assess the validity of this solution, the superfluid velocity, v_s , must be obtained to compare with the critical velocity, v_c . If the critical velocity is reached, another method of solution must be employed.

In order to obtain a solution for v_s and v_n , equations (26) and equation (15) are solved simultaneously. Substituting for \dot{m}/A_T from

equation (26) into equation (15), we get

$$v_n = \frac{k}{\mu \lambda} \left[1 - \frac{1}{\frac{\rho S L \lambda}{K} \left(\frac{F A^*}{A_T} \right) + 1} \right] (P_v(T) + P_h) \quad (28)$$

which gives the solution for v_n . This equation can be rewritten in a form similar to equation (26)

$$v_n = \frac{\frac{\rho S L k}{\mu K}}{\frac{\rho S L \lambda}{K} + \left(\frac{F A^*}{A_T} \right)} (P_v(T) + P_h) \quad (29)$$

the velocity of the super fluid component is obtained using equation (29) with equation (26). The result is

$$v_s = \frac{\frac{A_T}{A_p} \frac{1}{\rho_s} \left(1 - \frac{\rho_n \rho k S L A_p}{K \mu A_T} \right)}{\left[\frac{\rho S L \lambda}{K} + \frac{1}{\left(\frac{F A^*}{A_T} \right)} \right]} (P_v(T) + P_h) \quad (30)$$

The normal velocity is seen to always be a positive number while v_s may become negative if

$$\frac{\rho_n \rho k S L A_p}{K \mu A_T} > 1 \quad (31)$$

If the superfluid flow velocity should become greater than the critical velocity, equation 1 must be modified to include a viscous type term in the superfluid component. A solution for this case has not as yet been

developed since it was found that for the pore sizes and pressures under consideration, critical velocity was not reached. Critical velocity would be expected to become important, however, for larger sizes of pores and much higher pressure heads.

ABOVE T_λ

The flow rate above the transition temperature consists of only the normal fluid which is governed by Darcy's law as mentioned earlier. The flow is still effected by the orifice, however. Equation (12) for the pressure drop remains the same and equation (14) becomes, for flow of vapor,

$$F P_p = \frac{\dot{m}}{A^*} \quad (32)$$

Using equation (10) and (12) with the above we get

$$\begin{aligned} P_p &= \frac{A}{A^* F} (\rho v) \\ v &= \frac{k}{\mu \ell} (P_v(T) + P_h - \frac{A_p \rho}{A^* F} v) \end{aligned} \quad (33)$$

where ρ is the density of the liquid helium.

Solving for P_v , the flow above T_λ is given by

Above T_λ results

$$\begin{aligned} \frac{\dot{m}}{A_T} &= \frac{P_v(T) + P_h}{\mu \ell A_T} \\ &\quad \frac{1}{\rho k A_p} + \left(\frac{F A^*}{A_T} \right) \end{aligned} \quad (34)$$

SUMMARY OF BELOW T_λ RESULTS

Below T_λ

$$\frac{A_p}{A_T} (\rho_s v_s + \rho_n v_n) = \frac{\dot{m}}{A_T} = \frac{P_v(T) + P_h}{\frac{\rho S L \ell}{K} + \left(\frac{1}{F A^*} \right)} \quad (26)$$

where

$$v_n = \frac{\frac{\rho S L \ell k}{\mu K}}{\frac{\rho S L \ell}{K} + \left(\frac{1}{F A^*} \right)} (P_v(T) + P_h) \quad (29)$$

and

$$v_s = \frac{\frac{A_T}{A_p} \frac{1}{\rho_s} \left(1 - \frac{\rho_n \rho k S L A_p}{K \mu A_T} \right)}{\frac{\rho S L \ell}{K} + \left(\frac{1}{F A^*} \right)} (P_v(T) + P_h) \quad (30)$$

Comparison with Experiment

The equations given above were evaluated over the temperature range of interest ($l \cdot K$ to T_λ) for a number of plug parameters. The parameters associated with plugs being tested by Dr. Urban at MSFC were employed in the analysis and the comparison of these analytic results with the experimental results is presented here. The purpose of this discussion is to also describe the methods used to obtain some of the important parameters needed in the calculation. Some of the basic properties of a few of the plugs to be tested by Dr. Urban are given in Table I.

Table 3-1

Material	Thickness, l	Diameter*	Porosity, P	Labeled Pore Diameter
Nickel	.00630 m	.04515 m	.384	10 micron
Stainless Steel	.00630 m	.04510 m	.311	10 micron
Copper	.00645 m	.04520 m	.467	10 micron
Ceramic	.00660 m	.04525 m	.677	10 micron
Ceramic	.00650 m	.04523 m	.548	.5 micron

*The diameters listed are for the unmounted plug. The effective diameter of the plug in the holder is the same for all the plugs tested and is 0.0437 m.

Porosity Determination

The values of porosity listed in Table I were arrived at by weighing the plug on a balance to obtain the bulk density, ρ_b , of the plug given by

$$\rho_b = \frac{\text{mass}}{\pi r^2 l} \quad (35)$$

The porosity of the plug is then found using the density of the material, ρ_m , in the following equation

$$P = 1 - \frac{\rho_b}{\rho_m} \quad (36)$$

The densities employed in determining the porosity were approximate values given in Table II.

Table 3-2 Density of Plug Materials

Material	ρ_m (gm/cm ³)
Nickel	8.902
Stainless Steel	7.9
Copper	8.96
Ceramic, Al ₂ O ₃	3.965

Permeability Determination

The permeability of the porous plugs were determined in Helium gas flow tests ran at room temperature by Dr. Katz. The tests consisted of measuring the time for the plug to pass a measured volume of Helium gas for a measured pressure drop across the plug. The results revealed a linear relationship between volume of gas per unit time versus pressure drop over a range of pressure drops from 1/2 to 4 psi. The results of these measurements are given in Table 3-3.

Table 3-3 Flow Rate Per Unit Pressure Drop

Material	Pore Size	$\Delta F/\Delta P$
Nickel	10 Micron	31.45 scc/sec/psi
Ceramic	10 Micron	18.64 scc/sec/psi
Ceramic	.5 Micron	0.448 scc/sec/psi
Ceramic	3 Micron	6.23 scc/sec/psi

The permeability of the plug is defined using Equation 10

$$k = \frac{v \mu}{dp / dx} \quad (37)$$

Since the flow experiment measures volume flow rate rather than the velocity called for in Equation 37, multiply the right hand side by A_T/A_T to obtain

$$k = \left(\frac{v A_T}{d p} \right) \frac{\mu dx}{A_T} \quad (38)$$

where the term in the bracket corresponds to the measurements given in Table III. Taking dx to be the plug length (see Table I), the area to be based on a diameter of 0.0437 m (see note with Table I), and the viscosity of the helium gas to be

$$\mu = 1.953 \times 10^{-5} \text{ n} \cdot \text{sec/m}^2$$

the permeability values obtained are given in Table IV.

Table 3-4 Permeability Values

Material	Pore Size	Permeability, k
Nickel	10 micron	$3.7716 \times 10^{-13} \text{ m}^2$
Ceramic	10 micron	$2.2354 \times 10^{-13} \text{ m}^2$
Ceramic	.5 micron	$5.3726 \times 10^{-15} \text{ m}^2$

Effective Orifice Parameter

Equation 3 is a linear relationship between the flow rate and the back pressure developed on the gas side of the plug. This relationship is strictly valid only for a sharp edged orifice. The pumping line employed in the experimental apparatus to be considered here has a minimum diameter of 1/4 inch with many turns and a length of over six feet before expanding to a larger diameter. The pumping line reaches room temperature soon after leaving the dewar.

The restriction to the gas flow caused by the small diameter, long tube with high heating is represented in this analysis as a single sharp edged orifice. Modeling the pumping line restriction as a sharp edged orifice is not particularly accurate but does represent an important part of the plug system in a simple manner. Future work will incorporate a more accurate representation of the pumping line restriction which calls for an equation of the form,

$$\dot{m} = G P_p^2 \quad (39)$$

instead of the linear relationship given in Equation 3. The F factor in Equation 3 is a function of temperature on the gas side of the plug as given in Equation 4. This temperature dependence will be ignored in the present treatment since the error committed is less than the error of using Equation 3 rather than Equation 39.

The determination of F and A^* cannot be made separately but an effective orifice parameter can be found by writing Equation 3 as

$$\dot{m}/A_T = \left(\frac{FA^*}{A_T} \right) P_p \quad (40)$$

In Equation 40, the values of m , A_T and P_p are measurable quantities allowing the determination of the effective orifice parameter, placed in brackets in Equation 40. In one of the first plug experiments at MSFC, the values of m , A_T and P_p were monitored in order to obtain a value of FA^*/A_T . From these measurements the following value was obtained

$$\frac{FA^*}{A_T} = 1.0412 \times 10^{-6} \frac{\text{Kg}}{\text{m} \cdot \text{sec}} \quad (41)$$

which is representative of the pumping line restriction at temperature near 1.6°K where the pumping rate was found to be near 500 scc/min.

Liquid Helium Properties

The following liquid helium properties are required for the computation of plug flow rates.

P_V = Vapor pressure

S = Entropy

L = Latent heat of vaporization

ρ_n = Density of normal fluid component

ρ_s = Density of super fluid component

ρ = Total density of fluid = $\rho_s + \rho_n$

μ = Viscosity of the normal fluid component

The vapor pressure is obtained from a curve fit relationship provided by NBS which gives the vapor pressure in units of n/m^2

$$P_V = 1.33322 \times 10^5 \exp(a_1 T + a_2 + a_3/T + a_4/T^2 + \dots + a_{14}/T^{12}) \quad (42)$$

where

$$\begin{aligned}a_1 &= -49.510540356 \\a_2 &= 651.92364170 \\a_3 &= -3707.5430856 \\a_4 &= 12,880.673491 \\a_5 &= -30,048.545554 \\a_6 &= 49,532.267436 \\a_7 &= -59,337.558548 \\a_8 &= 52,311.296025 \\a_9 &= -33,950.233134 \\a_{10} &= 16.028.674003 \\a_{11} &= -5354.1038967 \\a_{12} &= 1199.031906 \\a_{13} &= -161.46362959 \\a_{14} &= 9.8811553386\end{aligned}$$

The other liquid helium properties were obtained from 12 point orthogonal polynomial least squares curve fits of values given in Donnelly, Experimental Superfluidity, 1967. The values used are given in Table V. The density of the super fluid, ρ_s , and the total density, ρ , are obtained from the values of ρ_n and the ratio of ρ_n to ρ given in the table. Therefore,

$$\rho_s = \rho_n / (\rho_n/\rho) - \rho_n \quad (43)$$

Table 3-5 Liquid Helium Properties

T Temperature °K	S Entropy j/gm°K	L Latent Heat of Vaporization cal/mole	ρ_n Normal Fluid Density gm/cm ³	ρ_n/ρ Ratio of Normal to Total Fluid Density	μ Viscosity of Normal Fluid Micro-poise
1.1	.0304	19.75	.00212	.0146	26.8
1.2	.0523	20.30	.00405	.0279	17.5
1.3	.0853	20.80	.00686	.0473	15.2
1.4	.132	21.20	.01100	.0743	14.1
1.5	.197	21.48	.01650	.1140	13.5
1.6	.284	21.78	.02465	.1700	13.2
1.7	.398	22.05	.03460	.2380	13.0
1.8	.535	22.20	.04720	.3250	13.0
1.9	.709	22.26	.06240	.4290	13.4
2.0	.929	22.18	.08070	.5540	14.9
2.1	1.215	22.02	.10550	.7230	18.6
2.2	1.600	21.87	.14600	1.0000	28.0

and

$$\rho = \rho_s + \rho_n \quad (44)$$

Thermal Conductivity

Values of the thermal conductivity of the plug materials were obtained from National Bureau of Standards, NBS Monograph 131, Thermal Conductivity of Solids at Room Temperature and Below, 1973. At the temperatures under consideration, the material thermal conductivities are found to vary in a linear manner on a log-log plot of conductivity and temperature. The thermal conductivity is then written as

$$K_m = \text{EXP} (A + B \log T) \quad (45)$$

where A and B are the parameters of the straight line curve fit.

Thermal conductivity is found to be a strong function of the impurities or the alloy of the material under consideration. Table VI gives a sampling of the thermal conductivities of various materials at 2°K. Figure 1 shows the variation of thermal conductivity with respect to temperature for a number of materials.

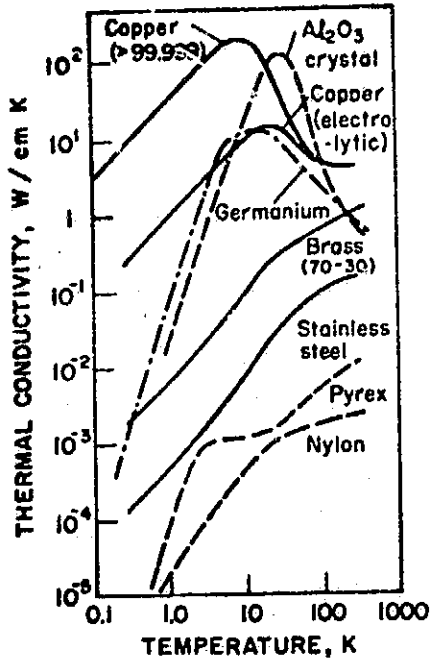


Figure 3-1

Thermal conductivity variations of metals and alloys (—), electrical insulators (---), and a semi-conductor (-·-·-).

Table 3-6 Thermal Conductivity of Materials at 2°K

Material		K_m , (W/m · °K)
Nickel	-high purity RRR = 670 -Matthey 37043, 99.995 pure -.16 atomic percent Cu	.550.0 47.5 20.0
Silver	-better than 99.99% pure	370.0
Gold	-99.999% pure with traces of Cu, Ag, Si, and Pb. RRR = 536	125.0
Copper	-.003% Ag, Ni, and Pb -Commercial wire RRR ≈ 85	118.0 260.0
Stainless Steel	-Extrapolation of Mean of number of stainless steels	≈ 0.10
Alumina Al_2O_3	-Sintered to within 5% of crystal density, extrapolated value -Doped with .1 (weight) $M_n O_2$	≈ .3 13.5
Fused Quartz	-Extrapolated from 100°K	≈ .08
Aluminum	-99.998% pure -Alloys (extrapolated)	480.0 ≈ 2.0
Titanium	-99.99% pure -98 % pure	≈ 1.0 ≈ .4

For comparison, Table VII gives the effective thermal conductivity of liquid helium at 2°K calculated using Equation 19.

Table 3-7 Thermal Conductivity of Liquid Helium at 2°K
(Equation 19)

Pore Size (microns) of flow passage	K L	W m	$^{\circ}K$
0.1		20.46	
0.5		511.54	
1.0		2,046.2	
5.0		51,154.0	
10.0		204,620.0	

The thermal conductivity of the liquid is seen to be generally higher than the material values given in Table VI except for pore sizes less than .5 micron in diameter.

The thermal conductivities of the porous plug materials are expected to be less than the bulk material because of the granular structure of the plug. Since thermal conductivity measurements were not made of the porous materials used in the plug tests, the bulk properties are employed in the analysis with the realization that these conductivities are likely higher than that of the porous material. The error made in using the higher conductivity values is not important for large pore plugs since the liquid helium thermal conductivity dominates the total conductivity. For cases in which the conductivity of the plug material is important (for pore sizes less than 0.5 micron), better values of thermal conductivity are needed in order to accurately predict the plug operation. While the relationships used here are expected to be in error in absolute value, the variation with respect to temperature is represented. The characteristics of small-pore-size plugs revealed in experiments may yield improved values of thermal conductivity when such results are compared with those predicted.

In view of the lack of porous material conductivity information as discussed above, curve fit parameters A and B were derived to represent a number of different materials. These values are given in Table VIII.

Table 3-3 Curve Fit Parameters for Thermal Conductivity *

Material Represented	A	B	$K_m (2^{\circ}\text{K}), \text{W}/\text{m}^{\circ}\text{K}$
Nickel - high purity	-.17712	.78873	144.7135
Aluminum Alloy	-4.8655	1.0269	1.5706
Copper	.2332	1.008	253.93
Alumina (Al_2O_3)	-3.141	1.348	11.
Beryllium Oxide (BeO)	-9.388	2.817	.059
Stainless Steel	-.8011	1.239	105.94
Quartz	-8.087	.8472	.055

*Values of A and B listed here, when used in Equation 45, will give thermal conductivity in units of $\text{W}/\text{cm}^{\circ}\text{K}$.

Area of Pores, A_p , and Area of Material, A_m

The effective area available for flow of liquid helium is obtained in the following derivation. Let the flow passages for the liquid helium be approximated by straight tubes of constant diameter. If each tube were to have the diameter of the pore size of the plug, then each tube would have an empty volume of

$$\text{Volume of one flow tube} = \pi \left(\frac{d}{2}\right)^2 l \quad (46)$$

If it is assumed that the flow tubes comprise all of the empty space of the plug, the total volume of voids, V_v , is

$$V_v = N \pi \left(\frac{d}{2}\right)^2 l \quad (47)$$

where N is the number of flow tubes. The value of N for a particular plug is found from the porosity measurements as follows. Since porosity is defined as

$$P = \frac{V_v}{V_b} \quad (48)$$

where V_b is the bulk volume of the plug. The value of N is then found from Equations 47 and 48

$$N = \frac{P V_b}{\pi \left(\frac{d}{2}\right)^2 l} \quad (49)$$

The total area of pores is found to be

$$A_p = N \pi \left(\frac{d}{2}\right)^2 = \frac{P V_b}{l} = \frac{P A_T l}{l} \quad (50)$$

The following expressions are therefore obtained

$$A_p = P A_T \quad (51)$$

and

$$A_M = A_T - A_p = (1-P) A_T \quad (52)$$

These estimates of A_p and A_M will be employed in the relationships describing the liquid helium flow in porous materials.

Pore Size Estimation

The size of the pores in the porous plugs tested are not uniform as evidenced by electron microscope pictures made of a number of the plugs. The labeled values of pore size are very approximate and is meant as only an estimate of the pore size. Since pore size is required in the evaluation of the equations presented here, it was decided to relate the pore size to the measured value of permeability rather than use the labeled value.

The permeability measurements given in Table III were least squares fit with respect to the labeled pore size. A linear curve fit was employed with the result

$$d = (\Delta F / \Delta P) / 2.5 \quad (53)$$

where d is the pore diameter (assumed to have a circular cross section) and $\Delta F / \Delta P$ corresponds to the room temperature helium gas flow given in Table III in units of standard cubic centimeters per second per psi of pressure drop (SCC/SEC/psi). The value of d determined using Equation 46 will be given in units of microns.

Results

The above relationships were evaluated on the UAH Univac 1108 computer. The computations were performed using the international system of units. The flow rates were then converted to units of Standard Cubic Centimeters per Minute (SCC/M) for ready comparison with the experimental measurements which were made in those units. Table IX gives the results for the first plug tested which was nickel having the properties listed with the table. Table X gives results of the 10 micron ceramic and Table XI gives results for .5 micron ceramic.

Table 3-9 Results for Nickel Plug (10 Micron)

Material = Nickel

Porosity = .38411

Pore Size = 12.58

Thickness = .0063 m

Thermal Conductivity at 2°K = 144 W/

Permeability = $3.77 \times 10^{-13} \text{ m}^2$

Temperature °K	Flow Rate SCC/M	v_n m/sec	v_s m/sec
1.1	20.3	.538 $\times 10^{-5}$.653 $\times 10^{-6}$
1.2	43.6	.116 $\times 10^{-4}$.127 $\times 10^{-5}$
1.3	84.4	.152 $\times 10^{-4}$.237 $\times 10^{-5}$
1.4	150.7	.176 $\times 10^{-4}$.432 $\times 10^{-5}$
1.5	251.7	.191 $\times 10^{-4}$.761 $\times 10^{-5}$
1.6	398.1	.201 $\times 10^{-4}$.130 $\times 10^{-4}$
1.7	601.0	.208 $\times 10^{-4}$.216 $\times 10^{-4}$
1.8	872.3	.213 $\times 10^{-4}$.356 $\times 10^{-4}$
1.9	1,223.3	.214 $\times 10^{-4}$.599 $\times 10^{-4}$
2.0	1,663.8	.210 $\times 10^{-4}$.106 $\times 10^{-3}$
2.1	2,200.0	.201 $\times 10^{-4}$.229 $\times 10^{-3}$
2.16	2,568.0	.192 $\times 10^{-4}$.563 $\times 10^{-3}$

Table 3-10 Results for Ceramic Plug (10 micron)

Material = Ceramic

Porosity = .677

Pore Size = 7.456 micron

Thickness = .0066 m

Thermal Conductivity at 2°K = 11 W/m °K

Permeability = $2.2354 \times 10^{-13} \text{ m}^2$

Temperature °K	Flow Rate SCC/M	V_n m/sec	V_s m/sec
1.1	20.0	.113 x 10^{-4}	.241 x 10^{-6}
1.2	43.4	.142 x 10^{-4}	.496 x 10^{-6}
1.3	84.2	.158 x 10^{-4}	.986 x 10^{-6}
1.4	150.5	.174 x 10^{-4}	.185 x 10^{-5}
1.5	251.6	.186 x 10^{-4}	.332 x 10^{-5}
1.6	397.9	.194 x 10^{-4}	.573 x 10^{-5}
1.7	600.8	.200 x 10^{-4}	.966 x 10^{-5}
1.8	872.1	.204 x 10^{-4}	.162 x 10^{-4}
1.9	1,223.0	.205 x 10^{-4}	.277 x 10^{-4}
2.0	1,663.6	.202 x 10^{-4}	.500 x 10^{-4}
2.1	2,199.7	.192 x 10^{-4}	.109 x 10^{-3}
2.16	2,567.7	.184 x 10^{-4}	.270 x 10^{-3}

Table 3-11 Results for Ceramic Plug (.5 micron)

Material = Ceramic

Porosity = .548

Pore Size = .1792 micron

Thickness = .0065 m

Thermal Conductivity at 2°K = 11 W/m °K

Permeability = $5.3726 \times 10^{-15} \text{ m}^2$

Temperature °K	Flow Rate SCC/M	V_n m/sec	V_s m/sec
1.1	16.0	.260 $\times 10^{-5}$.366 $\times 10^{-6}$
1.2	30.7	.117 $\times 10^{-4}$.455 $\times 10^{-6}$
1.3	52.2	.336 $\times 10^{-3}$.304 $\times 10^{-6}$
1.4	83.9	.747 $\times 10^{-4}$.377 $\times 10^{-5}$
1.5	130.9	.141 $\times 10^{-3}$.146 $\times 10^{-4}$
1.6	204.5	.231 $\times 10^{-3}$.409 $\times 10^{-4}$
1.7	321.7	.338 $\times 10^{-3}$.954 $\times 10^{-4}$
1.8	502.7	.448 $\times 10^{-3}$.197 $\times 10^{-3}$
1.9	761.3	.543 $\times 10^{-3}$.374 $\times 10^{-3}$
2.0	1,096.1	.600 $\times 10^{-3}$.685 $\times 10^{-3}$
2.1	1,484.9	.606 $\times 10^{-3}$.145 $\times 10^{-2}$
2.16	1,717.4	.580 $\times 10^{-3}$.351 $\times 10^{-2}$

ORIGINAL PAGE IS
OF POOR QUALITY

Discussion of Results

While a large number of tables could be generated, the three tables of results provided here are sufficient to illustrate many of the basic characteristics of all the results obtained using the relationships provided.

a. Comparison with experiment

Table XII gives samples of the results obtained in experiments conducted at MSFC and Stanford.

Table 3-12 Experimental Results

Temperature	MSFC Nickel Plug 7 - 10 micron SCC/M	Stanford Rolled Aluminum Foil Plug SCC/M
1.6	370.	312.
1.7	540.	564.
1.8	760.	803.
1.9	1200.	624.
2.0	1900.	442.
2.1	3000.	336.
2.16	3800.	336.

The Stanford results were obtained from "Research at Stanford on the Containment of Liquid Helium in Space by a Porous Plug and a Long Hold-Time Dewar for the Gyro Relativity Experiment" by Lipa, Everitt, and Fairbank . The fact that the MSFC plug and the Stanford plug had different dimensions was not taken into consideration in constructing Table XII.

The experimental results given in Table XII show similar total flow rates in the range of 1.6 °K to 1.8 °K for both the MSFC and Stanford plugs. However, at 1.8 °K and higher, the Stanford plug shows a reduction in flow rate with increasing temperature to the lambda point. The MSFC plug on the other hand shows a monotonically increasing flow rate with increasing temperature which is in agreement with that predicted by the equations developed here as given in Tables IX, X, and XI.

The theory developed here is found to predict the behavior of the MSFC large pore Nickel plug with respect to temperature. While the shape of the flow rate versus temperature curve is accurately predicted, the values predicted are about 30% less than that measured at temperatures near the lambda point. The agreement at lower temperatures is progressively better until the best agreement is reached at 1.6 °K. (7.5% error).

The reason the theory has such large error at the higher temperatures was traced to the value of the pumping factor $\frac{F_A}{A}$ used in the program. This factor was determined for flow measurements made near 1.6 °K. If the pumping line restriction were an ideal choked orifice as modeled, this factor would be constant. However, since the restriction is more complex, the factor is not constant and is found to increase as the pressure on the gas side of the plug increases. Future work will modify the model of the pumping line restriction to yield improved comparison with experiment.

CHAPTER 4 - GYRO ROTOR AND HOUSING MANUFACTURE

I. Introduction

In this section of the report, the gyro rotor and housing manufacturing developments are reported. The effort was principally directed by Wilhelm Angele who serves as consultant to UAH. In this report we first describe the basic gyro housing design and manufacturing process. We then report in some detail on the chemical etching developments that enabled the production of dimensionally stable housings. The design and manufacture of the suspension electrodes then concludes the report of developments concerning the housing. We then report on the gyro rotor developments which have resulted in the best spheres ever produced. We start the rotor discussion by describing the requirements and the material selection procedure. We then describe the quartz rotor finishing machine which was designed and built by Mr. Angele. This machine significantly advanced the capabilities of producing consistently round quartz spheres. Of practical importance to the development reported here was the parallel development of methods for measuring the rotor diameter in order to assess the advances made in rotor production. The rotor measuring equipment and designs of new equipment prepared by Mr. Angele are reported. The roundness measuring technique is then described. As part of the gyro development program at MSFC and UAH, the problem of rotor coating was also addressed. We report on the efforts to produce a uniform rotor coating and the designs developed by Mr. Angele which were used during this effort. A report on methods of measuring the metal coating thickness then follows. We conclude the report with a brief discussion of the gyro assembly procedure and a mounting fixture used for testing the completely assembled gyro.

II. GYROHOUSING DESIGN

The gyro rotor, 3.81 cm (1.5 inch) diameter, is contained in a housing with a spherical cavity. Three pairs of electrodes arranged in orthogonal positions are used to suspend and center the rotor within the housing by electrostatic forces, controlled by an electrical suspension network, operating at 20 KHz. The rotor is spun up by helium gas entering and leaving the housing at specific points. The design of the gas spin-up system changed during the development phases of the housing as will be described later. The theory of the gas spin-up is described elsewhere in this report. The measuring of the gyro precession, spin rate and other important quantities are also treated in detail elsewhere in this report.

1. Dimensional Requirements

To keep the spin-up helium gas as much as possible within the drive gas channel, the channel banks must have a very small distance to the rotor to act as a seal. A possible dimension achievable and acceptable is assumed to be 2.5 to 4 microns (.00010 to .00015 inch). The seals, while reducing gas loss, also have the effect of increasing the friction on the rotor and thus can affect the maximum spin rate achievable.

A second seal is needed around the electrodes to keep the gas from entering into the electrode area where the possibility of high voltage breakdown exists. Also, the housing design must provide a mechanical stop to keep the rotor from touching the electrodes when at rest. The levitation voltage is about 2000 volts and the field density is quite high at the sharp electrode edges. A distance of 25 to 40 microns (.001 to .0015 inch) between the electrode and the rotor is considered adequate for operation. The rest of the cavity surface, except a few rotor support spots, should have a relatively large distance from

the rotor surface .025 cm (.01 inch). The cavity is vented by several big vent holes. Figures 4-1, 4-2 and 4-3 show various views of the gyro housing. Figure 4-1 shows the major side view features of the gas channel and electrodes. Figure 4-2 shows a detailed top view of the channel entrance and the electrode region. Figure 4-3 shows an overall top view of the housing.

2. Various Spin-up Channel Designs

The design of the gyrohousing was changed several times as better manufacturing procedures were developed.

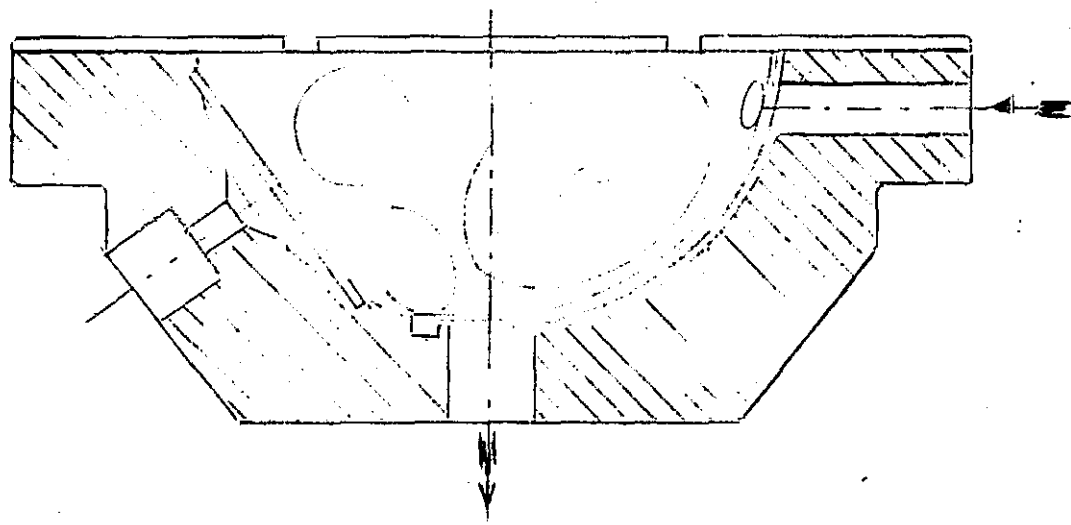
Each housing half had three problem areas:

1. A perfect and exactly half a spherical cavity with dimensional tolerance of $\pm .25$ micron (or ± 10 micro-inch) is required.
2. The gas drive channels with inlet, outlet and seals is difficult to machine on the spherical surface of the housing.
3. The three electrodes in each half to be located with an angular accuracy of 2.75 arc sec. ($\pm .25$ micron) and concentric to the cavity also within 2.75 arc sec. are also difficult to machine on the spherical housing surface.

2a. The First Housing Design with Separate Gas Channels (Split-Ring Design)

The split-ring housing was less than a half a sphere by half the thickness of the gas channel washers. Figures 4-4 and 4-5 show the details of the design. The length of one channel was $150^\circ = 4.95$ cm or 1.95 inch, permitting 30° for inlet and outlet ports. The channel washer between the two housing halves had to be split because of the .2mm (.008 inch) interference of seal and rotor diameter. A single channel washer having this requirement would not fit over the sphere. Therefore, the washer was split from .375 inch to .1875 inch thickness. The strength of the washer was further weakened by the 12 radial vent slots of .03 inch depth shown in Figure 4-5. Because of the various factors

FIGURE 4-1. SIDE VIEW
OF GYRO HOUSING



Gyro housing Rev. 2:1

FIGURE 4-1. SIDE VIEW OF GYROHOUSING

ORIGINAL PAGE
OF POOR QUALITY

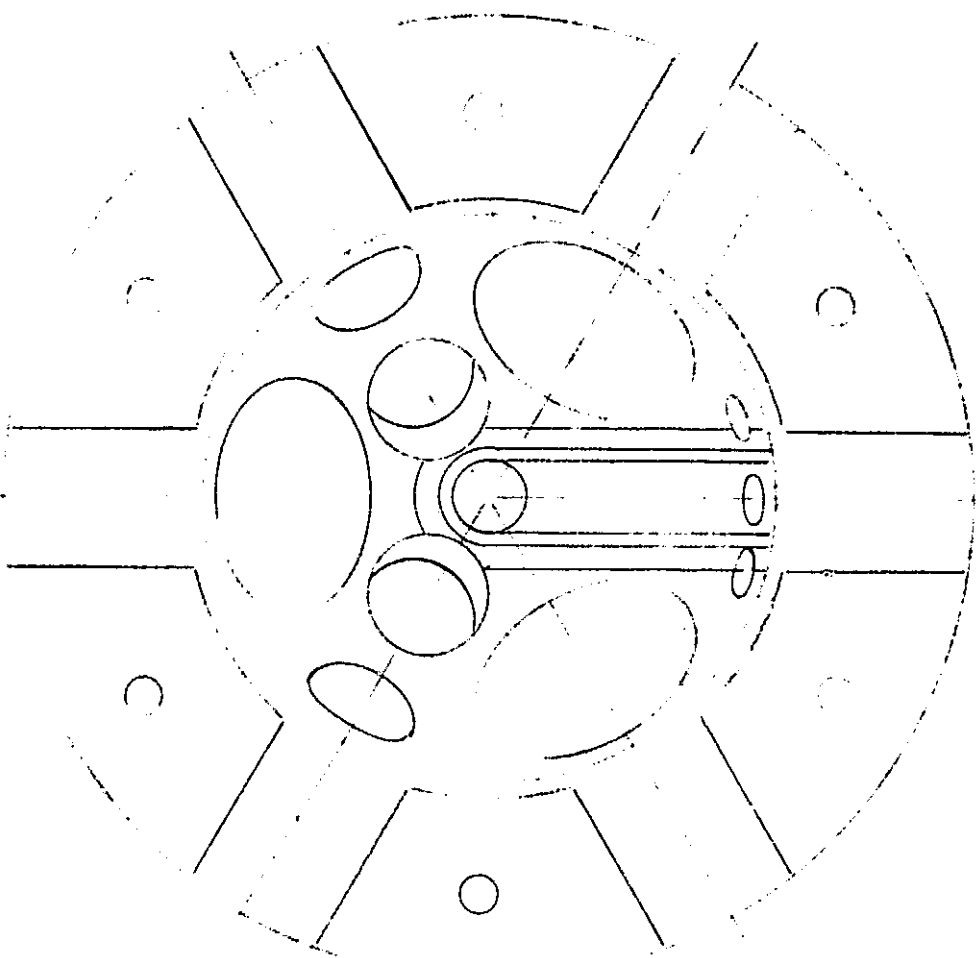
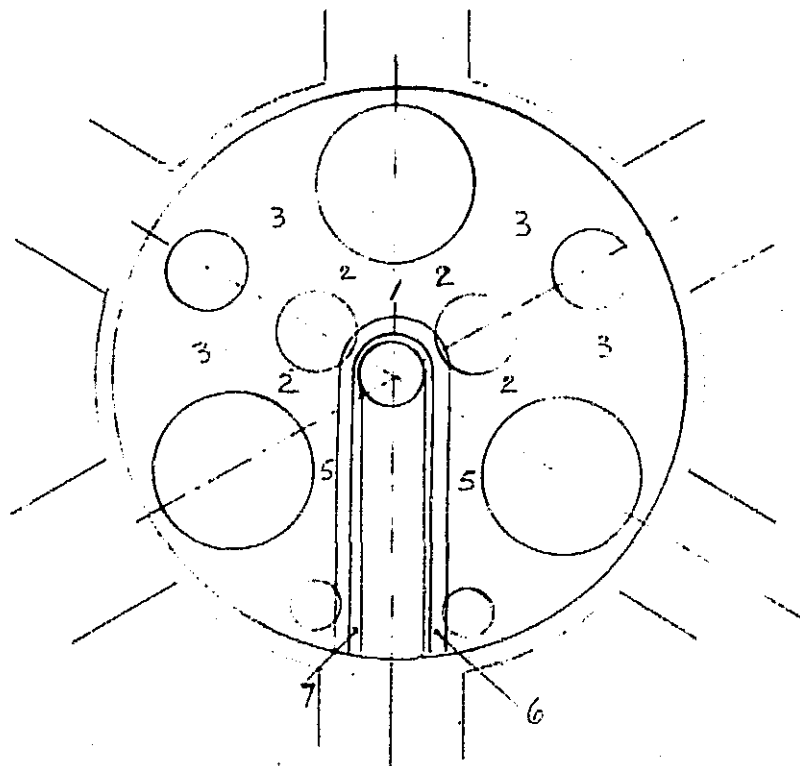


FIGURE 4-2. TOP VIEW OF GYROHOUSING

Hole distances
Average values of measurements



Location	shortest distance between	inch
1 Electrode - Drive channel mouth		.135
2 " - inner vent hole		.058
3 " - outer vent hole		.104
4 " - recess at equator		.033
5 " - Drive channel mouth		.012
6 Drive channel seal width		.034
7 Drive channel mouth width		.060

FIGURE 4-3. TOP VIEW SHOWING MAJOR FEATURES.

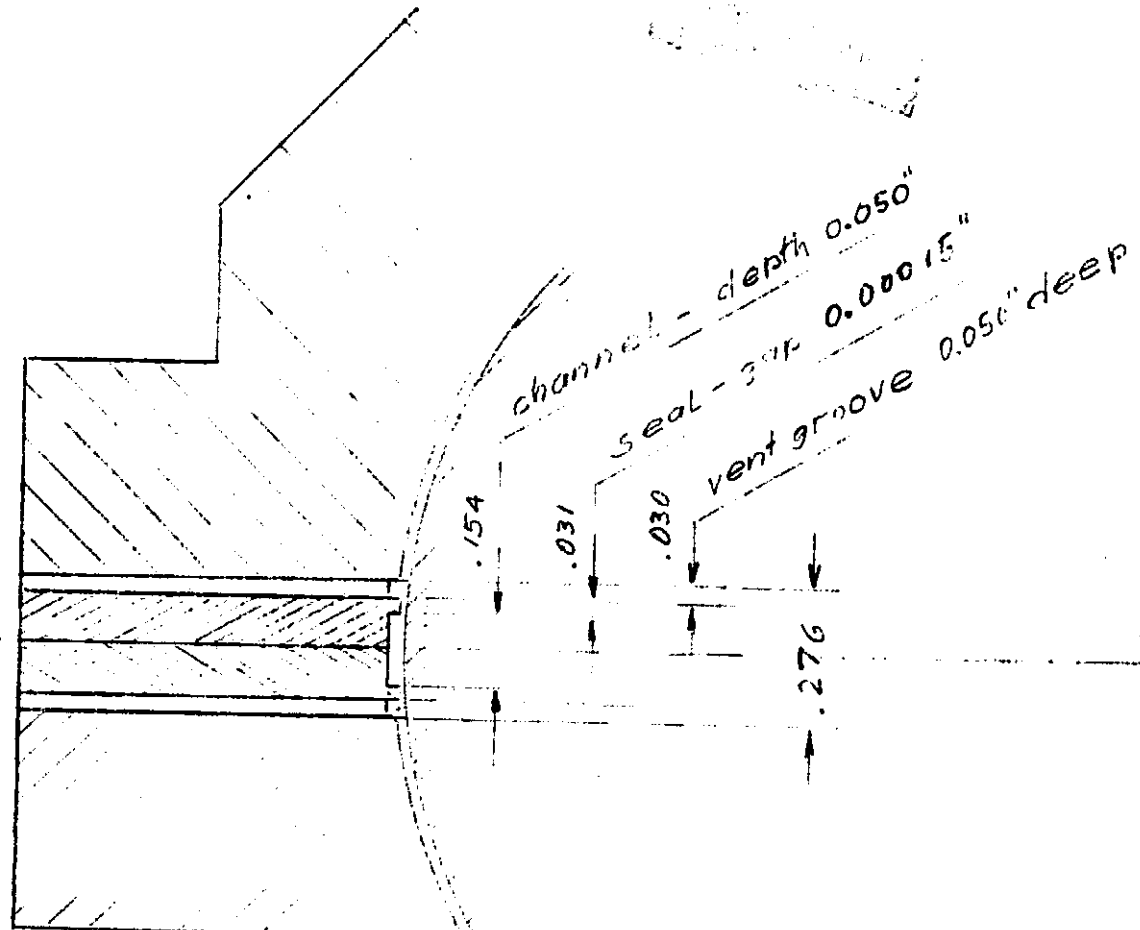


FIGURE 4-4. DETAIL SPLIT SPIN-UP CHANNEL WASHERS

C-2

ORIGINAL FIGURE
OF POOR QUALITY

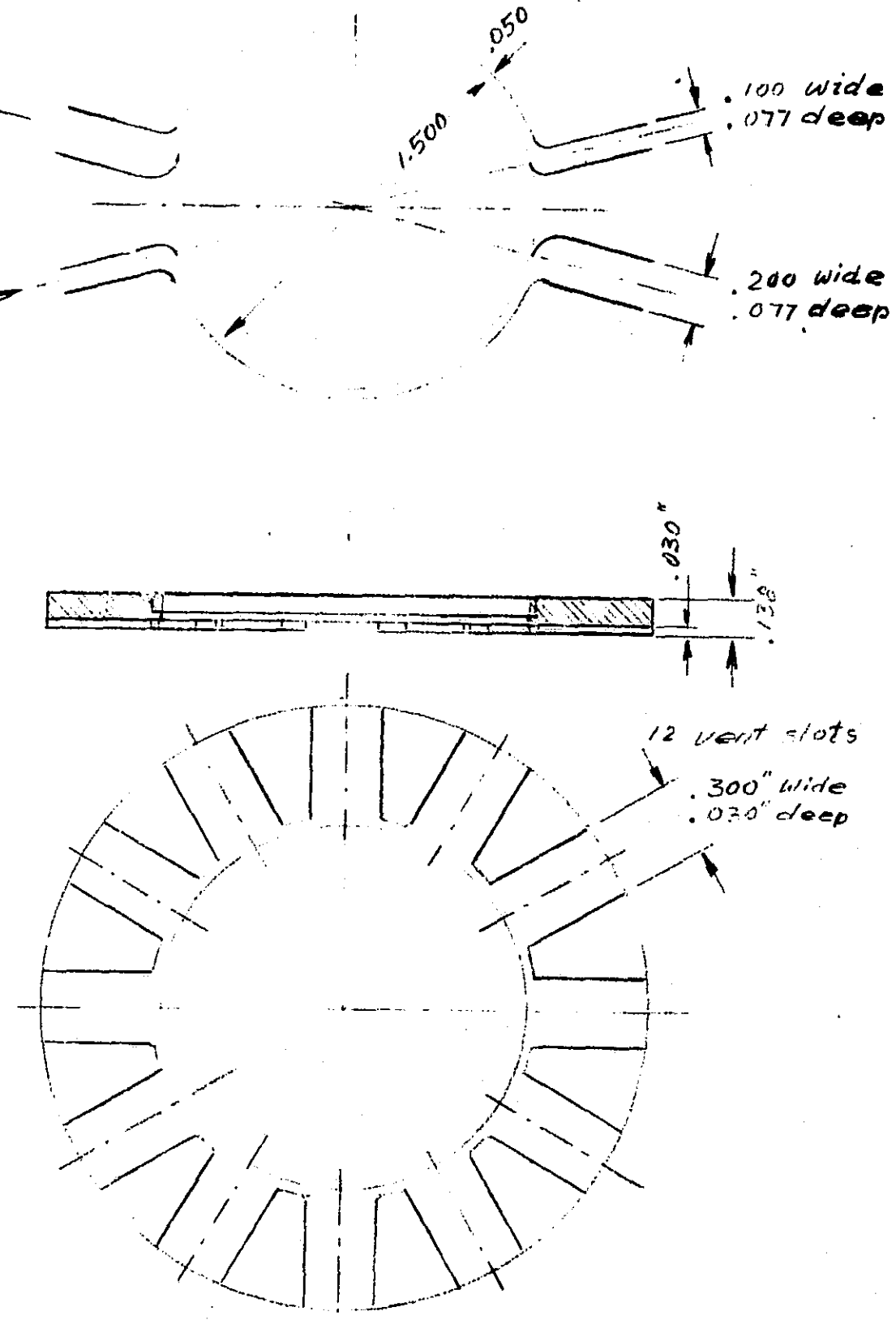


FIGURE 4-5. SPIN-UP WASHER AT EQUATOR PLANE

cited, the production of the washers proved too difficult. Also, the washer added one more tolerance to the cavity depth dimension and the centering problem. These spin-up channel designs were considered. A single spin-up channel is shown in Figure 4-6 and a dual spin-up channel design is shown in Figure 4-7. A three spin-up channel arrangement was also considered and is similar to the arrangement shown in Figure 4-10.

There were two major electrode arrangements considered during the housing development. The round electrodes are shown in Figure 4-1. We also considered a "triangular" electrode arrangement shown in Figure 4-8 which would give more electrode area than the round ones but at greater complexity in manufacture.

2b. Dividing Plane Channel Designs

A design concept was developed in which the gas channel was formed by beveled cavity edges machined into the housing half at the edge of the dividing plane, Figure 4-9. Three variations were offered:

1. A single spin-up channel with a triangular or rectangular profile passing 325° around the rotor, Figure 4-9.
2. Two channels each going 145° around the rotors.
3. Three short channels each about 95° around the rotor, Figure 4-10.

The width of the channel depends upon the suspension electrode requirement and the need of gas-seal width between channel and electrode. The number and length of the channels is influenced by the fluid dynamics of helium gas at 4.5°K and the time permissible for spin-up.

The spin-up channels in the last three configurations are formed simply by cutting a 45° chamber at the edge of the half sphere cavity except in the region between inlet and outlet ports. This design brought only a partial relief to the problem of maintaining a sharp edge (90°) between cavity and dividing (assembly) plane during the finishing operation. The use of a lapping tool of less than half a sphere (calotte) and by keeping the edge of the tool nearly in

FIGURE 4-6
OF FOCAL REGION

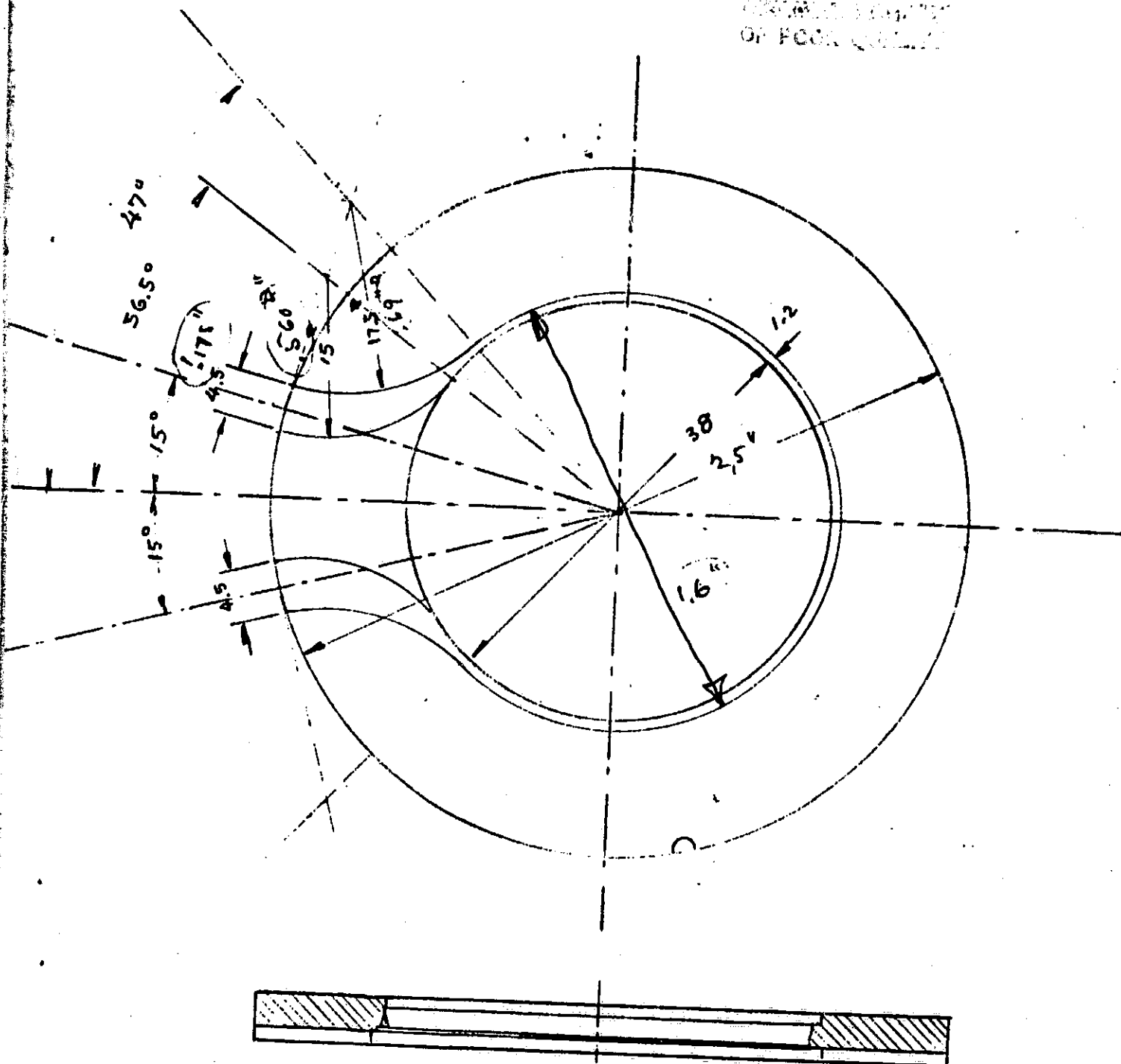


FIGURE 4-6. SPIN UP RING, SINGLE CHANNEL

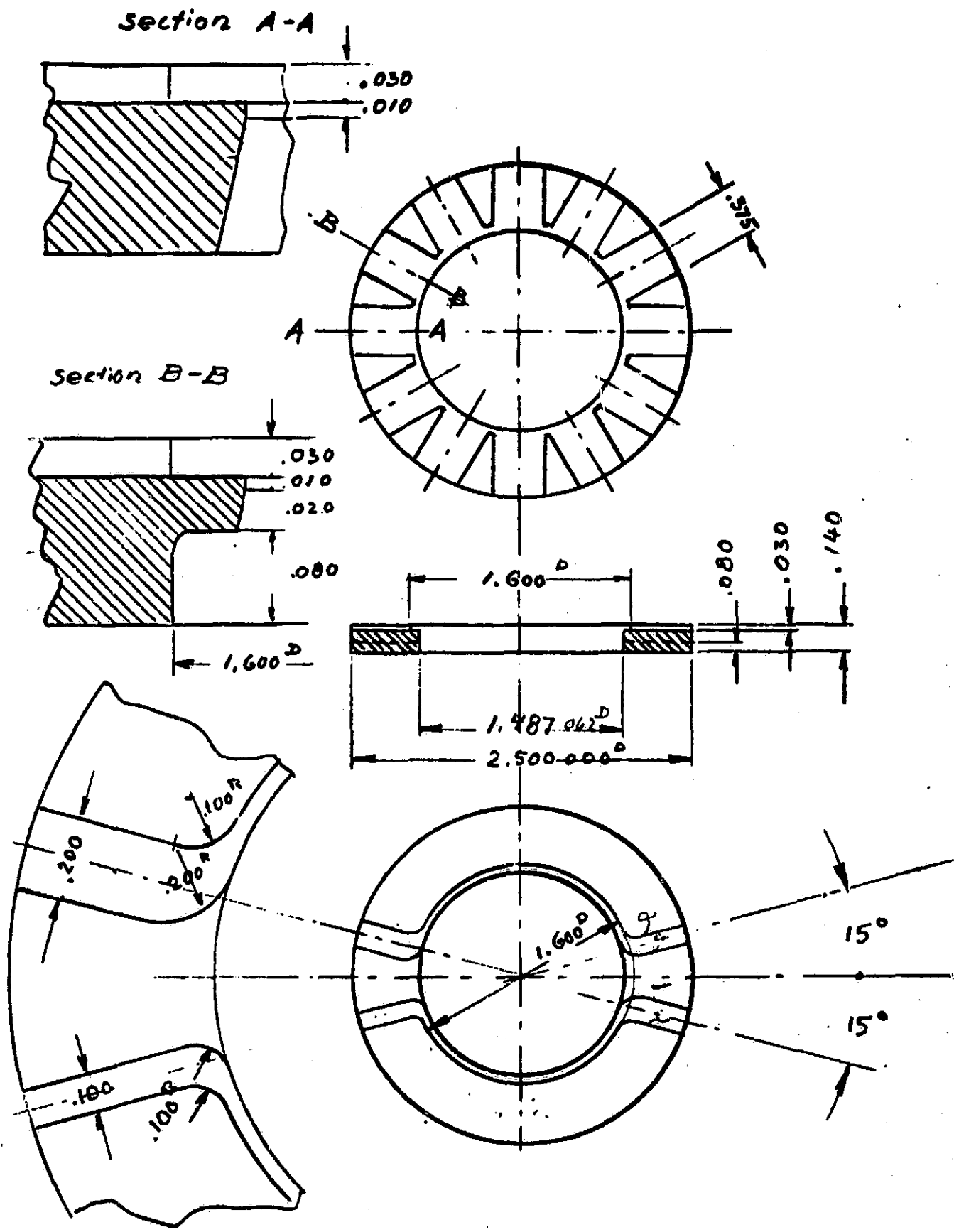
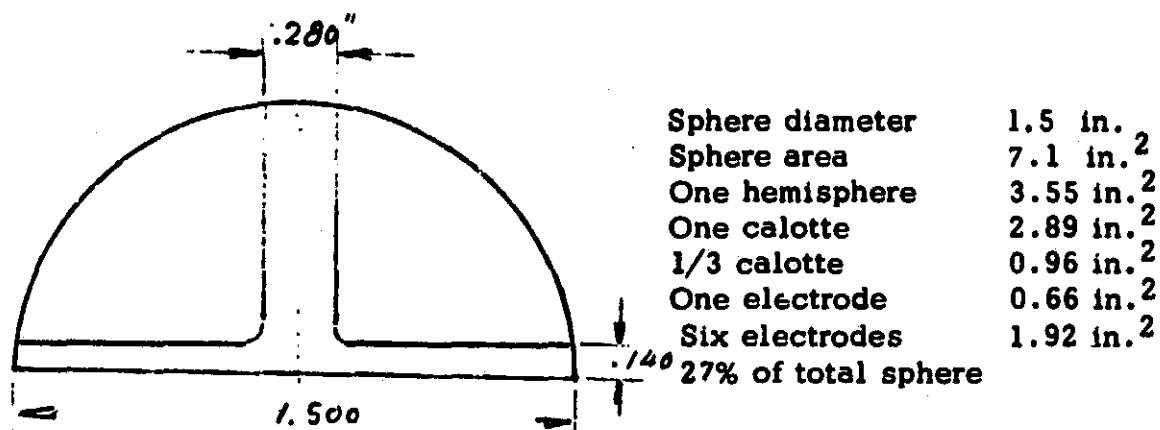


FIGURE 4-7. SPIN-UP DISC, DUAL CHANNEL

The area of the electrodes for the electrostatic rotor suspension is calculated in round figures as follows. The gyro cavity (shell) has 6 electrodes (3 pairs) of triangular shape. Each hemisphere of the cavity has 3 electrodes. The axis of the 3 pair of electrodes are mutually perpendicular.



The electrode size of the Honeywell design is 0.720" diameter or .32 inch².

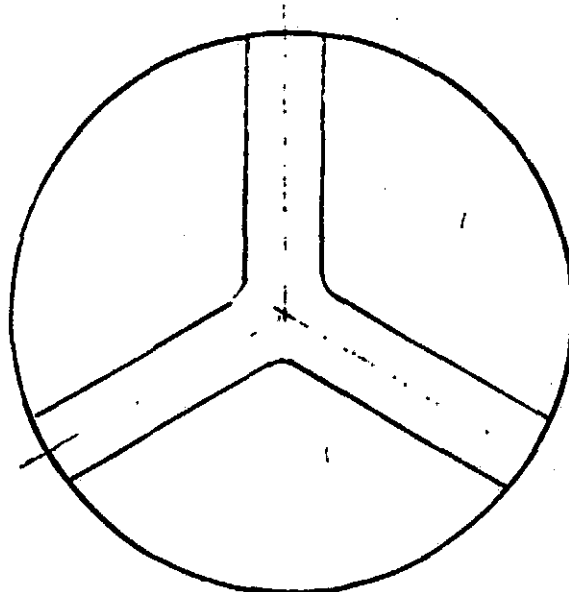


FIGURE 4-8. THE "TRIANGULAR" ELECTRODE DESIGN

ORIGINAL VALUE
OF POOR QUALITY

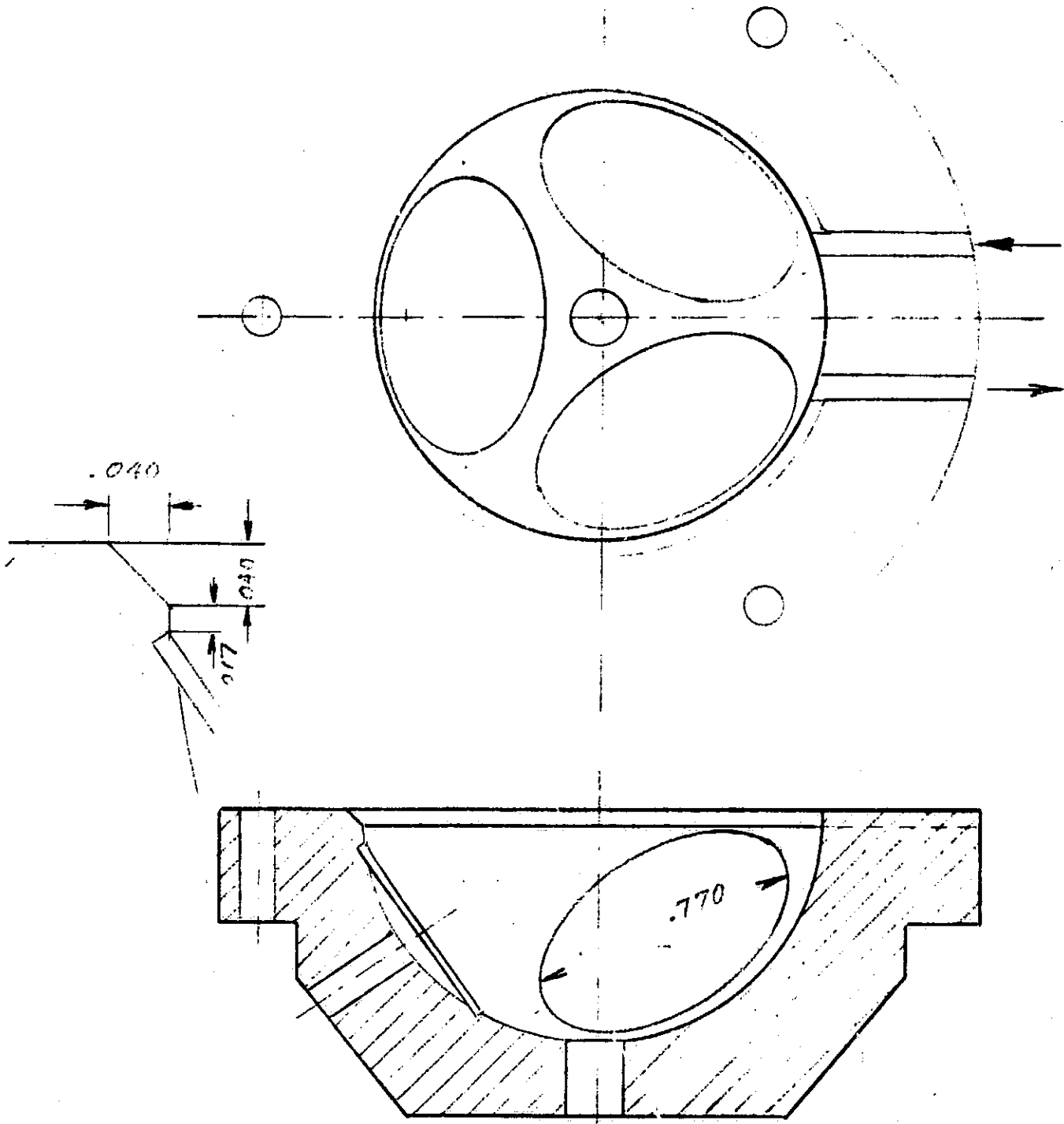


FIGURE 4-9. ONE SPIN-UP CHANNEL IN THE EQUATORIAL PLANE

ORIGINAL PAGE IS
OF POOR QUALITY

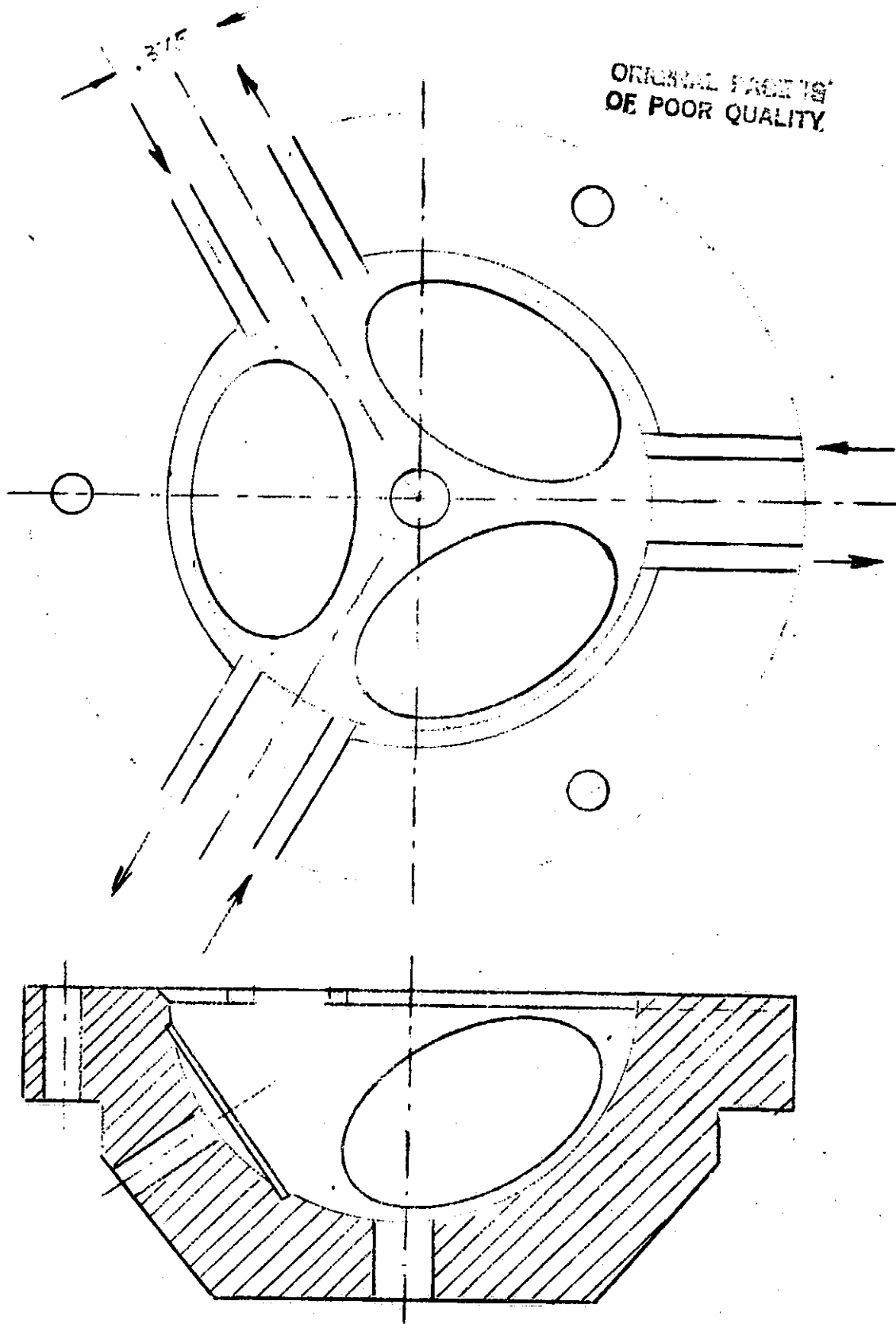


FIGURE 4-10. THREE SPIN-UP CHANNELS IN THE EQUATORIAL PLANE

tangential motion to the edge of the cavity helped to keep the edge from breaking. This very problem was the reason for separating the spin-up channel from the cavity body by making two separate spin-up washers in our first housing design.

Both types of designs, separate spin-up washers as well as dividing plane channels, present manufacturing problems and required considerable efforts. Therefore, the search for a better design continued. Also, it was desirable to develop a design which would support the Stanford housing design program.

2c. Spin-up Channel Turned 90°

A design was developed which incorporated the spin-up channel at 90° to the dividing plane as was the Stanford housing design. Also, the flange and mounting hole dimensions and locations were made identical to the Stanford design. We then concentrated on developments of the outer form, the electrodes, and the spin-up channels. A top and side view of the current housing is shown in Figures 4-11, 4-12.

Each housing half has a spin-up channel beginning below the dividing plane and ending at the bottom of the cavity, extending over 71° or a length of 2.36 cm (0.93 inch). Its cross-section is 0.46 cm (0.180 inch) wide and 0.064 cm (0.025 inch) deep. Around the channel is a seal 0.076 cm (0.03 inch) wide and a well vented moat 0.016 cm (0.062 inch) wide and 0.16 cm deep. The joining plane of the two housing halves has six vent slots 0.95 cm (.375 inch) wide and 0.15 cm (0.06 inch) deep.

The three electrodes 1.91 cm (0.75 inch) diameter are 0.013 cm (0.005 inch) recessed by precision chemical etching. The rest of the cavity area has several vent holes:

4 ea 0.787 cm (0.31") diameter

1 ea 0.457 cm (0.180") diameter

2 ea 0.318 cm (0.125") diameter

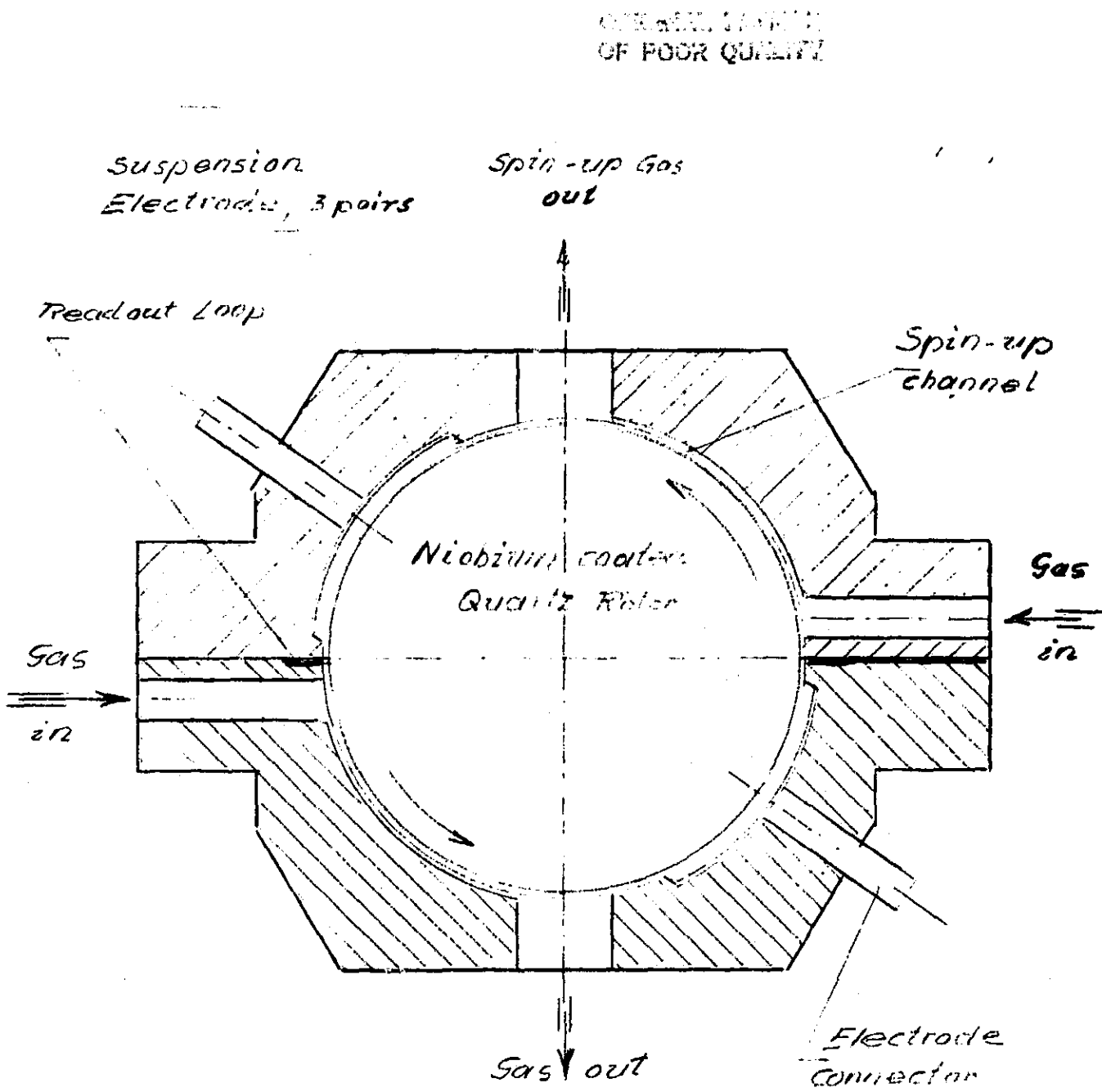


FIGURE 4-11. SUPER CONDUCTIVE QUARTZ GYRO SCHEMATIC

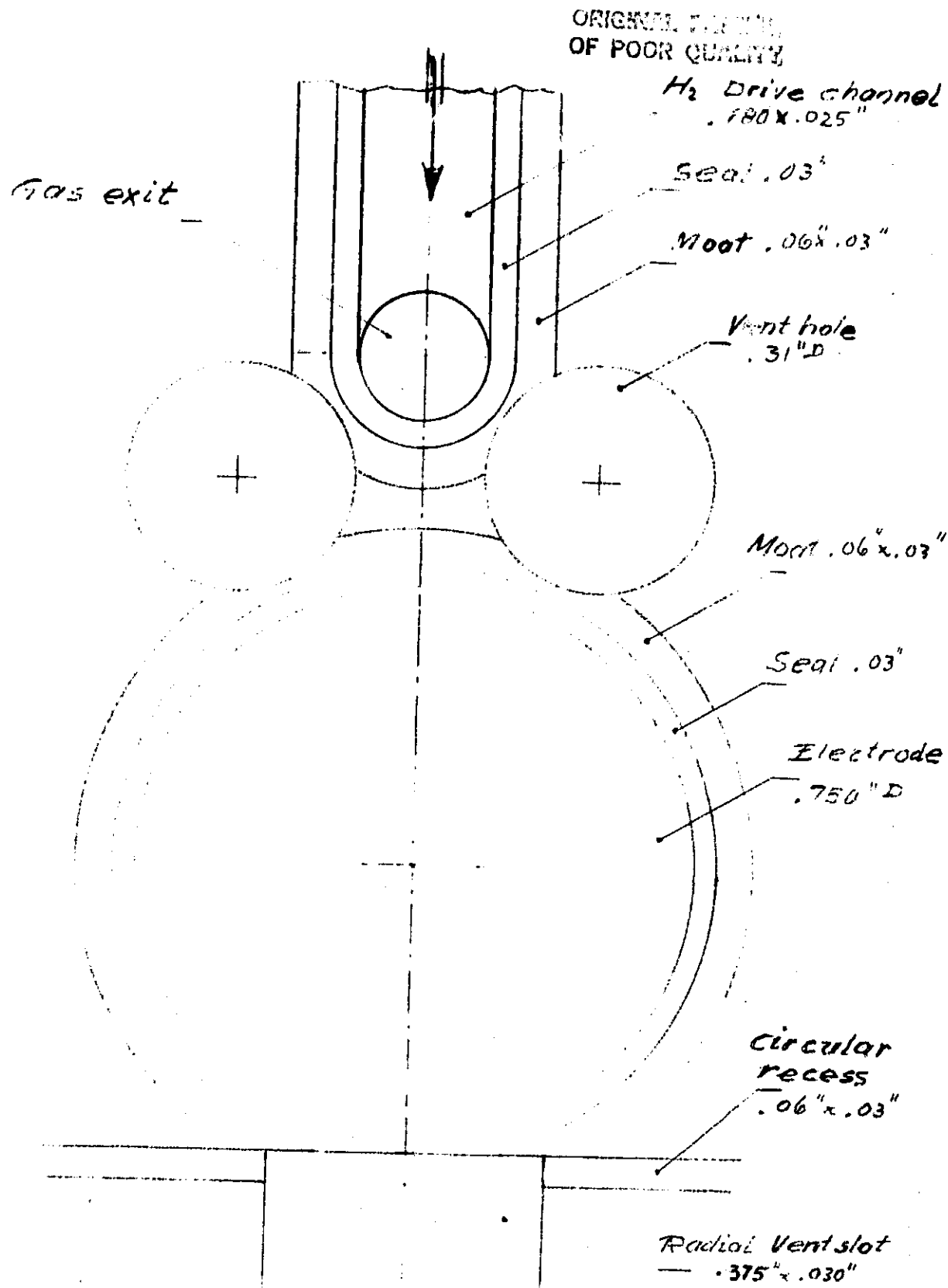


FIGURE 4-12. HOUSING CAVITY DETAIL FLATTENED - NOT TO SCALE

The 14 vent holes and the 6 slots in the housing amount to an area of 5.41 cm² (0.84 inch²) which is 12% of the cavity area.

The surface of the cavity, which is not used for spin-up channels, seals, electrodes and vent holes is recessed by chemical etching for more clearance between rotor and housing, enhancing venting and reducing gas drag.

Table 4-1 gives a comparison of the main data on spin-up channels of the three different housing designs.

Table 4-1. Spin-Up Channel Dimensions

Type	1	2	3	4	5
All Dimensions cm or cm ²	Channel In The Dividing Plane				Channel 90° Turned
	Washer	Long	Medium	Short	
Number of Channels	2	1	2	3	2
Figure	3 & 4	5	—	6	7
Channel Length	4.99	11.0	5.03	3.04	2.52
Channel Width	0.254	0.2	0.2	0.2	0.457
Channel Depth	0.076	0.034	0.034	0.034	0.0635
Channel Cross- Section cm ²	0.0096	0.0068	0.0068	0.0068	0.029
Total Gas Con- tact Area cm ²	2.535	2.2	2.012	1.82	2.303

III. HOUSING MANUFACTURING PROCESSES

1. Grinding and Ultrasonic Machining

The material selection for the gyro rotor is more demanding than for the housing and is discussed in more detail later. Material homogeneity is also of considerable importance for the housing and, in spite of the higher material price, it is recommended to use Homosil, a trade name from Amersil, Hillside, N.J., for very uniform fused silica. The process for housing manufacture begins by cutting a disc of 1.12 inches from a 3-inch diameter Homosil cylinder using a sharp cutoff wheel with plenty of coolant and very low cutting rate to keep the temperature from rising. Next the rough contour of the housing half is cut by grinding on standard cylindrical grinding machine. The grinding cutting rate should be kept very low to keep the temperature at near room level and to insure that no machining stresses develop in the quartz body. The cut rate is lowered and a finer grain size grinding wheel is used as the final dimensions are approached.

All details of the cavity and flange surface are formed by ultrasonic machining, a process widely used by industry to form extremely hard or brittle materials. The process removes material by fatiguing and erosion of the surface through bombarding it with tungsten carbide particles in a cooling and circulating liquid. The tool of relatively soft metal and negative shape vibrates vertically at ultrasonic frequency a very short distance from the work piece. The tool is advanced as stock is removed. The development of the shape of the cavity requires several ultrasonic tools and operations. One tool is used to recess the rim of the suspension electrodes as the cavity turns on a precision turn-tilt table. The tilt angle is 54.742° against the cavity centerline. The rotation from electrode to electrode is $120^\circ \pm 10$ sec. which is within the accuracy of a high quality toolroom tilt-turn index table. The stock removal

from the work piece and the wear of the tool depend upon their hardness, resiliency and fatiguing. (The soft tool steel wears much less than the quartz.)

Directly connected to the manufacturing are the measuring problems, especially when we work for extremely high accuracies.

2. Cleaning and Measuring Procedures

The cleaning process is as follows:

- a. Clean housing with soft toothbrush and clean holes with soft bottle brush in xylene, then rub with lint-free soft rag in xylene.
- b. Cook parts at 80 - 90° C for ten minutes in "Chromerge," a cleaning liquid from Emil Steiner Co., New York 13, N.Y. or use a saturated solution of chromic acid CrO₃ in concentrated sulfuric acid H₂SO₄ (1.84 g cm⁻³). Rotate the housing half in all directions while immersed in the cleaning solution (use a loosely woven glass cloth strip 6" x 18" for rotating and handling).
- c. Rinse part in hot running and filtered water for five minutes while tumbling with glass cloth.
- d. Rinse part in running deionized water while tumbling with glass cloth for five minutes.
- e. Hang part with glass cloth in 500 ccm beaker and place beaker in ultrasonic cleaner. Use distilled water in beaker and ultrasonic tank. Vibrate for ten minutes while tumbling the part slowly by see-sawing the glass cloth ends alternately.
- f. Roll part from glass cloth to a cleaned three-point teflon support base and cover with well-vented beaker for drying.
- g. Check cleanliness of part under a microscope (60x) before placing in a storage container or before beginning the next phase of manufacturing (coating). Store glass cloth in separate clean container.

Clean rotor by washing and rubbing the rotor with a soft lint-free rag in xylene. After cleaning, measurements of cavity dimensions and concentricity to the rim can be made. Since the clearance between rotor and cavity seals is only 0.000381 cm (or 0.000150 in) it is very important to stay within the tolerances of the cavity diameter and depth. Equally important is to orient the two housing halves to each other with regard to rotation and lateral shift. To facilitate the control of the lateral positions of the cavities, the concentricity error of cavity and rim must be near zero. This can best be measured by the differential method. After the cavity is centered on the turntable of a measuring machine, two stationary sensors are used--one at the edge of the cavity and the other at the rim, both in line with a cavity radius. Both sensors should be adjusted to the center of their scales. The combined output of the two sensors indicates the amount and location of the eccentricity.

The eccentricity can also be measured by two separate recordings of rim and cavity on one polar chart.

The cavity depth requirement and tolerance are:

Depth: 1.905318 cm (0.750125 inch)

Tolerance: $\pm 0.000\ 064$ cm ($\pm 0.000\ 025$ inch)

Figure 4-13 shows the setup for making this measurement using a sphere, a ring gauge (both of known dimensions) and an optical flat on top. The sphere can be lifted by a lever arm within the clearance given by the sphere diameter, the cavity depth and the gauge ring thickness. An electric sensor measures the amount of lifting.

The lifting can also be measured by counting the concentric fringes moving out of the contact point at the top of the sphere as the sphere is lowered or lifted. The fringe counting is greatly facilitated by using a low power microscope with a crosshair. One fringe represents 29.5×10^{-6} cm (11.6×10^{-6} inch) if a monochromatic light of 5876 Å is used.

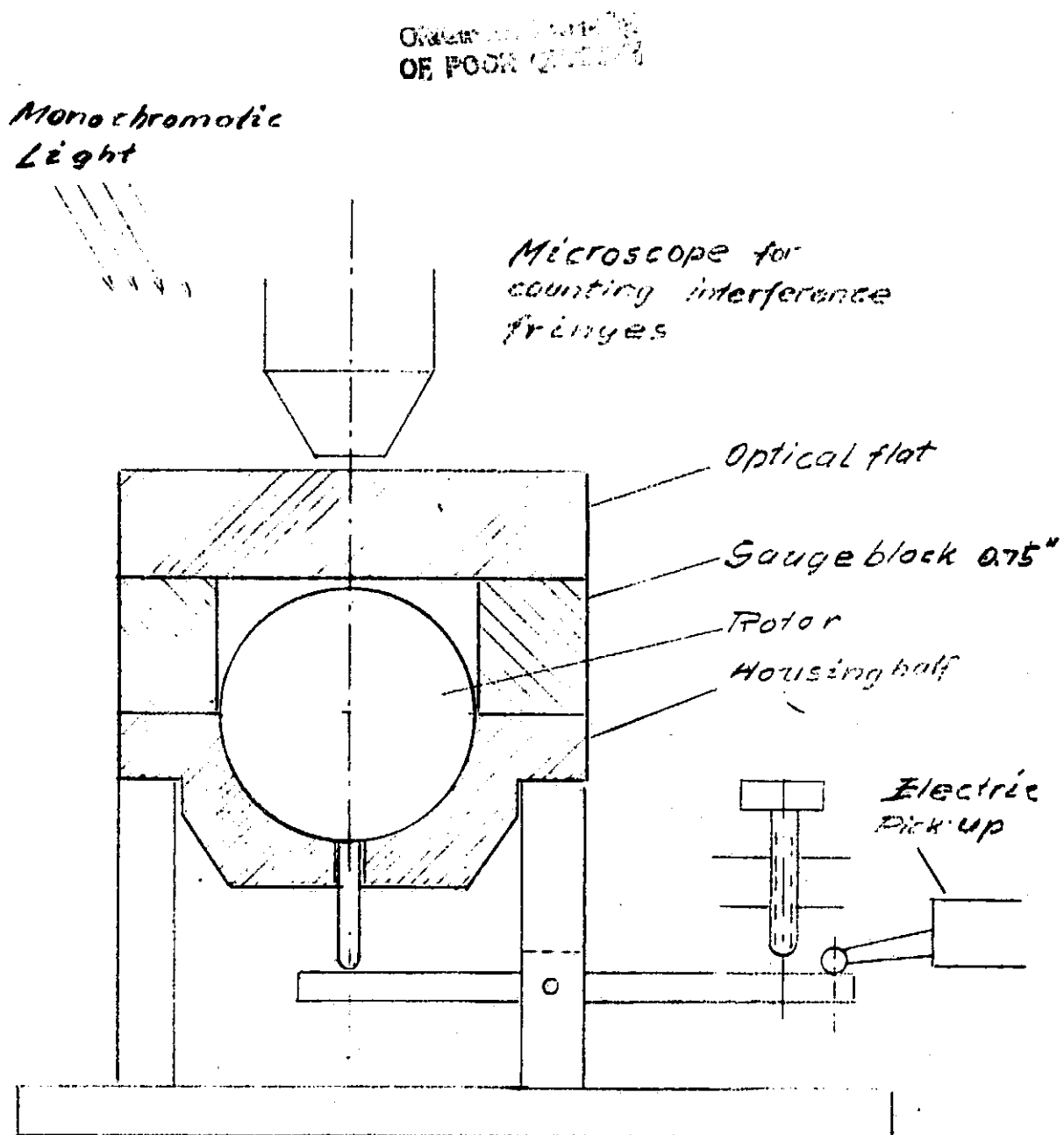


FIGURE 4-13. SET UP TO MEASURE DEPTH OF CAVITY BY ELECTRIC PICK UP OR FRINGE COUNT

The rotor clearance can be measured in the assembled housing in several directions, by lifting the rotor through the large vent holes of the cavity and using an electromechanical sensor as before.

IV. CHEMICAL ETCHING OF THE SUSPENSION ELECTRODE AREAS IN A QUARTZ GYRO HOUSING

1. Summary

A brief discussion is presented on how to depress the areas for the levitation electrodes by chemical etching rather than by mechanical lapping. The etching process, equipment, and measuring techniques were developed for this specific application. Since the quality of the etched samples were much better than accomplished by lapping, the first gyro housing of the Type 77 made of quartz was prepared and successfully etched. See Figure 4-14.

2. Housing Design

The gyroscope consists of a quartz housing made of two identical halves into which is closely fitted a spherical rotor of 3.81 cm (1.5 inch) in diameter also of quartz. The housing cavity has 3 pairs of electrodes, orthogonally located for electrostatic suspension of the rotor. There are also 2 gas channels to set the ball in rotation and evacuation openings to remove the gas. A place is provided for a precise precession loop using a Josephson junction. To prevent mechanical contact between rotor and electrodes, the electrodes are recessed by about .025 mm (.001 inch).

3. Electrode - Positions and Tolerances

We summarize here the major requirements and tolerances concerning the electrodes.

- a) The angular positions of the three electrode pairs must form an x, y, z orthogonal coordinate system with an angular accuracy of ± 1 arc sec.
- b) The radial distance of the electrodes from the center of the cavity should be held to $19.075 \text{ mm} \pm 0.0012 \text{ mm}$ ($0.751 \text{ inch} \pm 5 \times 10^{-5} \text{ inch}$). This tolerance controls the position of the rotor within the cavity if not adjusted

;

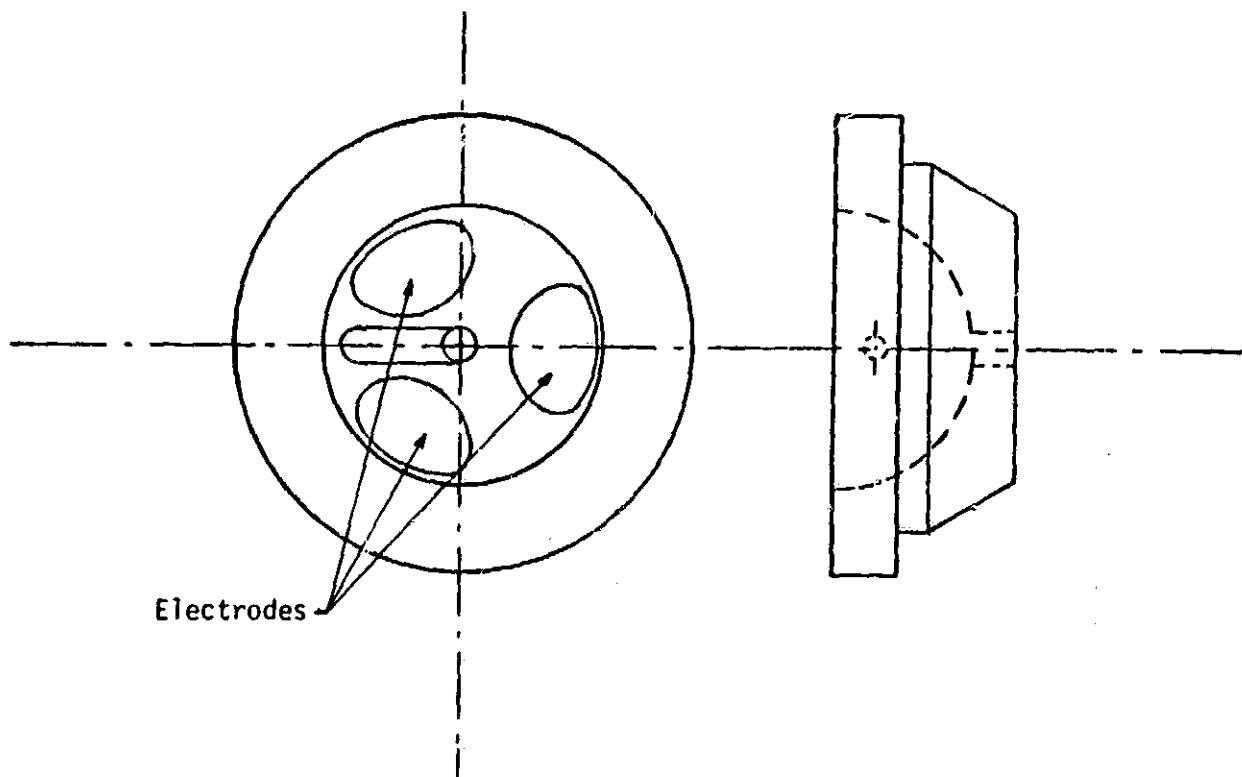


FIGURE 4-14. HOUSING HALF OF GYRO TYPE 77 WITH THREE SUSPENSION ELECTRODES. SCALE 1:1, 750" DIA., .001" DEEP.

by the individual electrode voltages. Eccentric rotor position causes eccentric and excessive gas leakage over the edges of the spin up channels and/or changes the clearance between rotor and seals dangerously.

c) The electrode diameters can vary from 18.92 mm to 19.18 mm (.745" to .755") but should be uniform in one pair of housing halves within .050 mm (.002 inch).

d) The curvature of the electrodes must be concentric to the rotor within reasonable limits to form a relatively constant gap.

e) The electrodes cannot be tilted more than 2 arc sec in any direction.

f) The surface finish should be better than .0013 mm (50 μ inch) and must not have sharp edges or points for reasons of electrical sparking. The levitation voltage is about 2000 volt at 1 g.

g) The outer rim of the electrodes is gradually turning from spherical to flat ending at the bottom of a moat which is .25 mm (.010 inch) depressed into the housing. The larger distance .25 mm (.010") of the electrode edge gives added safety against sparking at the edges.

4. Recessing the Electrodes by Lapping

At first a machine was designed and built to lap the electrodes one at a time. More recently however the lapping is done with a Jigboring machine. The housing half is held and precisely rotated 120° with a Pratt and Whitney rotating tilt table. Both the Jigboring machine and the turn table are the highest quality tool room pieces available. The lapping result was of poor quality and the amount of time spent was excessive, even though the effort was made by experienced tool and die makers.

5. Recessing the Electrodes by Chemical Etching

The requirement of close tolerances and the marginal results from mechanical lapping efforts discussed above called for a new approach to fulfill the requirements. It was felt that chemical etching with careful control of tem-

perature and time would produce better quality electrodes with much less effort on time and tooling. The development of the etching process is discussed in the following.

A large number of etching tests were made with small samples of about 25 mm square (1 inch square) to find the best suitable resist and etchant. For close control of the etch rate, it was proposed to use buffered Hydrofluoric acid. The first tests required hours of etch time to remove a layer of about .025 mm of quartz. The photo etch resist did not withstand the long exposure to the acid and no area control was possible. Then we switched to HF 49% which removed about .025 mm in about 20 min. The resist was changed to bees wax which can be applied hot in liquid form by dipping. Beeswax adheres well to the quartz surface and can stand the etch time easily. The area which is to be etched is protected during the wax coating by a template placed to the surface by a silicone or other adhesive for ease of removal for etching.

A number of etch tests were made to develop the process and to find the surface requirements of the quartz to be etched. It was found that the preparation of the quartz surface is of great importance because it influences greatly the etch rate and the resulting surface finish.

Rough machined surfaces with only superficial improvements by lapping produced very rough surfaces and a high and irregular etch rate. Etching reveals previously invisible machining stress marks. This is why metal specimens are polished and etched for metallographic and stress studies. To accomplish a uniform etch rate and a fine surface finish, the material must be machined with increasingly finer cuts until the final dimension is reached. This applies also for lapping.

A number of 2.5 x 2.5 cm (1 inch square) etch test specimens of quartz were prepared in the same manner as the gyro cavity will be prepared. This means the squares were machined and lapped until all the disturbed material from the first

machining was removed. Then the specimens were wax coated except one square centimeter area for etching. To study the effect of the etchant flow, some of the samples were placed in vertical positions and others in horizontal positions in the etch tank. The etchant used was Hydrogen fluoride 49% from Baker Chemical, Philadelphia. No agitation of the liquid or motion of the part was done.

A large number of samples with similar preparations were etched. Only 9 samples are listed in the Table 4-2 below. Figure 4-15 shows how the etched samples appear. The surface finish was measured with a Talysurf machine. Its feeler moves with .1 gr force over the surface following the contour up and down and producing a calibrated recording. The machine also outputs a plot of the centerline average, CLA, by integrating the topographic cross-section. The feeler, or sensor, (a four-sided 90° pyramid with a point of 2.6 micron radius) moves a distance of 1.25 mm at a speed of 2.5 mm per sec. The sensor cannot detect concave surface features or fine cracks smaller than its top radius.

6. Evaluation of Etched Samples

The etch samples were 25 x 25 x 6 mm.

Table 4-2

No.	Etch Time (Min.)	Stock Removed (Microns)	Etch Rate Mic/Min	Test Data on 9 Etched Samples			Diff. Bef.-Aft.
				Before Etching CLA Micron	After Etching CLA Micron		
1	15	20	1.33	.18	.55		.37
2	17	21	1.24	.18	.55		.37
3	19	25	1.32	.20	.85		.65
4	19	25	1.32	.13	.50		.33
5	19	25	1.32	.15	.60		.45
6	19	25	1.32	.15	.60		.45
7	19	26	1.37	0	.55		.55
8	19	25	1.32	0	.67		.67
9	19	27	1.42	.20	.67		.47

The etch samples were 25 x 25 x 6 mm.

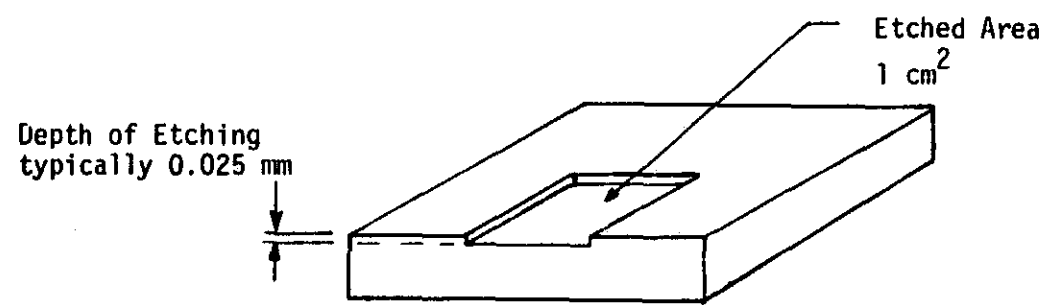


FIGURE 4-15. ETCHED SAMPLES

Table 4-2 shows the etch results of nine samples. The table shows differences in surface finishes. It is assumed that the variations in the results are, to a large degree, caused by varying treatments of finishing before etching and the fact that quartz of different boules was used. The sample preparation and etching was done over a period of about 4 weeks with slightly different temperatures. No attempt was made to repeat etch tests under exactly equal conditions. Typical surfaces before and after etching are shown in figures 4-16 and 4-17.

The average etch rate is 1.35 microns per minute and it takes 19 minutes to remove 25 μ . The surface finish changed from various fine finishes before etching to about .6 micron CLA after etching. Notice sample 7 and 8 had an extreme high finish and were roughed also to .55 and .65 μ by etching. A finish of .6 μ is still very fine and good enough for the electrical requirements of the electrodes.

The microscope reveals that the etched surface consists of neat shallow spherical depressions of 2 to 24 μ in diameter and about 10% of that in depth. The boundary lines of these dimples are rather well defined and where 3 ridge lines meet is a seemingly sharp peak. The peak angles calculated from given dimensions are 130° to 135°, which is rather blunt and will hardly be a danger for sparking even though the levitation voltage at 1 g gravitation is about 2000 volts. The surface finish of the etched samples is better than 1 μ which compares to a fine lapped or polished condition favorably.

The table 4-3 gives an evaluation of a microphotograph of Sample #6 in Table 4-2. Etch time 19 min., HF 49%, Mag. 1000 times.

ORIGINAL PAGE IS
OF POOR QUALITY

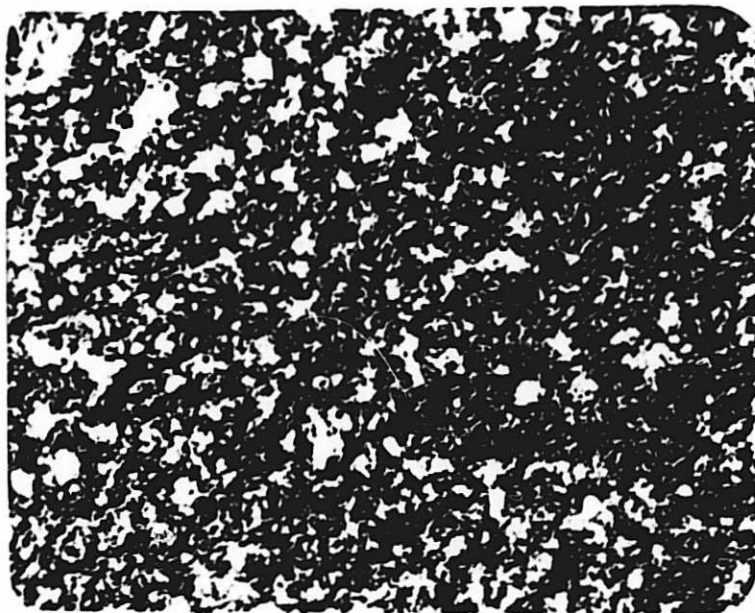


FIGURE 4-16. BEFORE ETCHING (1000 X MAGNIFICATION)

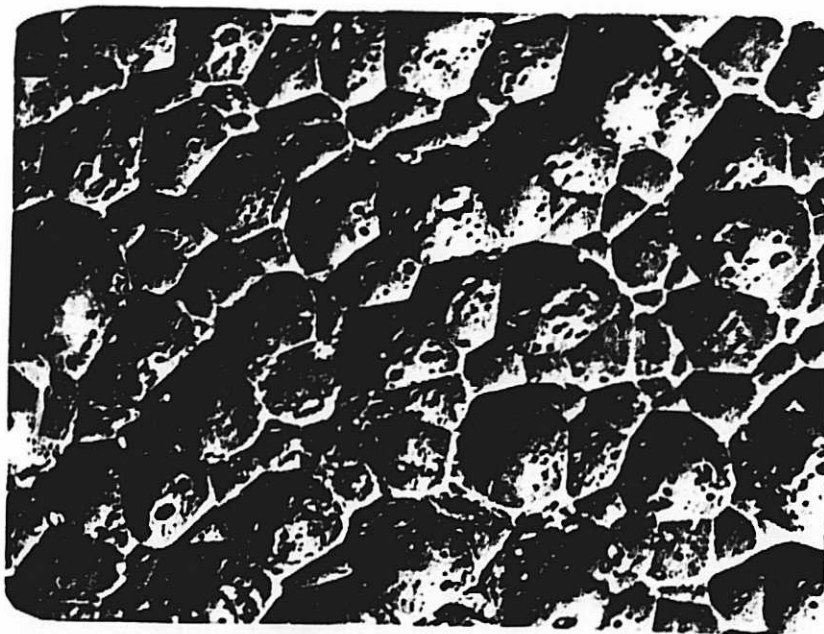


FIGURE 4-17. AFTER ETCHING (1000 X MAGNIFICATION)

Table 4-3
Surface Data from Micro Photo - Sample 6

Pit Size mm	2	4	6	8	10	12	14	16	24
Number of Pits	1	6	6	7	7	6	6	4	2
Pit Diameter μ	2	4	6	8	10	12	14	16	24
Pit Depth μ	0.2	0.4	0.6	0.8	1.0	1.2	1.4	1.6	2.4

The depth of etching is 25μ and the depth of the individual dimples range from $.2$ to 2.4μ . The average depth is 1μ which is 4% of the electrode depth and 3.4% of the distance Rotor - Electrode.

7. Etching of the Electrodes in the Gyro Housing

After sufficient data and experience were collected by etching the 25 mm square blocks, preparations were started to etch a gyro housing. An etch tank made of Teflon was prepared to etch 2 housing halves at one time. Figure 4-18 shows the tank with the two halves clamped in place. The tank has two handles for ease of tilting (emptying) and a spout to pour the etchant back into its container.

The housing halves are wax-coated and the 3 electrode areas left bare. This is accomplished by sticking 3 exactly cut discs into the circular grooves (moat) area, which define the positions where the electrode depressions will be etched. After the wax coating is completed, the 3 masking tape discs are removed. A careful inspection under a microscope is needed to assure that no lifting of the wax took place by the disc removing, which would cause under cutting more etching area than permissible.

The etching is performed at room temperature, without agitation, using Hydrogen Fluoride 49% for 19 min. After the etching is completed, the tank is

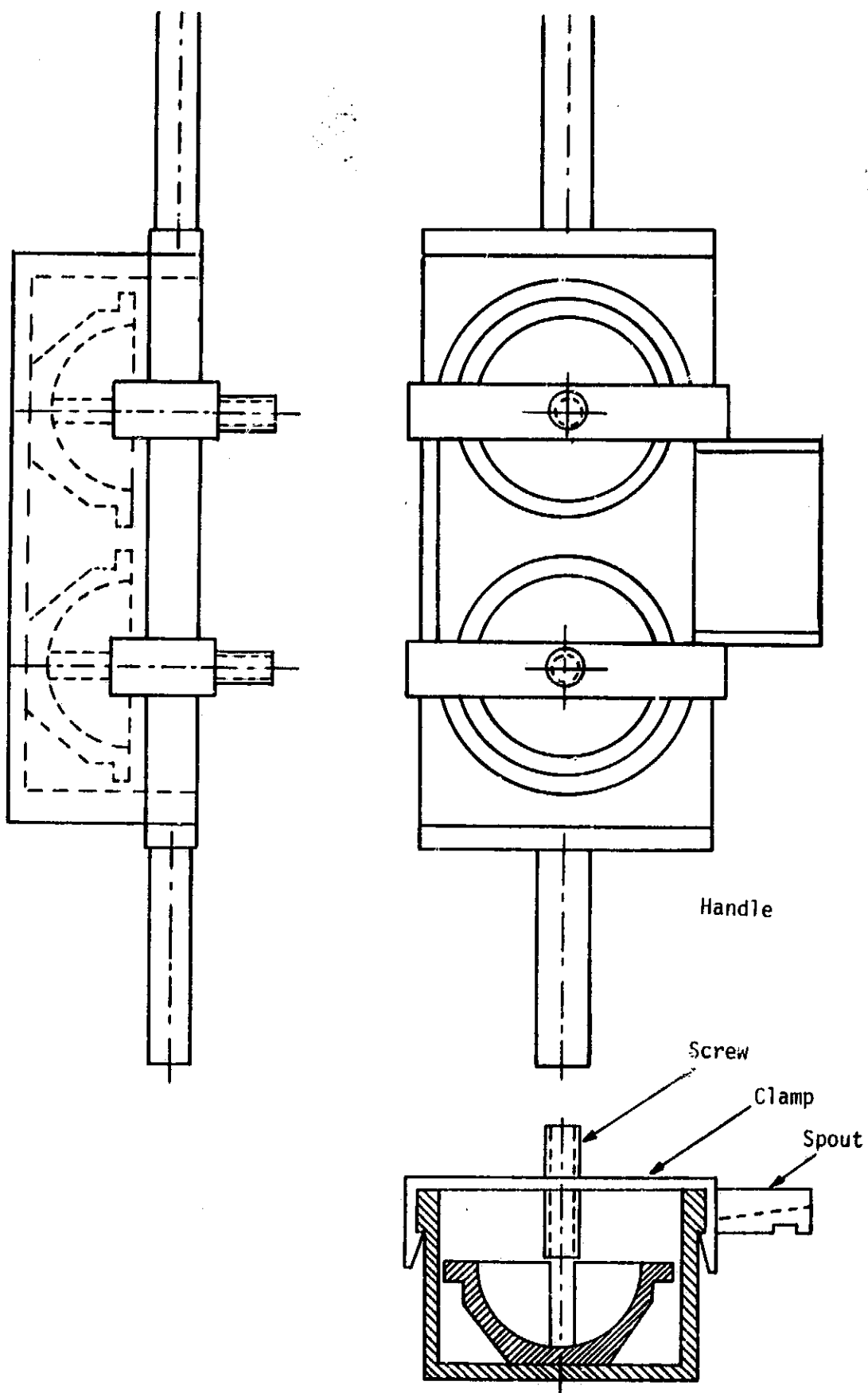


FIGURE 4-18. ETCHTANK (TEFLON) WITH HOUSING HALVES INSTALLED

emptied and vigorously rinsed with tap water. Then the wax must be removed and the housing halves carefully cleaned.

8. Inspection of the Etched Areas

First, a close examination of the etched electrode areas is performed under a microscope to check the rims for imperfections and the areas for uniformity. Then, measurements and recordings are made of the depth and shapes of the areas with a Talyrond or similar machine. Readings are taken at 3 different latitudes in the housing cavity and recorded on polar charts. The stylus of the Talyrond rotates within the cavity and measures in nearly a horizontal direction. The reading must be analyzed to arrive at the real depth of the electrode in radial direction from the cavity center (see Figure 4-19). It is also important to measure the position of the stylus (Latitude) in the cavity to an accuracy of 25 μ .

Table 4-4 gives the depths of the six electrodes in the two housing halves. The depth figures have limited accuracy due to the tolerances of the various instrument elements involved in measuring, recording, and evaluation, e.g., spindle looseness and out of roundness. The stylus swings in an arc rather than moving straight which causes a small error in recording. Also, the arm of the stylus is not exactly perpendicular to the housing dividing plane. The vertical distance from the dividing plane (latitude) is measured with limited accuracy (25 μ). Since the evaluation of the polar charts has its limitations, the depth of the six electrodes is likely more uniform than the figures in the table indicate.

9. Conclusions

The first gyro housing Type 77 was coated with bees wax and the bare electrode areas were etched with hydrofluoric acid 49% for 19 minutes. This removed a layer of 28.4 μ m from the quartz surface with a tolerance $\pm 1 \mu$ m. The surface finish is equal to the 25 x 25 mm² flat samples which range from .5 to

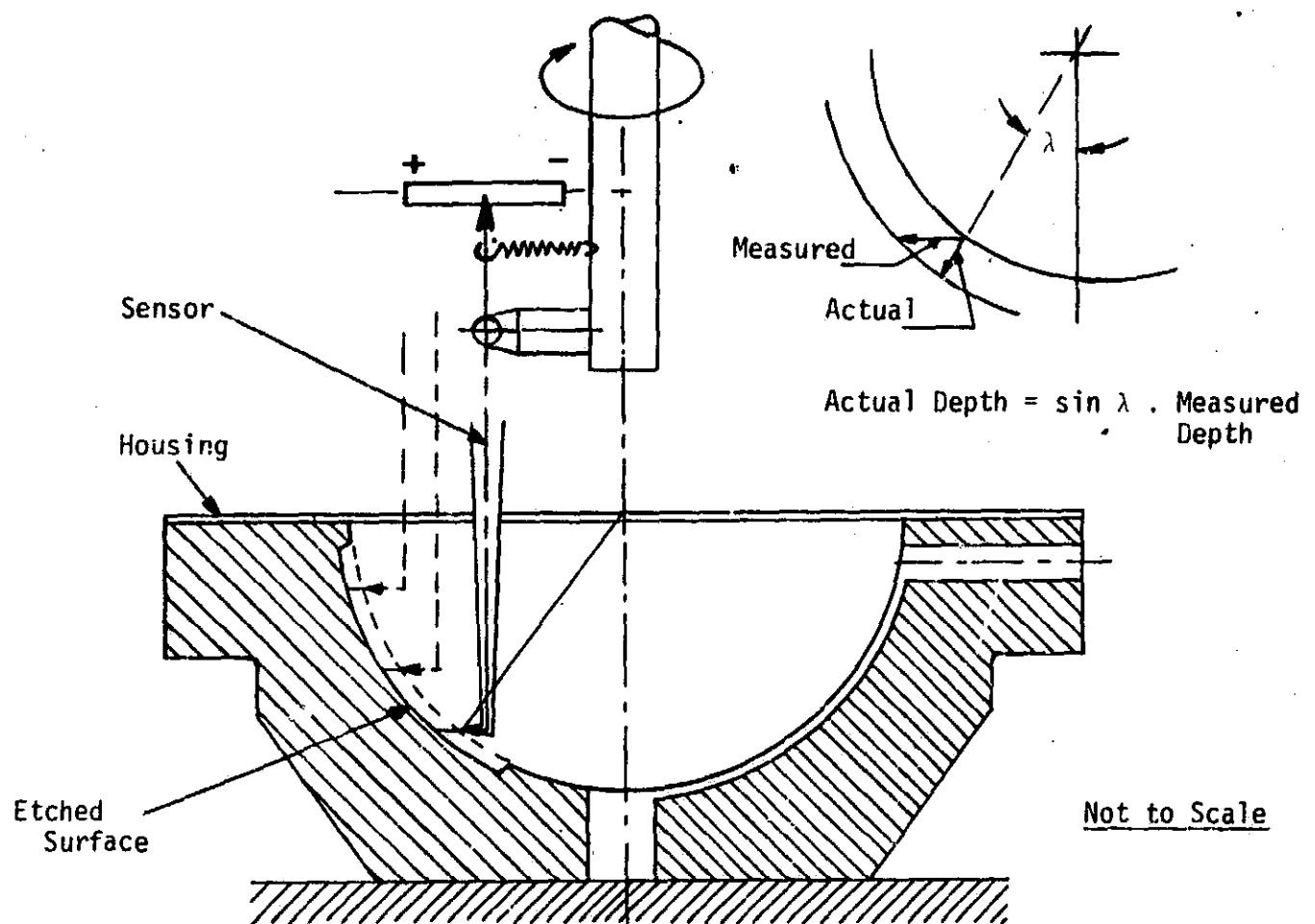


Figure 4-19 Talyrond Measuring Setup. The Housing is stationary. The Sensor is rotating.

Table 4-4

Electrode Depths in Housing Halves I and II

Housing No.	Electrode No.	Radial Depth μ	Average μ	Δ from Average μ	%
I	1	27.8		-.5	-1.77
I	2	27.6	28.3	-.7	-2.47
I	3	29.4		+1.1	+3.89
II	1	27.5		-1.1	-3.85
II	2	29.1	28.6	+0.5	+1.75
II	3	29.2		+0.6	+2.10

.85 μm. (The surface finish of the spherical electrodes in the cavity were not measured.) The chemical etching of the electrodes has substantially improved the dimensional quality and saved much time as well.

V. SUSPENSION ELECTRODES

1. Functional Requirements

The gyro rotor is suspended and centered by electrostatic pull forces from three circular electrode-pairs in three orthogonal axes. An electric suspension network performs the levitation and centering at about 20 KHz. The weight of the rotor is 63 g. A practical working distance of rotor to electrode was found to be about 25 microns (0.001 inch). The size of the electrode area should be as large as mechanically possible and the shape concentric to the rotor. The tolerance of their location is very critical because of the small clearance of .00025 cm (.0001 inch), between rotor and cavity. This also restricts the permissible tilt error of the electrode to the rotor surface. A tilt angle of only .0001 in .750 is equal to 0.0076° or 2.7 arc sec and is enough to cause interference of rotor and seal. The meeting of the required dimensions presents manufacturing problems. A further requirement is to contour the edge of the electrode away from the rotor to minimize or eliminate the danger of electric arcing. For this the same reason it is desirable to have the electrode area well vented so as to reduce the pressure buildup. In the early stage it was a problem to make and maintain high electrical conductivity between the electrode and its contact screw which will be discussed later.

2. Electrode Designs and Manufacturing

It was clear that the electrode surface would need a distance from the rotating ball, which is greater than the gas-seal gap of 0.00038 cm (0.00015

inch). A distance of 0.0025 cm (0.001 inch) was considered practical. Also, the rotor should not make contact with the electrode while at rest even for the case that the rotor be sitting exactly centered over an electrode. By calculation the difference of the sagittas of rotor and cavity for a 0.750 inch electrode is 0.00017 inch. This is little compared to the 0.001 inch recess of the electrode.

The diameter of the electrodes is limited by the area the spin-up channels and their seals. One is tempted to design maximum area electrodes by using the available areas regardless of shape. This leads to triangular electrodes and it multiplies the complexity of having their area centered on the orthogonal axes. Therefore, we stayed with the convenient circular form.

The close tolerances for location and concentricity of the electrodes caused problems in manufacturing. As a first approach the electrode areas were lapped with some imporvised fixturing. After considerable effort with results of poor quality, it was recognized that a machine was needed with proper indexing equipment to have a chance for better locating the electrode in the housing. The lapping spindle was placed off center for more uniformly covering the electrode area but it was still not possible to lap the area strictly concentric to the rotor and to uniform depth. Parallel to the strong lapping effort, a design was made using a solid metal electrode with center shaft for fastening and electrical contact (see Figure 4-20). The solid metal electrode had turned off edges, no contact problem, no spark problems, but it was a mass of metal in a quartz environment which causes thermal expansion problems. Also, the gap adjustment was not easy.

The present and final approach to provide the proper substrate for the electrode metal coatings is by chemical etching. Location and turned away rim area of the electrode is provided by ultrasonic machining with high precision tool room equipment. Extensive tests were made to study and confirm repeatabi-

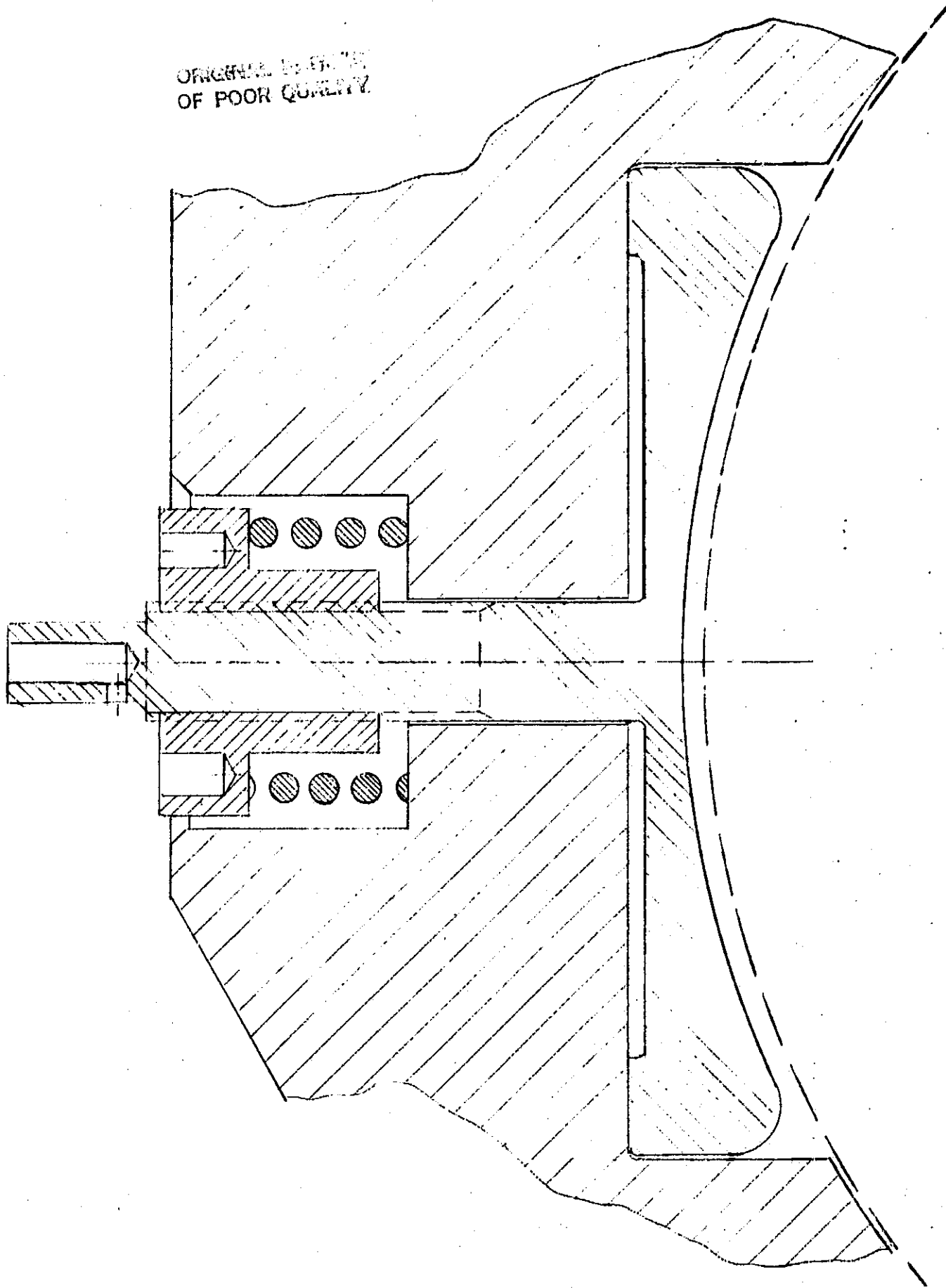


FIGURE 4-20. SOLID TITANIUM ELECTRODE

lity, close tolerances and fine finish. The previous section reported on details and results of the chemical etching.

3. Electrode - Metal Coating by Sputtering

A mask was prepared for sputtering one electrode at a time. The mask covers all areas of the cavity including the flange not to be coated. At the rim of the electrode is a tightly fitting ring pressed against the outer edge of the electrode area by the mask to avoid sputtering in unwanted places. The mask is held in place by outside clamp screws. The first layer sputtered is titanium about 500 to 1000 Å thick to promote bonding of the heavy copper layer (3-4000 Å) for conductivity when not operated by cryogenic temp. The third and last layer is either titanium against copper for corrosion protection or niobium as a super conductive layer for levitation at cryogenic temperature. Before the sputtering operation the cavity has to be cleaned to make adhesion of the metal to the quartz possible.

4. Inspection of the Coated Electrodes

It was found to be necessary to inspect the electrodes before and after ultrasonic cleaning for adherence and blisters of the metal coatings. The best method is a jerk test with masking tape. The surface has also to be inspected for minute imperfections under a microscope. In some cases a polishing operation is needed to remove visible protrusions.

F. Connector Design for the Electrostatic Suspension Electrodes

The design of the electrical connection between the electrode-surface and the connector screw is based on mechanical spring force. From experience with contact applications in other fields of technology in a range from $\pm 100^\circ$ to -100°C , low contact resistance of $1 \text{ m}\Omega$ or less can be accomplished and maintained if the contacting metal surfaces are clean (not oxydized) and a pressure of at least 700 kg per cm^2 (10,000 psi) is maintained. The increase or reduction of the pressure at cryogenic temperatures depends upon the design con-

figuration and the behavior of the materials used. The amount of current which can be transferred is a function of contact area and heat dissipation. While 6 Amp per 1 mm^2 copper is permissible for house wiring, electrical contacts may carry as much as 20 Amp per mm^2 for short time intermittent operation.

1. Form and Dimensions of the Contact Elements

The head of the contact screw has a taper of $\pm 60^\circ$ and a spherical cavity to conform with the sphere to be suspended (see Figure 4-21). The edge of the screw head is rounded to reduce the danger of arcing. The screw is made of beryllium-copper and is coated with a high conductivity non-corrosive metal. The seat for the contact screw in the center of the electrode is tapered $\pm 45^\circ$ and makes contact with the screw head by a narrow tapered ring. This is purposely designed this way to create a high specific pressure. The earlier housings had spherical seats for a fitted spherical screw head, thus having a large contact arc and very low contact pressure.

Above the contact area near the seat edge is a somewhat thinner metal deposition due to shading effect during sputtering. This thin area adds electrical resistance and restricts heat dissipation, both of which are most undesirable.

2. The Spring Force and Stress

The contact spring is wound of beryllium copper alloy 172 wire and heat treated to half hard condition. The spring ends are ground flat. The installed spring is 2 mm compressed by turning the nut about $4\frac{1}{2}$ turns, which produces about 2 Kg force. The resulting stress in the spring wire is

$$\sigma_T = f \times d \times G / 4 \pi n r^2 = 4086 \text{ Kg/cm}^2$$

(See Hütte I Torsion Springs, Page 715)

f = 2 mm compression

d = .079 cm wire diameter

$G = 5.2 \times 10^5$ material constant kg/cm^2

n = 4 number of coils

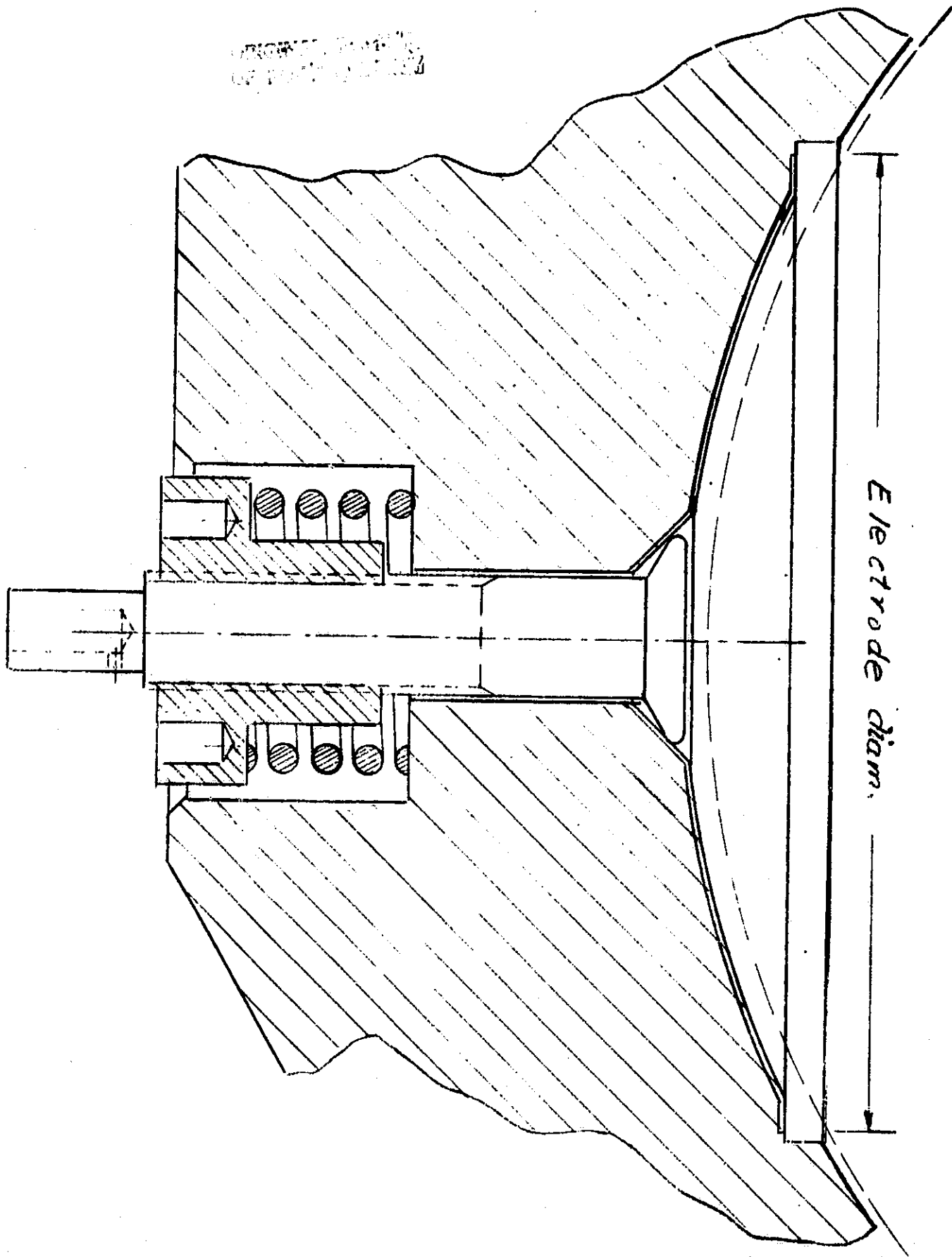


FIGURE 4-21. ELECTRODE - CONNECTOR

$r = .2$ cm spring radius

Since σ_{max} for beryllium copper 172 is $12,000 \text{ Kg/cm}^2$, the stress in our spring is safe.

The spring force $F = \pi \times d^3 \times \sigma_T / 16 \times r = 2 \text{ Kg.}$

The spring characteristic $C = F/f = 10 \text{ Kg/cm.}$

3. The Electrical Contact Force and Area

The spring force of 2 Kg acts against a conical seat of $\pm 45^\circ$, therefore, the contact force is $2 \times \sqrt{2} = 2.8 \text{ Kg.}$ The contact area can be approximately calculated by using the formula for "contact of two cylinders." In our case, the two cylinders are not straight, but curved to form two circles - the cylinder becomes a toroid. The contact width

$$a = 3.04 \frac{F}{E} \frac{x}{L} r \text{ cm, contact zone width}$$

$$F = 2.8 \text{ Kg} \quad \frac{1}{r_1} = \frac{1}{r_1} + \frac{1}{r_2} + \frac{1}{.0127} + \frac{1}{\infty}$$

(see Dubbel I, page 412)

$$r = .0127 \text{ cm}$$

$$E = 1.04 \times 10^6 \text{ Kg/cm}^2 = \frac{2E \times E}{\frac{Q}{E+E} \frac{\text{BeCu}}{Q} \frac{\text{BeCu}}{Q}} = \frac{2 \times 0.73 \times 1.8 \times 10^6}{0.73 + 1.8}$$

$$L = 1.256 \text{ cm} \quad L = .4 \text{ contact dia.} \times \pi$$

$$\text{Contact width } a = 5.14 \times 10^{-4} \text{ cm}$$

$$\text{Contact area } L \times a = .000645 \text{ cm}^2.$$

The contact pressure $2.8 \text{ Kg} / 6.45 \times 10^{-4} \text{ cm} = 4341 \text{ Kg/cm}^2$ or $63,800 \text{ psi}$, promises very low electrical resistance.

4. Calculation of the Contact Resistance

The contact area calculation above shows a narrow flattening of the contacting beryllium copper by the much harder quartz seat. The area is $6.45 \times 10^{-4} \text{ cm}^2$, which offers a constriction to the current flow. The total contact resistance consists of several phenomena, the major ones being: surface contaminations, tunnel effect through insulating oxide layers and constriction. Only the last, constriction resistance, can in simple cases be calculated with some degree of accuracy. See Ragnar Holm-Electrische Kontakte, Verlag - Springer, Berlin, 1958.

Formulas have been developed by Ragnar Holm for the constriction resistance of two crossing cylindrical bars (wires) and of a sphere pressed into a flat surface. Our case is a metallic toroid pressed into a 90° cone of metal coated quartz. The calculation is based on the assumption that the material will yield till the area of contact is so large that the contact pressure is equal to the contact hardness. We approximate our case as a flat surface in contact with a sphere.

$$a = \frac{P}{3\pi Y}$$

a = contact area radius
P = Force
Y = Yield strength

$$a = \frac{2.8}{3\pi \cdot 10^4}$$

$$a = 0.0055 \text{ cm}$$

The constriction resistance of both surfaces together would be

$$R = \frac{\rho_1 + \rho_2}{4a} \quad \rho_1 = 7.8 \times 10^{-6} \Omega \text{ cm BeCu}$$
$$\rho_2 = 2 \times 10^{-6} \Omega \text{ cm coated copper}$$

$$R = \frac{9.8 \times 10^{-6}}{4 \times .0055}$$

$$R = 0.0004 \Omega$$

From this result of $.4 \text{ m } \Omega$ with a sphere against a flat surface, we can assume that the resistance of our electrode contact may be of a similar magnitude, say between 0.1 and $1.0 \text{ m } \Omega$.

The resistance of the contact screw (# 2-56, 0.8 cm effective length) is found from the beryllium copper material electrical resistance of $7.8 \times 10^{-6} \text{ } \Omega \text{ cm}$, a resistance of $0.24 \text{ m } \Omega$ is thus calculated for the contact screw. The resistance of suspension electrode plating is calculated based on an electrode diameter of 1.9 cm and connection diameter .4 cm.

Assuming an average flow path length of .45 cm and copper of $5 \times 10^{-4} \text{ cm}$ thickness, we find the resistance of the plating to be given by

$$R = \frac{.4 \times 10^{-2}}{57 \times .188} = .00037 \text{ } \Omega$$
$$= 0.4 \text{ m } \Omega$$

Total Resistance is thus given as the sum of

Electrode plating	$\sim .4 \text{ m } \Omega$
Contact - constriction, etc.	.4 to $1.0 \text{ m } \Omega$
Screw shank	.2 to $.3 \text{ m } \Omega$

Considering some uncertainties in material data and calculation methods, the total resistance may be as high as $2 \text{ m } \Omega$.

Actual resistance measurements will be made when a sample of this contact design becomes available. More important than the low value is the constancy of the resistance based on the very high pressure of 4340 Kg/cm^2 (63,800 psi) effected by the contact spring force of 2.8 Kg and its spring constant of 10 Kg/cm.

5. Summary of Contact Data

Spring force: 2.0 Kg

Electrode plating resist.: .4 m Ω

Spring stress: $\sigma_T = 4086 \text{ Kg/cm}^2$

Total resistance: 1 to 2 m Ω

Spring construction: C = 10 Kg/cm

Spring compression: = 0.2 cm

Electric contact force: 2.8 Kg

Contact area: $6.45 \times 10^{-4} \text{ cm}^2$

Contact pressure 4341 kg/cm²

Constriction resistance: .4 m²

Contact screw resistance: .24 m Ω

6. Assembly Procedure for the Suspension Electrode Contacts

Before the parts can be assembled, a careful dimensional check is necessary.

- (a) Compress 2 mm.
 - (b) Force exerted should be 2 Kg.
 - (c) Calculate spring constant. Should be 1 Kg/mm.
 - (d) Check dimensions and surface finish of contact screw head.
 - (e) Measure torque needed for 2 mm compression; use torque test spacer with seat for contact screw head. The same torque should be used for final assembly.
 - (f) Assembly and Adjustment:

The contact screw head must not rotate in its electrodes seat during assembly and pressure adjustment, because the delicate electrode metal layer might be damaged. Use pin vice to prevent the screw rotation during adjustment.

(g) Soldering:

When soldering the lead wire to the contact screw, keep solder from running into the 2-56 thread. Use antiflux or teflon washer.

VII. GYRO ROTOR

1. Dimensional Requirements

As a compromise of functional requirements and attainable manufacturing accuracy, the rotor should fit to the housing cavity with a clearance 0.000254 to 0.000508 cm (.0001 to .0002"). The gyro design is based on a standard rotor of 3.810000 cm (1.500000") diameter. This means the seal diameter of the cavity is 3.810381 ± 0.000127 cm (1.500150 \pm 0.00005 inch).

2. Material Requirements

The dimensions of the rotor must be extremely stable over time and temperature. This demands the rotor material must be completely annealed, stress free. For concentric rotation without any amount of wobble, the rotor material must have highest homogeneity, no bubbles and no density variation of detectable magnitude. It is also most desirable to use material of low density. For test purposes hollow rotors were made to ease the levitation problem.

3. Material Selection

Large astronomical telescope mirrors have similar material requirements as we do for our gyroscope (housing and rotor). Special materials have been developed for telescope such as Cervit, Zerodur and other ultra low expansion (positive and negative) glasses or glass-ceramic materials. All gyros used in the program were made of fused silica, a low expansion material widely used in cases where highest stability is most important. The various types of fused silica differ in purity, bubble size and number, and homogeneity of stress. Some basic data for quartz are given in table 4-5 and table 4-6.

Table 4-5. Properties of Some Candidate Materials

	Quartz Natural	Quartz Fused	Cervit 126
Density g/cm	2.65	2.2	2.51
Hardness Mohs	6.3-7.0	4.9	
Tensil Strength $\times 10^3$ PSI		7.0	
Compressive Strength $\times 10^3$ PSI		160.	
Elasticity E $\times 10^6$ PSI		10.4	12.3
Therm. Expansion $^{\circ}\text{C} \times 10^{-6}$		0.55	-.35
Index of Refraction		1.4585	
Sonic Attenuation db/ft/mc		0.033	
Internal Damping		1×10^{-5}	
Annealing Temp $^{\circ}\text{C}$		1140	
Softening Temp $^{\circ}\text{C}$		1670	

Table 4-6. Fused Silica Data

Comp	Grade	Homogen Δn	Strain	Bubbles $%/\text{cm}^2/\text{cm}$	Bubbles mean dia inch
Amersil	T19 suprasil	5×10^{-6}	8	.00013	.012
	T15 Homosil	2×10^{-6}	5	.00013	.012
	T32 SR optical	10×10^{-6}	10	.005	.020
	T31 SR commercial	-----	20	.012	.080
Corning	optical Schlieren	3×10^{-6}	10	.005	.020
	UV Schlieren	3×10^{-6}	10	.005	.012
	optical Grade 1	3×10^{-4}	10	.005	.012
	optical Grade 2	3×10^{-4}	10	.020	.012
	industrial grade	-----	20	.120	.012

VIII. MACHINE AND CONTROLS FOR FINISHING HIGH PRECISION QUARTZ BALLS

1. Summary

This section describes a 4 cup lapping machine for finishing balls to a roundness of 10^{-6} diameters or better. The lapping cups are spaced in tetrahedron fashion for maximum size and uniform distribution. A 4 cam control mechanism switches the sense of rotation of the four lapping motors in a special way to achieve maximum uniformity in surface coverage of the ball by the lapping cups. Motor rotation-combinations which would produce a ball rotation in or near to a cup axis are avoided. Lapping tests have produced roundness beyond our present measuring capabilities, 2.5×10^{-6} cm. Figure 4-22 shows a picture of the Lapping Machine and Figure 4-23 shows a closeup of the lapping process.

2. Requirements and Application

The machine is designed to produce in a reasonable time small quantities of extremely high precision balls for very special purposes. Our present requirement is a 38.1 mm (1.5 inch) sphere to be used as flywheel for a gyroscope, made of fused silica. The roundness of this sphere is to be as high as possible, but not less than 2.5×10^{-6} cm (10^{-6} inch). The surface finish must have optical quality and be free of any imperfections. In addition, gauge balls of extremely high roundness are needed to check the roundness of spindle bearings for measuring and testing equipment.

3. Material for the Precision Ball

Dimensional stability from 200°C to near absolute zero over several years is required. The time span includes development, manufacturing, testing, storage, and one year of orbital flight. Clear fused quartz SiO₂ was selected because it seems to have the best stability over temperature and time and much experience in handling it is available. The best grades must be used with

ORIGINAL PAGE IS
OF POOR QUALITY

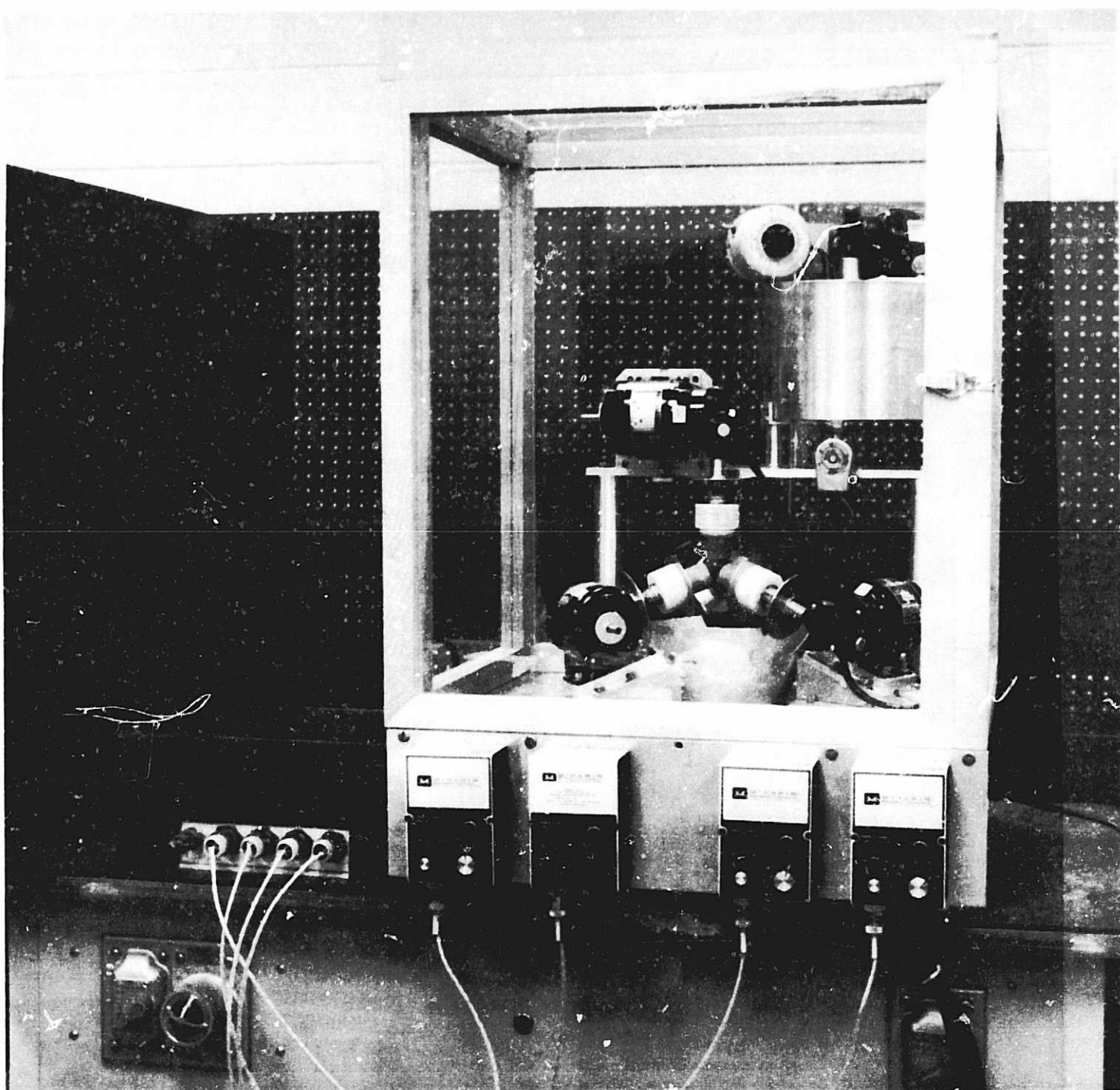


FIGURE 4-22. THE FOUR-LAP LAPPING MACHINE

ORIGINAL PAGE IS
OF POOR QUALITY.

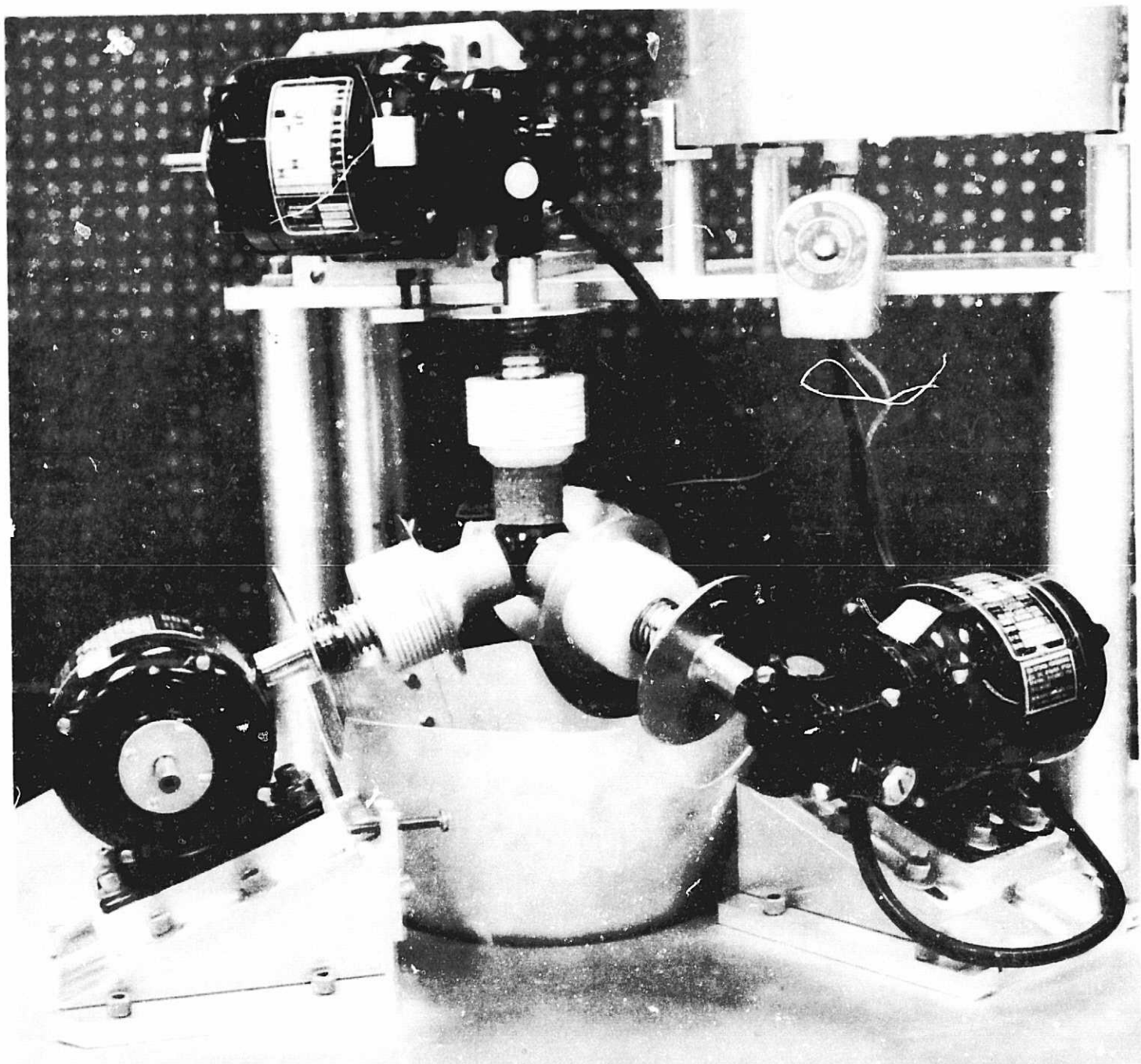


FIGURE 4-23. CLOSEUP OF THE LAPPING PROCESS

regard to uniformity of stress (refracting index) and contaminations. Sources for fused quartz are in alphabetical order:

Amersil, Inc. 685 Ramsey Ave., Hillside, N. J. 07205

Corning Glass Works, Corning, New York 14830

Owens-Illinois, Inc., Toledo, Ohio 43601

and others. The basic quartz data is given in table 4-7.

Table 4-7. Basic Quartz Data

Density	2.2 gr. cm^{-3}
Tensil Strength	500 Kg. cm^{-2}
Compressive Strength	11,200 Kg. cm^{-2}
Young Modulus E	.732 Kg. cm^{-2}
Thermal expansion	.55 x 10^{-6} /°C 20°C to + 320°C (crossover temperature)
expansion is zero at -166°C	
Thermal Conductivity	.0033 cal/cm ² /sec/°C/cm
Specific Heat	.18 cal/gr
Fusion temperature	1800°C
Softening Temperature	1670°C
Annealing Temperature	1140°C
Strain Temperature	1070°C
Dielectr. Const.	3.75 up to 100 MC
Index of Refraction	1.4585 for 4876 Å

4. History of Ball Lapping Devices

Ball-lapping devices have been made for ages. Thousands of years ago, the Chinese made beautiful balls of Indian ivory by carving them round with primitive tools and finishing them at the square ends of one or two sticks of bamboo.

MSFC has made sophisticated ball-lapping machines of different types and sizes. The largest one was for a 25 cm ball of aluminum. The ball and its cap, which was also finished in that machine, was used as an airbearing for a space simulator with three degrees of rotational freedom and a load capacity of over one ton. We have also made a few balls for the National Bureau of Standards, Washington, D.C. Their balls are 6.35 cm in diameter and are made of opaque fused silica to be used to define the precise density of that material (because the volume of a ball can be more closely measured than the volume of any other geometric form).

Our present effort is, and has been for some time, to make spherical gyro rotors of fused clear quartz with 3.81 cm diameter to be used for the Schiff relativity experiment, conceived and developed at the Stanford University in California. It is a NASA project called Gravity Probe B (GPB).

5. Problem Areas

The major problem areas in meeting the requirements of the GPB gyro rotor are as follows:

- (a) The quartz should be free of stress or at least uniform in stress. Non-uniformity will, in time, relax and cause changes in roundness.
- (b) Another problem is to make accurate diameter and roundness measurements to 1 part per 100,000 and 1 part in a million, respectively.
- (c) The overriding problem in the past has been the intelligent control of the lapping machine to produce, in an acceptable time, the required roundness of the ball.
- (d) It was difficult to accomplish roundness before the right diameter was reached unless one started with a ball of much oversize, which meant days or weeks of polishing. It was obvious that a much more efficient finishing method was needed.

A careful investigation of the actions of the lapping cups and the ball motions brought better understanding of the lapping problem and resulted in a new control mechanism for the lapping machine which is explained later in this report.

6. Description of a 4-Cup Ball-Lapping Machine - Tetrahedron Type

The machine has 4 low-speed DC reversible motors, arranged in tetrahedron fashion, with 109.47° angles between their shafts. Each motor has a spring-loaded lapping cup axially floating at its shaft end and is pointing to the tetrahedron center (see Figure 4-24). The three lower motors (B, C and D) are spaced 120° as seen from above and tilted with their shafts upward 20° . The upper motor "A" is pointing straight down. The forces of the 4 cups must hold the ball in the center of the tetrahedron and should be the same. The downward force of cup "A" is compensated by the forces of cups "B", "C", and "D" but their forces are higher to compensate for the weight of the ball. The individual spring forces and lapping forces are listed in Table 4-8.

Table 4-8. Lapping Cup Force Tabulation

Lapping Cup "A"

Spring Weight	5 gr
Flexible Cupholder	55 gr } 90 gr
Pitch Lapping Cup	30 gr
Spring Force	200 gr
Total Lapping Force	290 gr

Lapping Cups "B", "C", or "D" --
tilted up 20°

Lapping Force "A"	290 gr
Ball Weight	64 gr
Total Down Force	354 gr
divided by 3 ---	118 gr to be carried by each one of the lower cups
Force at 20°	$118 \text{ g}/\sin 20^\circ = 345 \text{ gr}$

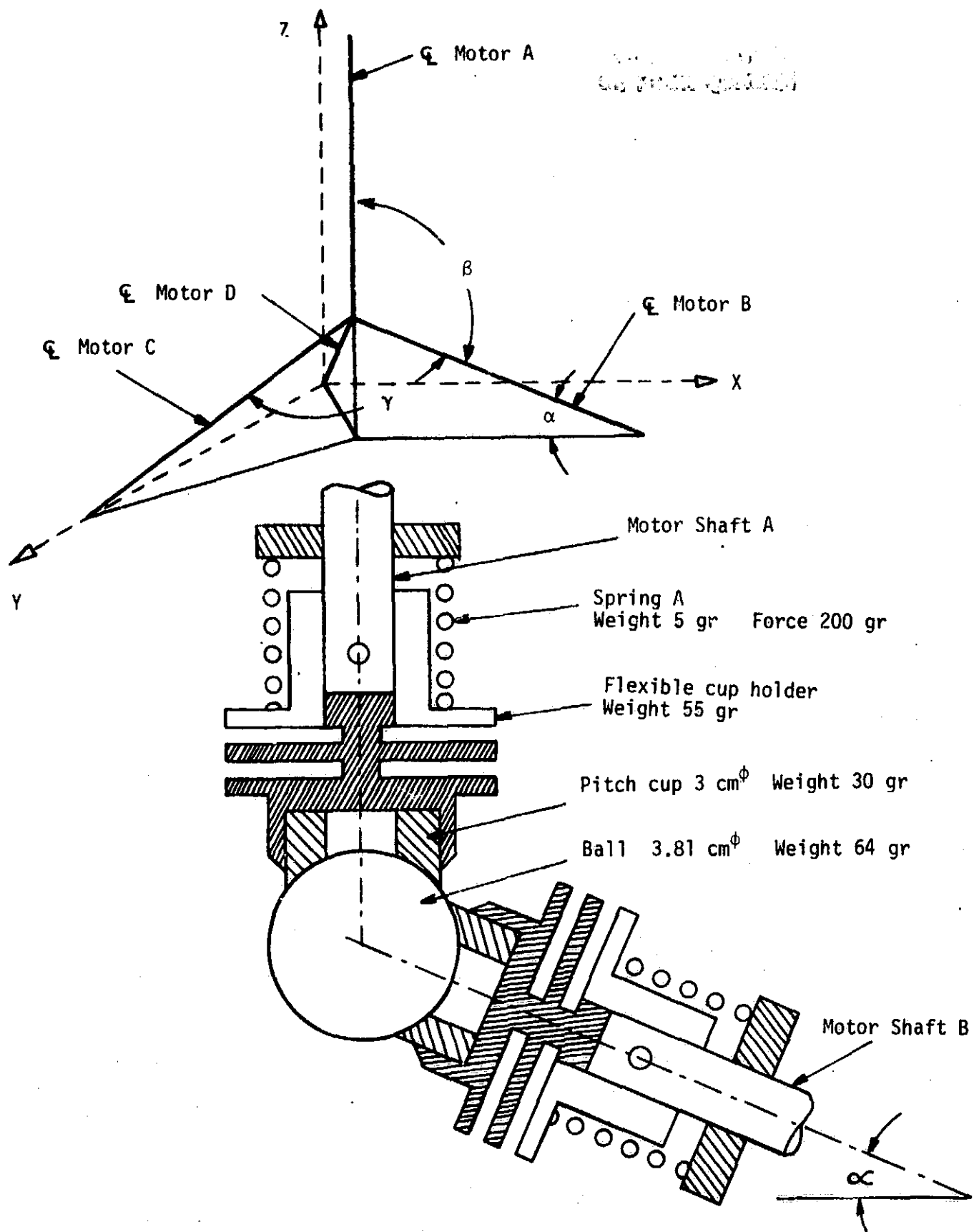


FIGURE 4-24. DETAIL OF THE GEOMETRY AND DESIGN OF THE LAPPING MACHINE

$$\frac{\text{Force to hold cup, etc. } 90 \text{ g} \times \sin 20^\circ = 31 \text{ gr}}{\text{Spring Force "B", "C", or "D"} = 376 \text{ gr}}$$

To hold the ball in the center of the tetrahedron, the force of the lower 3 cups has to be 345 gr as compared to the upper cup of only 290 grm.

It has an advantage to have maximum coverage of the ball surface by the lapping cups because larger cups (near the diameter of the ball) have a much better chance to make the ball round. Table 4-9 gives some typical figures on coverage.

Table 4-9. Leverage Versus Cup Arrangement

Cup Arrangement	Max Cup Diameter	Ball D Coverage %
3 cups in one plane	0.866 D	56
4 cups in one plane	0.707 D	50
4 cups in tetrahedron fashion	0.816 D	66.6

These are theoretical figures. The cups must be a little smaller to give clearance between them.

It is most important that the cups drive the ball in nearly random fashion (with certain exemptions) and to keep the ball always moving. This can be almost accomplished by changing in short time intervals the sense of rotation of the cups in a certain pattern. Since visual observation of the ball movements is nearly impossible, nor is it possible to know which way the ball drifting should go with time. proper hand control of the 4 cup motors cannot be accomplished. Therefore, an automatic device was developed to accomplish a maximum of roundness in a minimum of time.

7. Other Cup Arrangements for 4 Cup Lapping Machines

During the development, a number of other cup arrangements were studied. These are briefly discussed in the following.

(a) Cup Axes in a Horizontal Plane, 90° apart

The weight of the ball is carried only by the lower half of the cups lapping surface. The spring force behind the cup must be increased to keep the entire cup in contact with the ball. Also, the weight of the cup and its holder add to the nonsymmetry of the cup pressure. This uneven pressure is increasing with the ball size more rapidly than the areas of the cups do (R^3/r^2). The pressure limits a cup can stand are given by the cold flow of the pitch. Special refrigeration of the cups during lapping and standstill to keep the pitch from deforming have other ill effects besides uniformity and cost. In short, the horizontal cup arrangement is not good.

(b) Four Cups in a Vertical Plane

One cup is pushing down, one from right and one from left are pushing inward, and the lower cup is carrying the ball weight, the hang down forces of the horizontal cups plus the force from the top cup. The unequal pressure between top and bottom cups could be equalized by adjusting the cup areas according to the load they have to carry; but this requires that the lower cup should be larger than the top cup. This makes the cup control more difficult.

(c) Four Cups in a Vertical Plane with their Axes at 45° to the Horizontal Line (see Figure 4-26).

The lower two cups have to carry the down force of the two upper cups plus the weight of the ball. Some of the forces acting against the ball are tabulated next to Figures 4-25 and 4-26.

A summary of the spring and lapping forces of the three configurations is given in table 4-10. Most 4 cup lapping machines have nonequal cup forces but

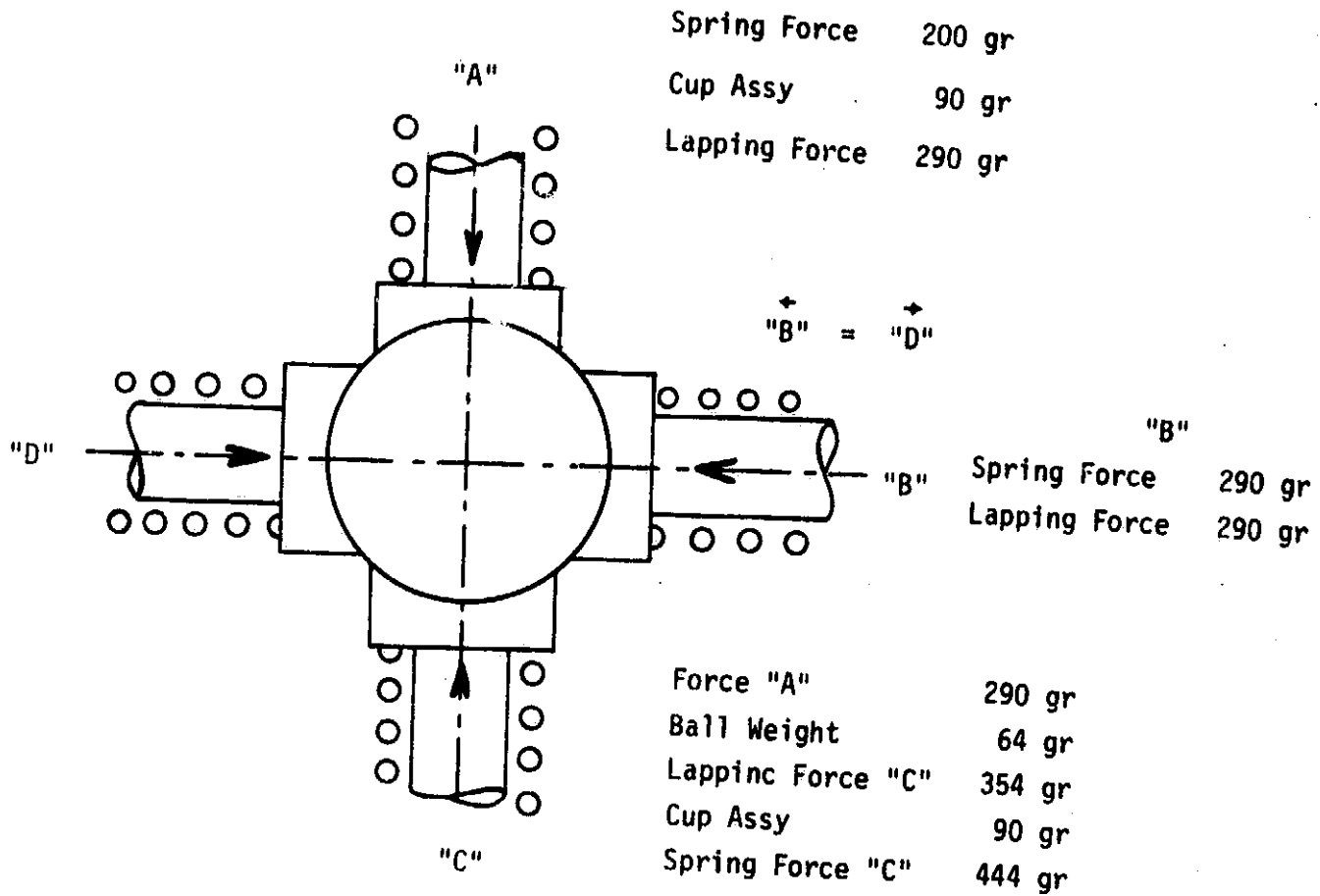
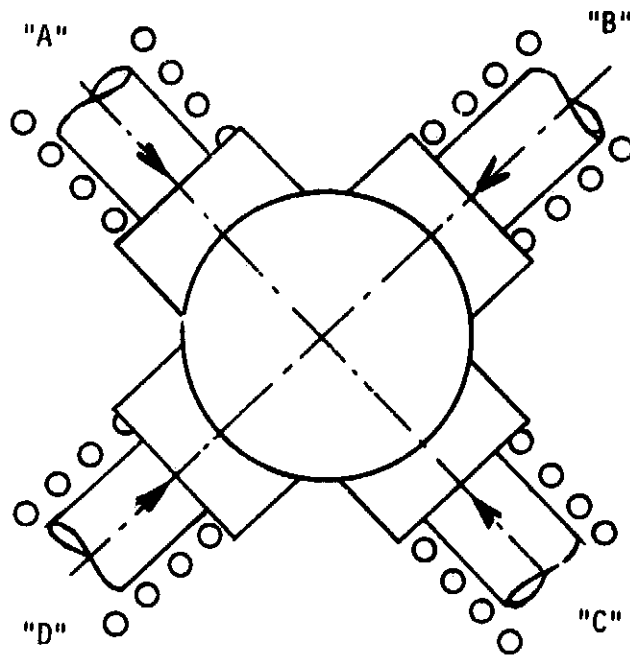


FIGURE 4-25. AXIS PERPENDICULAR AND PARALLEL TO THE VERTICAL.

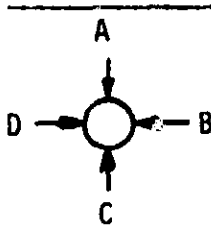
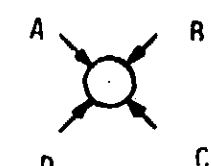
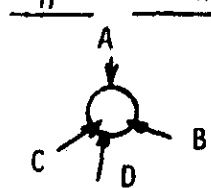


Spring Force "B"	200 gr
Cup Assy / $\sqrt{2}$	64 gr
Lapping Force "B"	264 gr

Lapping Force "A"	264 gr
Ball 64 / 2 $\sqrt{2}$	23 gr
Lapping Force "C"	287 gr
Cup Assy / $\sqrt{2}$	64 gr
Spring Force "C"	351 gr

FIGURE 4-26. AXIS AT 45° TO VERTICAL

having all 4 cups in one plane hinders to some degree the universal tumbling control of the ball-xpin axis.

Figure	Cup	Spring force	Lap force	Average Lap Force Difference
	A B = D C	200 290 444	290 290 354	7% 7% 13%
	A = B C = D	200 351	264 287	4% 4%
	A B = C = D	200 376	290 345	12% 4%

The lapping machine data for a 30 to 75 mm ball are:

4 Reduction gear motors, 115 volt DC, 1/30 HP

Speed of output shaft: 200 RPM, adjustable $\pm 30\%$

Lapping cup diameter: $0.8 \times$ ball diameter

Radial cup force: 200 - 600 gr

Self-aligning cup bearings, timing cycle for cup reversal: 5 sec.

8. Ball Motion Control

The ball is supported and rotated by the 4 lapping cups which can be individually controlled to turn right or left. The speed range is limited by poor lapping efficiency at low speed and by the throwing off of the lapping compound at high speed. Therefore, the speed was set constant at 120 RPM based on experience.

An effort was made to find a series of rotation-combinations for the 4 motors driving the lapping cups to cover most uniformly the entire ball surface. Having 4 cups which each can rotate right or left gives $2^4 = 16$ combinations (see Table 4-11). R and L stand for Right and Left hand rotation of the cups.

Table 4-11. Combination Table

Group	No.	Cup Combination A B C D	Ball-spin axis	Torque Units or Speed
I	1	L L L L	--	0
	2	R R R R	--	0
II	3	R L L L	A _R	2 T ₀
	4	L R R R	A _L	"
	5	L R L L	B _R	"
	6	R L R R	B _L	"
	7	L L R L	C _R	"
	8	R R L R	C _L	"
	9	L L L R	D _R	"
	10	R R R L	D _L	"
	11	L L R R	G _R -K _L	4 $\frac{1}{3}$ · T ₀
	12	R R L L	K _R -G _L	"
III	13	L R L R	I _R -H _L	"
	14	R L R L	H _R -I _L	"
	15	L R R L	E _R -F _L	"
	16	R L L R	F _R -E _L	"

9. Discussion of the Combination Table

The C combinations No. 1 (LLLL) and No. 2 (RRRR) produce no motion of the ball. This can be explained as follows: assume the top lapping cup A is removed. The cups B, C, and D turning all in the same direction (clockwise) will produce a vertical spin vector of the ball with a value of one which is equal to the individual cup vectors of B, C, and D. By adding cup A with its vector "one" relatively in the opposite direction will cancel the ball vector and the ball will stand still. Then, each of the 4 cups would wear a ring groove into the ball surface. Therefore, the combinations 1 and 2 must be eliminated.

The eight combinations No. 3 to No. 10 produce ball rotations about the axis of the cups A or B or C or D. For example: the combination No. 3 (RLLL) -- the cups B, C, and D produce a ball motion about axis A, as above, and in the same direction as cup A. Therefore, there is no lapping action under cup A. Lapping takes place only in the zone 33° north to 73° south (see Figure 4-27). Relative values of lapping actions as a function of latitude are given in Table 4-12.

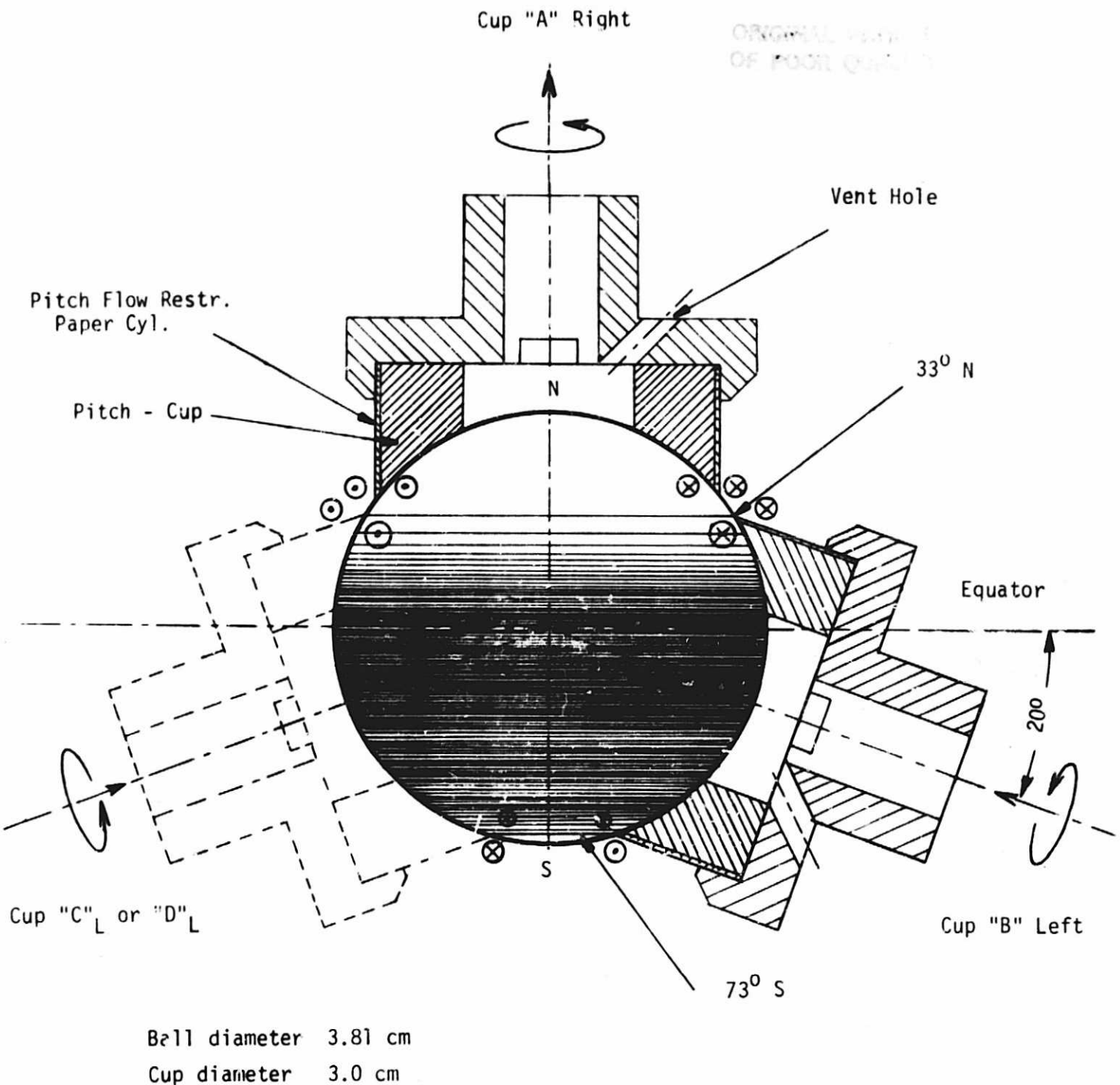


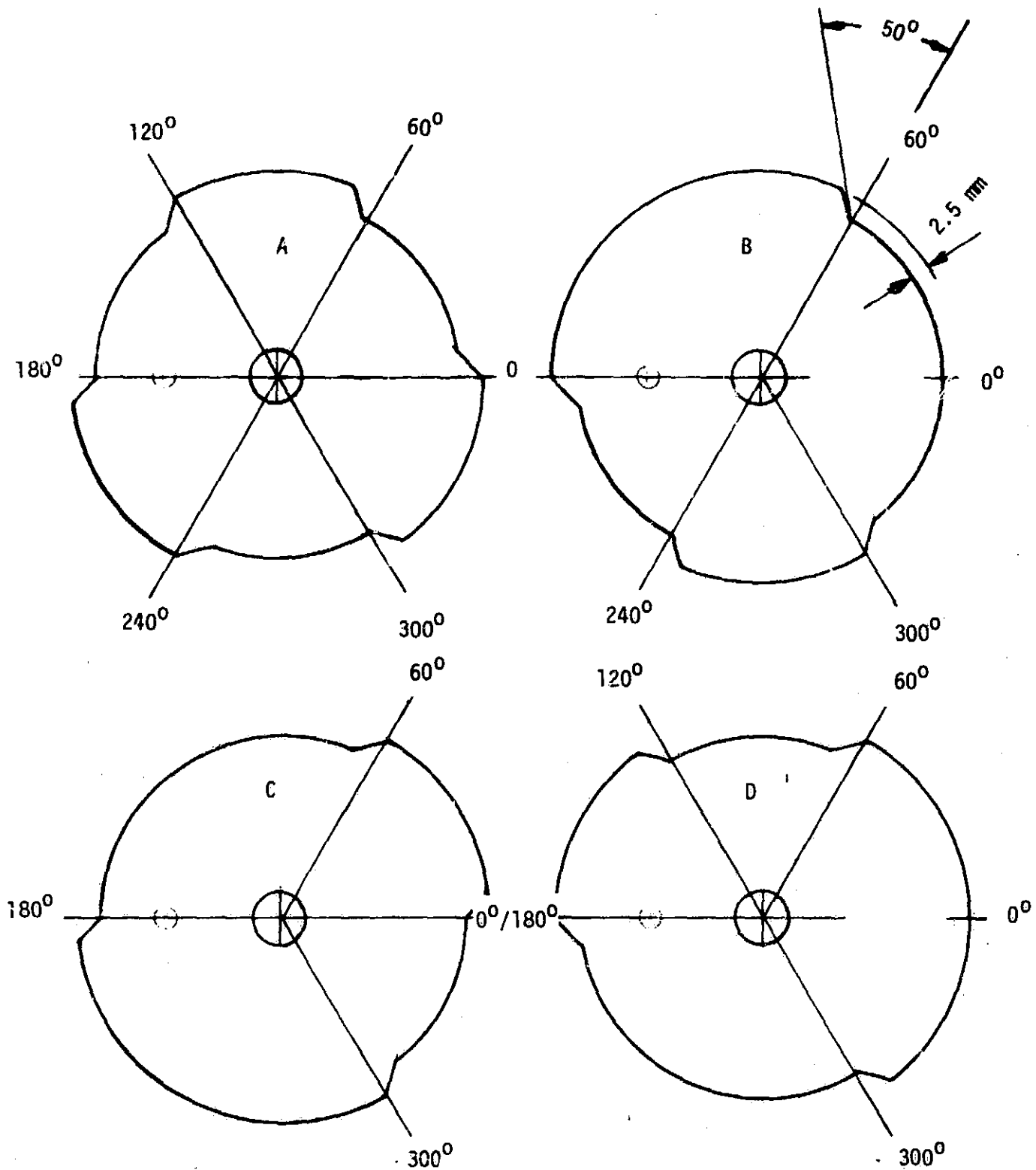
FIGURE 4-27. CUP-ROTATION - COMBINATION NO. 3 A B C D
R L L L

Table 4-12. Lapping Actions as a Function of Latitude

Latitude	Ball Vector	Lap Angle	Cup Vector	Relative Lapping Action
90 - 33° N	→	none	none	none
33° N	→	180°	↗	.05
16.3° N	→	140°	↑↗	1.43
Equator	→	114°	↑↑↗	2.0
20° S	→	106°	↑↑↗	2.0
45° S	→	67°	↑↑↗	2.2
73° S	→	0°	↖	2.38
73 - 90° S	→	none	none	none

The third and last group of combinations No. 11 to No. 16 finally produces ball motions which cause the desired lapping actions. Example: Combination No. 11 - LLRR. Cup A and B together would cause a ball rotation about the center of the A and B axis called "K" axis. Cup C and D would turn the ball about the center of the C and D axis which is the "G" axis. Because of the tetrahedron geometry, the "K" and "G" axes are identical. Figures 4-28 and 4-29 show 4 cam controls used to control the lapping.

The torques of all cups are added in the K-G axes , the ball is rotating. But the coverage of the ball by the cups is not 100% nor is it uniform. A small area at the entrance of the K and G axes is not covered because the lapping cups have only 3 cm diameter instead of the theoretical value of 3.1 cm.



Alum. .125" or 3 mm

FIGURE 4-28. CAMS FOR LAPPMOTOR CONTROL

ORIGINAL PAGE IS
OF POOR QUALITY

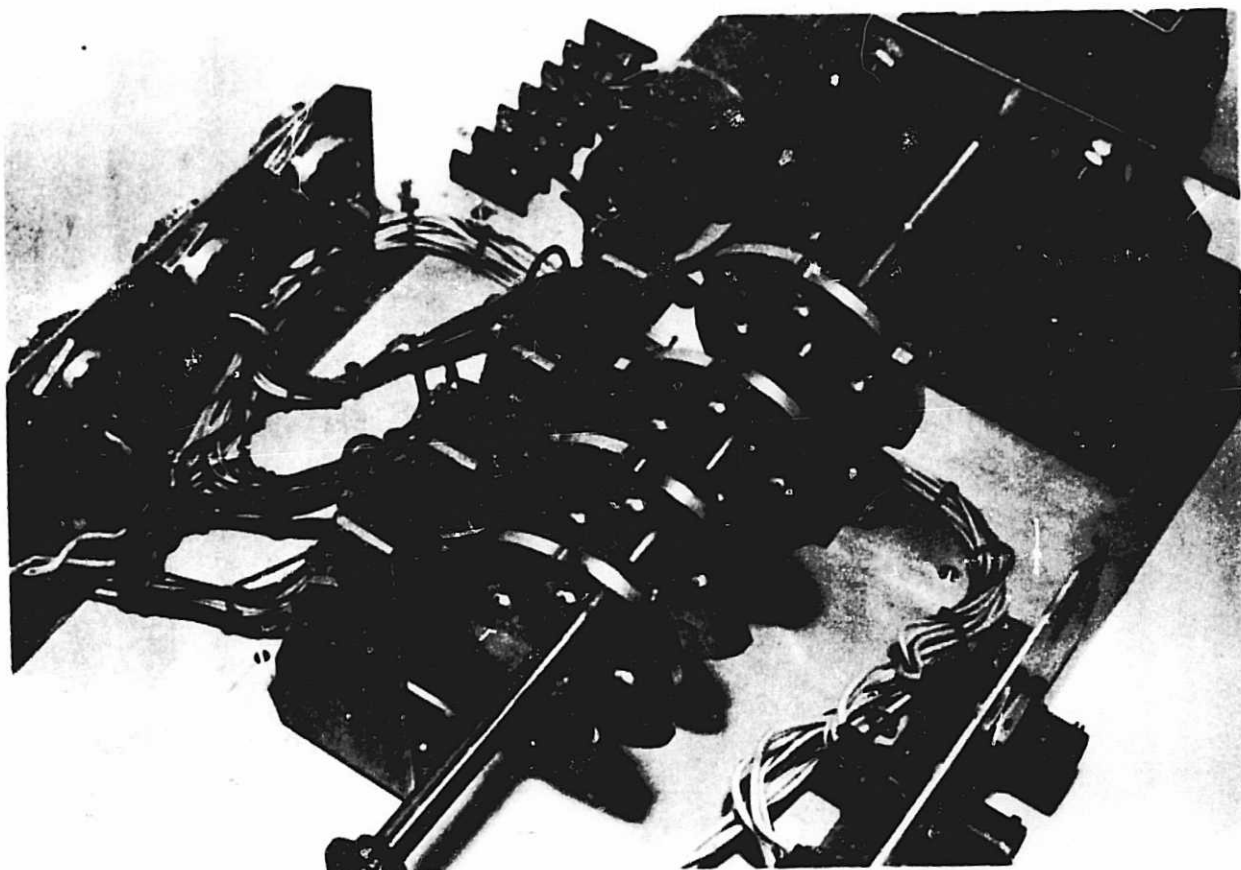


FIGURE 4-29. 4 CAM-CONTROL DEVICE

Ball radius 1.9 cm

Angle between A and B is 109.5°

Maximum cup diameter = $2 \times \sin 109.5/2 \times 1.9 = 3.1$ cm

The small spots of 1 mm diameter at K and G axes will be covered many times over when the combinations change which happens about 360 times per hour.

The speed of ball rotation and the drifting rate of the ball spin axis are much dependent upon the friction of the lapping cups which change with the cup condition, compound consistency, and amount. The motion of the ball is the result of cam control and varying friction. The efficiency of the lapping operation also depends on the care of the pitch laps. More details appear in following sections.

10. Inspection for Stress

At the outset of the ball development for the relativity test project, it was planned to inspect all quartz materials for stresses. However, quartz was offered stress free to $1 \text{ in } 10^6$ maximum variation in the index of refraction, so the stress inspections were dropped.

The excessive fracturing of two balls during gyro spin tests in December '76 and January '77 revived the interest in stress testing. A quartz cube, placed between polarizing windows, with light from behind, shows the stress in form of color or brightness changes when observed from the front because the stress in the quartz causes additional phase rotation of the light. For testing a transparent sphere, it is placed in a container with a liquid having the same optical refracting index as quartz. The container has two parallel windows consisting of polarizing material (see Figure 4-30). The sphere need not be polished because the liquid makes contact with the quartz surface and lets the contour diminish if the liquid is colorless. Stresses can easily be observed even when the oil has a light yellow color. Since contours disappear, any shape of quartz can be tested.

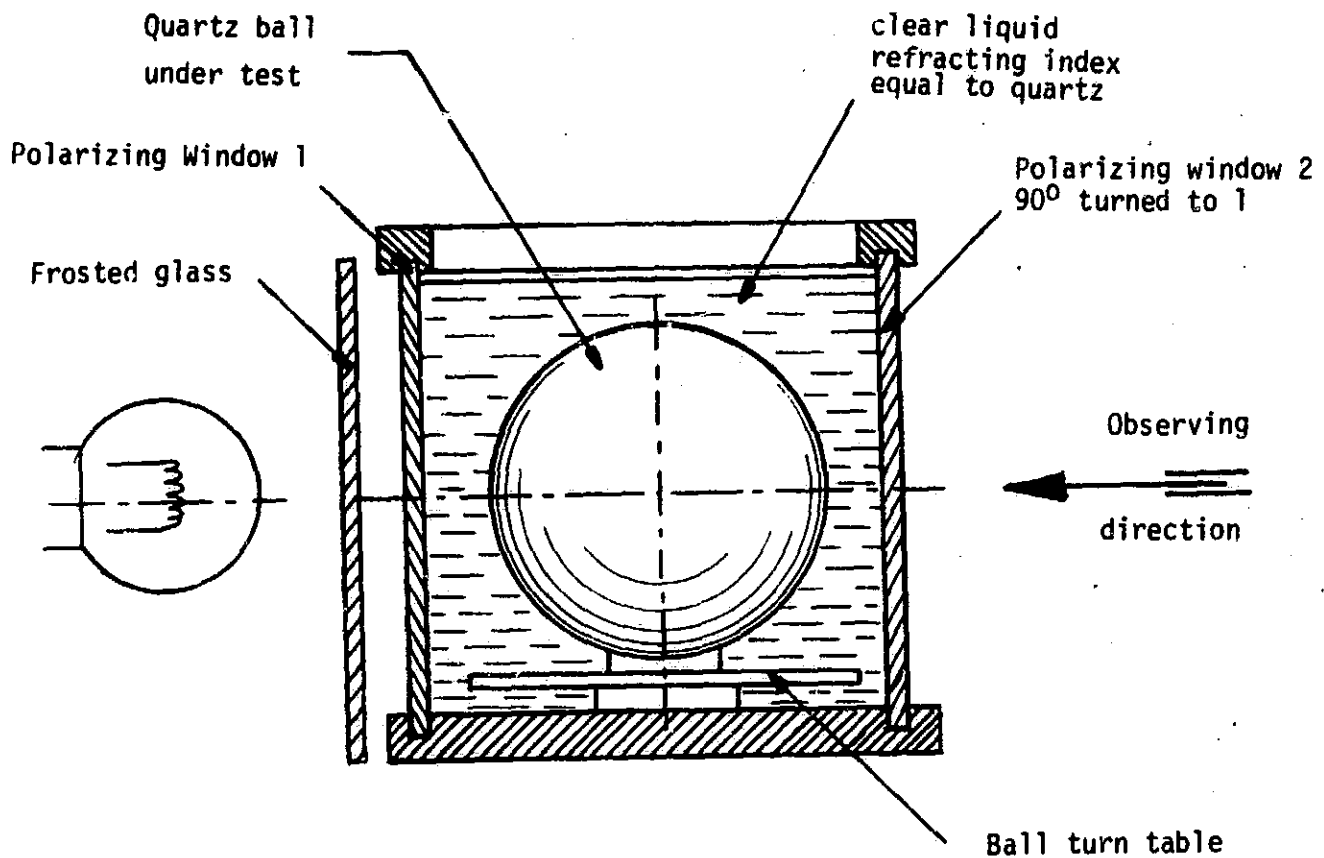


FIGURE 4-30. SETUP FOR STRESS TESTING WITH POLARIZED LIGHT SCHEMATIC

Several balls were tested and showed clearly three zones, indicating stress. One zone was rather sharp and strong in color change, while two other zones were much wider and of lesser color intensity. One of these balls was heat treated and the zones disappeared; it is assumed the stresses have normalized.

All quartz material intended for making spheres or gyro housings must be inspected for stress and, if needed, stress released before and after machining. Amersil warns against stress releasing of their material "Homosil" because it is very sensitive and requires a specific annealing schedule. Amersil proposes one to three minutes of chemical etching with HF to remove surface stresses from machining. The beforementioned stress zones, of course, cannot be removed by surface etching. This material was not from Amersil.

11. Stress Relieving Schedule for Fused Quartz

Before heating, the quartz must be carefully cleaned. Also, the object should be supported in the furnace by non-contaminating material.

- | | | |
|---------|--|----------------|
| Step 1) | Heat to 1150° C at a rate of 45° /10 min | 4 hrs. 10 min. |
| Step 2) | Hold at 1150° C for | 20 min. |
| Step 3) | Drop to 900° C at a rate of 20° /10 min | 2 hrs. 5 min. |
| Step 4) | Drop to 500° C at a rate of 50° /10 min | 1 hr. 20 min. |
| Step 5) | Cut off heat, keep door closed till room temperature is reached or at least 8 hours. Total controlled heat and cool down time about 8 hours. | |

12. Lapping Operation

The rough shape of the quartz ball is produced with a curve generator. This machine has two spindles which can be set to an angle to each other. The tool spindle has at its end a cup wheel impregnated with cutting diamonds. The other spindle is holding the workpiece to be cut. The spindles are rotating in opposite directions; the cup wheel cuts with its inner edge when making convex

spheres, the outer edge generates concave spheres. The resulting curvature is given by

$$\sin \alpha = \frac{\text{cup diameter}}{\text{ball diameter}}$$

In one setting only a partial sphere can be made. For completion, reset the ball into a ball chuck, cut the stem, and finish that side. The cutting rate should be very low especially when approaching the final dimension, leaving about .5 mm stock to be removed by lapping and polishing.

Lapping is performed in the 4 cup tetrahedron lapping machine, using brass cups, aluminum oxide of various grit sizes, and water. The cutting medium is not bonded but loosely rolling between the brass and quartz surfaces. Water is used to carry the grit, to wash away the abraded material and, to some degree, for cooling. Roundness can be achieved very early by keeping the abrasive layer thin (if possible, 1 grit particle size thick) so the cup has maximum efficiency, does not tend to tilt and cause uneven lapping action. The grit should be changed to finer sizes, 600 to 1200, as the stock is reduced from .5 mm to .05 mm.

13. Polishing with Pitch Laps

The pitch must be strained to be free of foreign particles which cause scratches. The pitch should be soft to form well to the sphere and to imbed polishing grit yet should not have excessive cold flow. Cold flow can be reduced by keeping the room temperature at a low level, 16 to 18° C. The lapping cups stand up longer when cool.

The lapping cup is cut free at the inside to about 50% of its diameter. For lapping larger spheres, the lapping cup surface should have criss-crossing

grooves for easier flow of materials. The outside diameter of the cup can be held by a paper cylinder to restrict cold flow; this cylinder is also helpful in casting the cup. The cast cup should be aged for a day or so before using it. In addition of the criss-crossed grooves, the center of the cup should be well vented by a hole to one side. During the finishing operation with cerex-ceriumoxide and water, the abrasive film at the ball surface should be uniform in appearance without streaks or visible markings. Such signs would be caused by uneven polishing action and possible defects. As discussed above, the care for the pitch laps takes much time and the cold flow is a cause for difficulties in lapping. A substitute material was found to eliminate these problems. In the Buehler catalog for mounting and polishing supplies mounting materials are found which can be used to replace pitch. Tests have proven that cups molded from Diallyl Phthalate, blue with mineral filler, does not cold flow and has extremely little wear. Pitch cups have not been used since the new blue cup was tested. The total polishing time of 40 mm ball with a pitch lap should be about 2 to 4 hours. The next problem is to measure the roundness 10 times better than the tetrahedron machine can make it.

14. Lapping Cup Alignment

The lapping cup center line must point at all times to the center of the ball to be lapped. This may be accomplished but not with maintaining uniform lapping pressure under the entire cup. First, there is always a small amount of misalignment which is taken up by elasticity of the cup support drive. Secondly, there is a suction force between the moving ball and the turning cup. Both result in a tendency to tilt the cup against its axis and the uniformity

and symmetry of the lapping pressure are disturbed. This is shown by streaks in the lapping compound at the surface of the ball.

To eliminate the tilt moment of the cup and its ill effects on the roundness of the ball, the cup should have a spherical bearing with its center in the center of the ball. Then, all lapping forces would be tangential and no harm could result. However, this concentric bearing design still needs a drive (cross-sliding coupling) for the cup and it is more costly to produce and cumbersome to maintain. The reduction of suction forces can be obtained by adding criss-crossing grooves into the cup surface. This reduces, unfortunately, the lapping efficiency but also the danger of scratches by foreign particles.

As mentioned above the lapping cups must be properly aligned. Some kind of assurance is given when the distance of all four cups is equal and centered to the drive motor axes. For observing the cup distances a microscope is provided, which has in its eye piece a reticule showing the rims of three cups of equal distance. The microscope has a long working distance so it does not interfere with the polishing process. It is mounted to the base plate of the machine.

15. Polishing Compound Application

Similar to commercial flat lapping machines, our machine has an automatic compound dispenser. It consists of a tank with 3.6 ltr. capacity, and a reduction gear motor driven stirrer. The compound flows by gravity through a control valve to the ball surface. A cam with 4 notches located in the motor control box activates the valve. The timing has been adjusted through testing. To keep the polishing compound from settling and blocking the flow in the valve, we use Everflow in a mixture of:

450 cm³ deionized water

50 cm³ ceriumoxyde

225 cm³ Everflow from

Products Corporation, 518 Milwood Avenue, Pittsburgh, Pennsylvania 15213. Everflow, besides keeping the polishing compound in suspension, acts as a lubricant and reduces the polishing efficiency. We found later that Everflow need not be used. The automatic compound applicator has been in operation since October, 1980, and works very well. It replaces the manual operation which is tiresome and therefore often quite irregular.

16. Dust Protection and Temperature Control

Fine polishing is a very delicate operation and requires dust protection and temperature control. An enclosure consisting of a hardwood frame with plexiglass panels gives the needed dust protection. The machine should be located in a clean room with temperature control to $\pm 1^\circ$ with the cleaning equipment and measuring machines for diameter and roundness included.

17. Measuring Diameter and Roundness

The new lapping control device performs well and predictable. From time and diameter measurements during the lapping process on several balls, the stock removal rates for various lapping compounds are known. Due to the relatively large cup diameters related to the ball diameter, the balls do not show the famous triangular or tetrahedron shapes as it is known to happen in centerless grinders for shafts. The lapping time with various grit sizes can be controlled so that the roundness is accomplished well before the wanted diameter is reached. The diameter is checked with a Pratt & Whitney Mastermike. This machine has an adjustable and repeatable measuring force. Its accuracy is 25×10^{-6} cm. By averaging a number of settings, the accuracy can be doubled and compared to precision gauge blocks of low expansion glass.

For measuring roundness, a Talyrond with a similar absolute accuracy but better sensitivity is used. The Talyrond produces a polar recording with one part of the scale equal to 25×10^{-6} cm. A one fifth of this can be estimated

which is 5×10^{-6} cm (2×10^{-6} inch). Recordings are usually made of three great circles 90° to each other. The roundness requirement for the ball was set to be at least 2.5×10^{-6} cm (1×10^{-6} inch). It is obvious that new measuring equipment is needed with at least ten times higher accuracy. Such a device is under development.

18. Results and Recommendations

The new 4 cup tetrahedron ball-lapping machine using maximum cup size and the 4 cam turn control device for the lapping motors has produced, in a minimum of time, much better ball roundness as compared to previous efforts to make high precision balls with manual control.

The basic knowledge gained or regained during the development and testing of the lapping machine and its controls is listed as follows.

a. Design of the lapping cups and supports

1. The cups should be as large as possible (80% of the ball diameter).
2. The cup support in lateral direction should be by 3 rollers (10% of ball diameter) placed close to the ball surface in the 4 triangular spaces between the cups. Another support for the cups is a flexible cupholder and drive. This design is a compromise.
3. The cups should be well vented and the lapping surface crossgrooved.
4. The cup should have the smallest possible mass to minimize hangdown and tilt forces.
5. The cup should be softly spring-loaded.
6. All cup axes must point at all times to the center of the ball.

b. Rotation, Precession, and Timing

1. The ball must always be in rotation.
2. The ball spin axis must frequently (every 5 to 10 sec) change its position.

3. The spin axis should continuously precess.
4. The spin axis of the ball must never be parallel or nearly parallel to a cup axis other than fast going through this danger zone.

Some of the above points are not new, but have been largely disregarded.

Obedience to these basic ideas provides better and more accurate balls in a much shorter time.

IX. MEASURING OF THE ROTOR DIAMETER

1. Requirements

The diameter range for the gyro rotor is given as 3.809492 ± 0.00038 cm (1.499800 ± 0.000150 inch) so the accuracy requirement is therefore given by 2.5×10^{-6} cm (10×10^{-6} inch).

2. Measuring Equipment

The Standard tool room master mike made by Brown and Sharp has a large range but its accuracy is limited to 10×10^{-6} inch. For achieving reliable measurements the accuracy of the instrument should be one magnitude higher. Therefore, ways and means have been explored to find or develop a more accurate measuring tool. Several instruments are available with the same accuracy as the Brown and Sharp Master mike. Some with very high accuracy are very cumbersome to use by shop personnel. Three other methods have been considered.

(a) Comparing the rotor diameter with a gauge block, by using optical flats and monochromatic light producing fringes. The possible sensitivity is about 10^{-6} in., but the process is delicate.

(b) Comparing rotors of various diameters, by measuring the roundness with the Talyrond and recording the results of all the measured rotors on one polar chart. The difference of diameters can easily be seen, yet the absolute values of the diameters are still unknown.

(c) A more sensitive comparator is being developed which allows a measuring accuracy of 10^{-6} inch and the comparison with gauge blocks. The design of this

new instrument is based upon a precision lead screw with 100 threads per inch and an accurate repetition of the measuring force. A detailed description is presented in the following.

3. Flattening of a Solid Sphere

Elastic deformation takes place where a sphere is in contact with the anvils of a micrometer screw as force is applied. It is customary to use about 100 to 400 gr force depending on the cleanliness of the part. The force used in instruments of highest precision and extreme cleanliness may be as little as 10 gr. The standard equation for calculating the flattening of a sphere is given by

$$f = 2(1.23)(F^2/(RE^2))^{1/3}$$

where F is force Kg, and E is Youngs module which needs correction if more than one material is involved

$$E_{st-q} = (2 E_q E_{st})/(E_q + E_{st})$$

Table 4-13. Material Data

Material	Youngs Mod E	Rotor Mass	g[g/cm ³]
Quartz	0.73×10^6 kg/cm ²	0.0637 kg	2.2
Beryllium	3.00×10^6 kg/cm ²	0.0533 kg	1.85
Steel	2.1×10^6 kg/cm ²	---	7.8

Using the material data given in Table 4-13, the flattening of a 1.5 inch sphere by its own weight sitting on a steel surface is for quartz

$$f_q = 15 \times 10^{-6} \text{ cm } (5.87 \times 10^{-6} \text{ in})$$

and for a beryllium sphere

$$f_b = 6.25 \times 10^{-6} \text{ cm } (2.46 \times 10^{-6} \text{ in})$$

Table 4-14 gives the results of calculating the flattening of a 1.5 inch sphere pinched between two anvils (reduction of diameter of contact areas). The results show that using a measuring force of .1 to .5 Kg, the quartz rotor is actually about 20 to 46 micro inches bigger in diameter than indicated.

Table 4-14. Reduction of Diameter Versus Force

Force (Kg)	Quartz		Beryllium	
	10^{-6} cm	10^{-6} in	10^{-6} cm	10^{-6} in
.100	50	19.7	28.8	11.36
.200	64	25.3	37.1	14.6
.300	84	33.2	48.6	19.15
.400	102	40.8	56.4	22.2
.500	118	46.5	68.1	26.8

4. Longterm Stability of Rotor Shape Under Applied Load

We have calculated the elastic deformation of the rotor under static load and also during rotation. We also investigated the possibility that plastic deformation may take place if an applied load prevails over a long time. A test fixture was built in which the rotor was loaded with a 5 kg weight with the rotor sitting on a flat steel plate. The elastic flattening of the sphere at both contact areas (top and bottom) calculated to be 2.5×10^{-4} cm (10^{-4} inch) and the pressure at the center of the contact area is 4500 Kg/cm^2 (70,000 psi). The radial stress at the center is 3600 Kg/cm^2 (70,000 psi). The compression

strength of quartz is 160,000 psi which is three times higher than the induced load. The rotor was visually inspected and its roundness at the contact areas measured. No permanent flattening was discovered or after a six month load test.

5. Interference Method of Reasoning

The setup for measuring using the interference method is illustrated in Figure 4-31. A monochromatic light source (not shown) of 5876 Å wavelength was used in these tests. The height of the gauge block would be about 100×10^{-6} inch less than the rotor diameter, assuming the gauge block is 2 inches wide. The arrangement results in a wedge above the gauge block extending from 0 to 66.7×10^{-6} inch at 1 inch distance from the ball center to gauge block. For 5876 Å wavelength the distance between fringe maxima represents 2938 Å (11.56×10^{-6} inch). The number of fringes over the 2 inch length is then 5.76 with 0.882 cm (.347 inch) maxima distance.

For improving the readability to one-tenth of a fringe the Fabry Perot etalon is used to change the sinusoidal energy distribution of the fringes to sharp maxima with broad minima (see figure 4-32). For this arrangement the common fluorescent light source was replaced by a laser. With some experience under ideal conditions 1/10 of a fringe can be read, which is 293.8 Å (2.9×10^{-6} cm, 1.16×10^{-6} inch). In practice cleanliness is a major problem and repetitive measurements produce widely scattered results. The method seems to be reliable under clean room conditions, otherwise only to 10×10^{-6} inch at best can be read. The method then gives the same accuracy as the Brown & Sharp master mike. For determination of the true sphere diameter, the elastic deformation (flattening) caused by the measuring force must be considered as has been discussed.

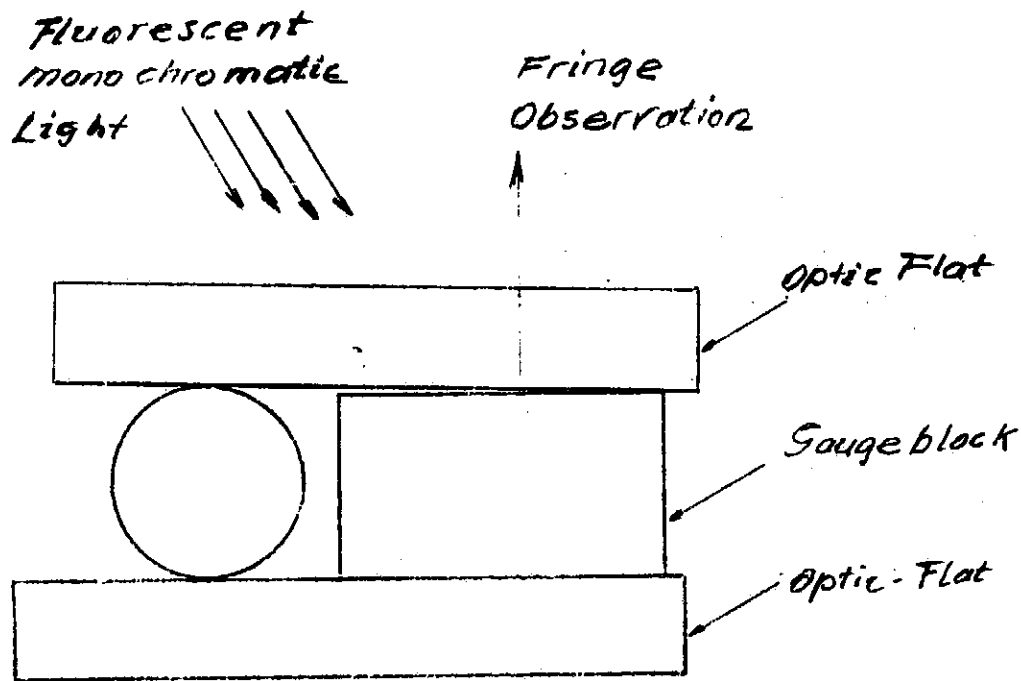


FIGURE 4-31. SINUSOIDAL ENERGY DISTRIBUTION FRINGES

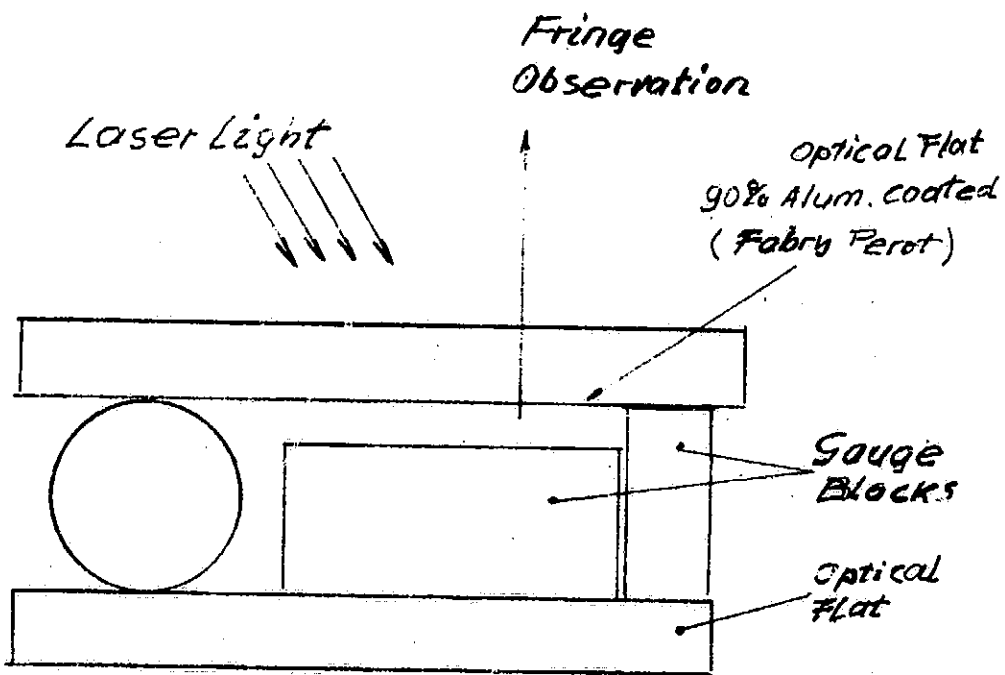


FIGURE 4-32. HIGH CONTRAST FRINGES FOR BETTER RESOLUTION

6. Use of a Comparator to Measure Ball Diameter

Mechanical measurements to extremely high accuracies require compensation for elastic deformation of the object and exact repetition of the measuring force. The new instrument was developed which can measure the force and the value of the diameter of six decimal places. The instrument is built around a leadscrew with 100 threads per inch and a split nut of nylon which is forced to the screw by springs (see figure 4-33). A picture of the instrument is shown in figure 4-34. One turn of the screw represents 0.01 inch 0.025 cm. Attached to the upper screw end is a dial wheel with 12.5 inch diameter divided into 1000 parts. Each part is 1 mm (0.040 in) and represents 25×10^{-6} cm (1 microinch). A microscope with $X = 100$ is used to observe and measure parts of one division. One division of 1 mm magnified 100 times can easily be read with the eye piece micrometer to 1/100 which is equivalent to 0.1 microinch (0.25×10^{-6} cm, 250 Angstroms). The readability of 0.1×10^{-6} inch should be regarded as the sensitivity rather than the accuracy of the system.

The force measurement is accomplished by reading the deflection of a spring which changes the value of a capacitor (see figure 4-35). The spring is machined out of a monolithic block in invar, a nickel-iron alloy with a very low coefficient of thermal expansion $10^{-6}/^{\circ}\text{C}$ at room temperature. By applying force against the part to be measured the invar spring deflects and changes the gap of a capacitor mounted within the string fram. A force of 1 gram deflects the spring 0.1×10^{-6} inch which changes the capacity by 0.0017 pF. The capacity and change of capacity is measured by a general radio bridge, which has a range of 12 digits which is at least 4 digits more than needed. At a measuring force of 200 gr, 1 gr variation means a change in diameter of 0.12×10^{-6} inch, due to the elasticity of the quartz ball. To keep the temperature influence small, the two main posts of the machine are made of invar. The present lead screw was made of stainless steel, however future replacement should be invar. The

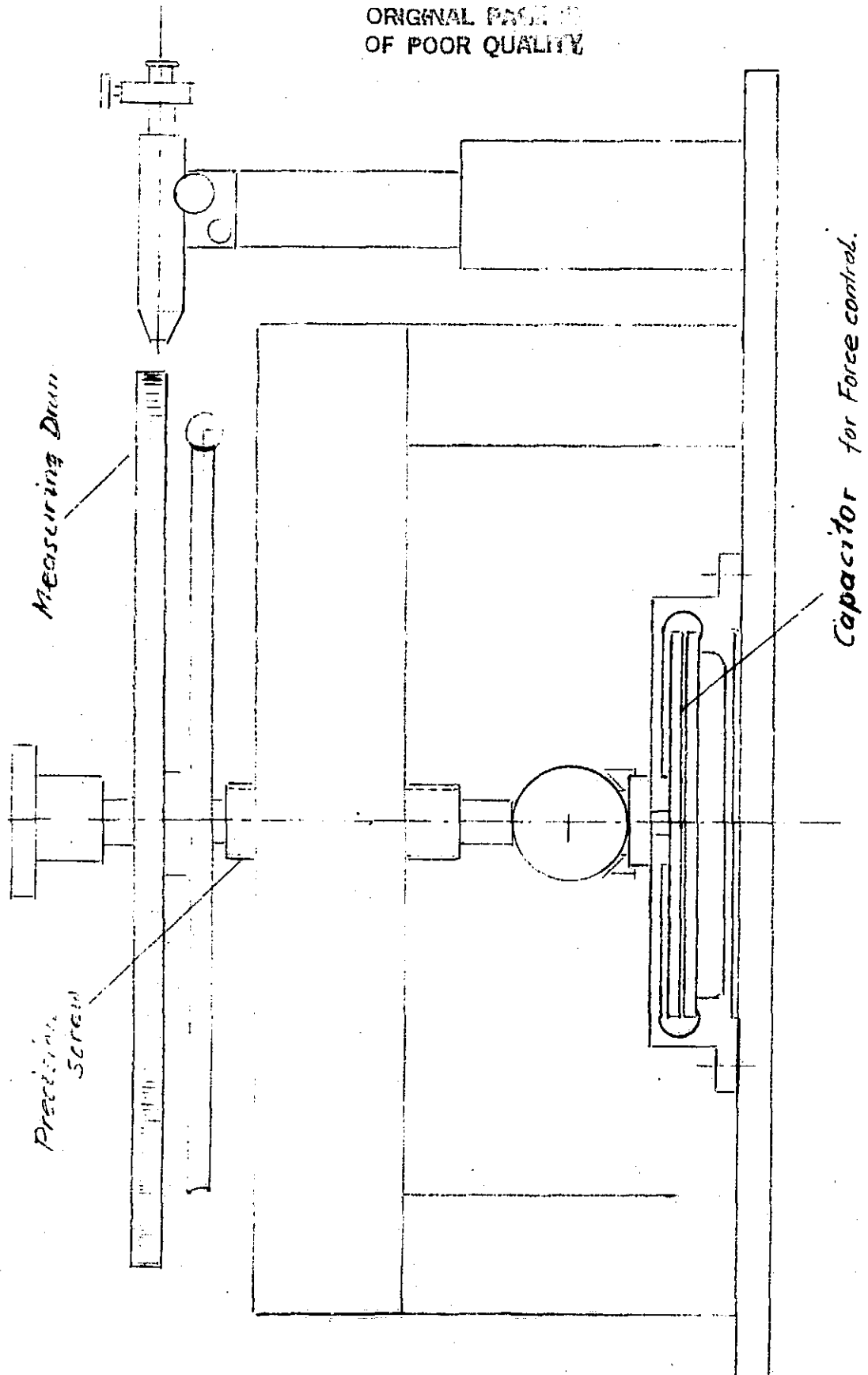


FIGURE 4-33. PRECISION COMPARATOR

ORIGINAL PAGE IS
OF POOR QUALITY

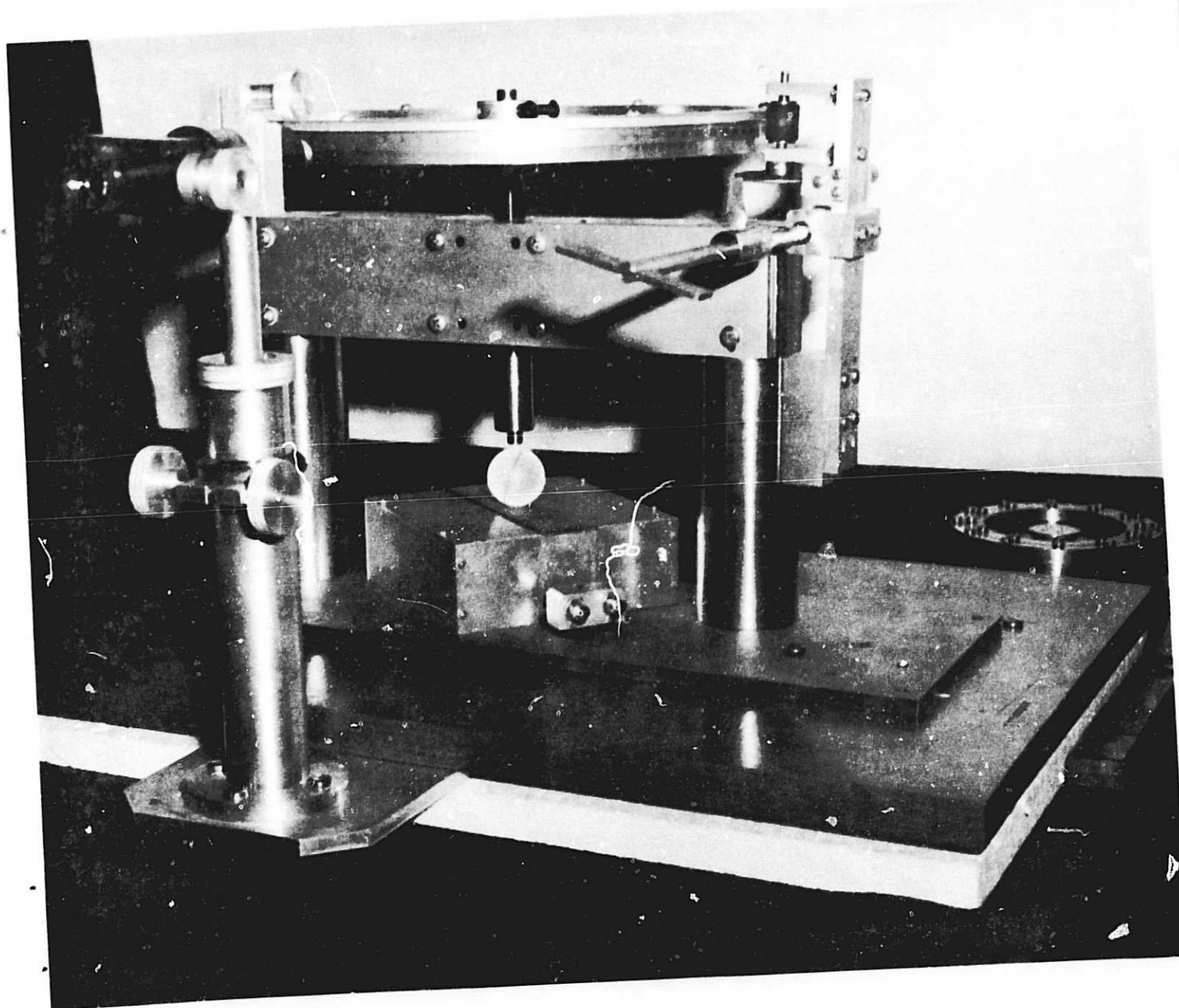
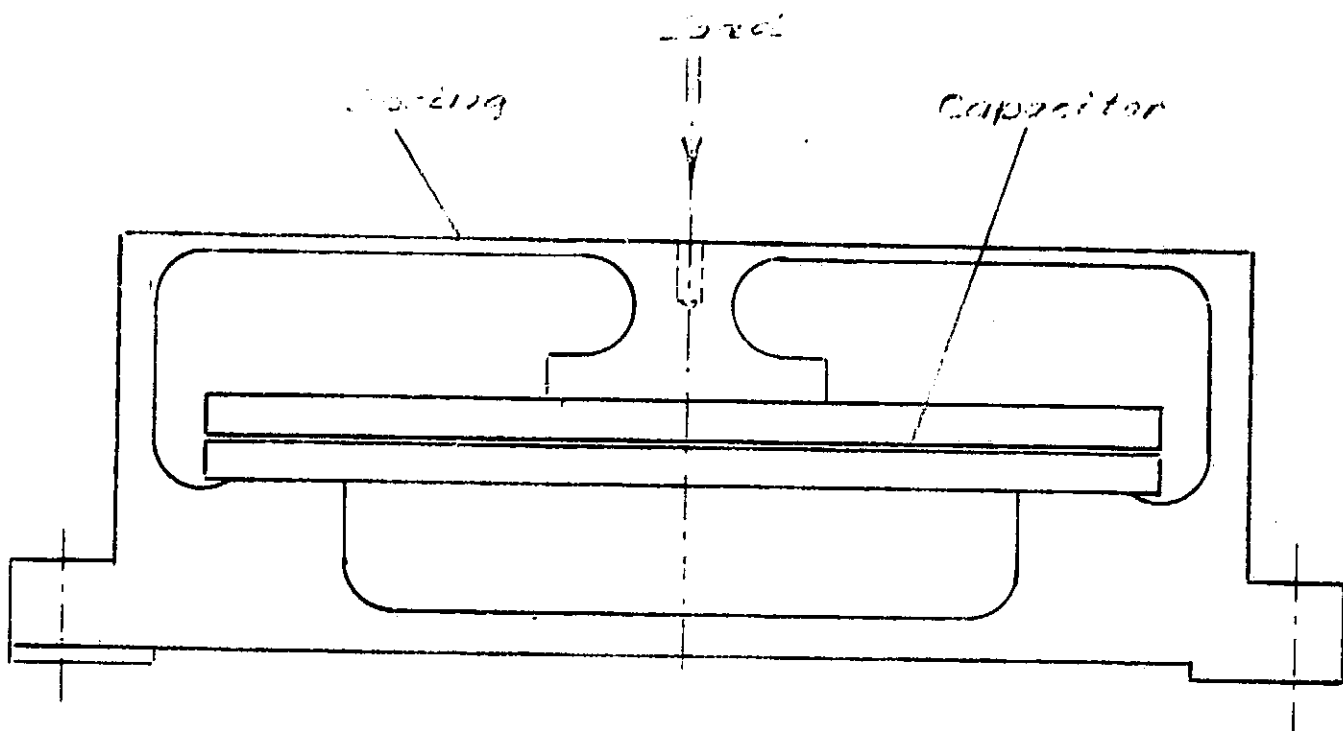


FIGURE 4-34. PHOTO OF ASSEMBLED PRECISION COMPARATOR

ORIGINALLY
DE POOR QUALITY



Force-Control

Monolithic Invar Spring Frame
with 200 pF Capacitor

Spring constant 2.5×10^7 cm/gr 0.1×10^{-6} in/lb/gr

Capacitor Plate size 12.7×12.7 cm 5×5 inch

Dielectric gap 0.0636 cm 0.025 inch

capacity change 0.0017 pF per gr/force

FIGURE 4-35. FORCE CONTROL ASSY FOR COMPARATOR

machine is protected by an enclosure similar to the ball polishing machine. It has a wooden frame and plexiglass panel to protect against draft, sudden temperature changes and dust. Aluminum foil at all sides shields against thermal radiation from the operator. All adjustments needed for the measuring process are made from the outside. The results of the preliminary test measurements show a repeatability of 1×10^{-6} inch.

7. Roundness Measurements of the Rotor

The latest ball polishing machine can produce roundness of better than 25×10^{-6} cm (10×10^{-6} inch), but it has been difficult to measure the roundness to that high accuracy. The major problem is surface contamination caused by improper cleaning. There is very often an electrostatic charge at the ball which attracts small non-metallic particles. Whenever the sensor arm of the roundness measuring machine hits such a particle, the machine records a spike and may not return to the surface because the particle is wedged between sensor and ball. The particle may stay until it wears out or falls out, therefore falsifying the roundness measurement of the ball. The computer of the roundness measuring machine integrates the readings, including the spikes and misreadings caused by logged-in particles. The foreign particles adhering to the surface are up to 2.5×10^{-6} cm (10×10^{-6} in) in size. The ball should be inspected under a microscope and found to be clean just before measuring.

The roundness machine used in this work is the Talyrond Nova. The Talyrond 73 made by Rank Taylor Hobson England consists of the basic machine, a desk with the electronic units, the display module, a polar recorder, and, for ultra high precision, a desk with the Taly Nova computer and Teletype machine. To achieve highest accuracy the spindle errors can be separated from the measuring results by the computer. The electronics allow extremely high amplifications. We have used polar chart radial magnification up to 100,000 in which 0.1 inch on the

chart represents 10^{-6} inch. The printout of the Teletype on request can give very detailed information on the average and maximum deviation from roundness. The machine does not, however, disregard spikes and dirt, and thus careful examination and interpretation of the polar chart is needed. The Talyrond Nova is the most advanced machine available. A typical polar chart is shown in Figure 4-36.

The roundness should be measured and recorded about the three major axes. A ball turning device was therefore developed to place the ball in any desired angular position on the measuring machine table, without marking the ball surface (see Figure 4-37). The quartz ball is supported by three 15 mm steel balls spaced at 120° and fixed to a steel base which can be rotated about its vertical axis to any desired position. The ball turner has two soft rubber wheels to take the ball, lift it off the base, rotate it, set it gently down on the base, and then release it. The ball rotation angle can be controlled to about 1° . The ball turner is adjusted to meet the ball in its centered position and can be moved by keyway to make room for the rotating Talyrond sensor. A photograph of the ball turner attached to the Talyrond machine is shown in Figure 4-38.

X. THE ROTOR COATING EFFORT

1. Task Summary:

A nearly perfect sphere of fused silica of 38.1 mm diameter is to be coated with a uniform thickness of niobium. The quality of the coating is to be such that the metal will become a superconductor at helium temperatures. The diameter of the ball may vary from ball to ball as much as 5 microns. The coating must well adhere to the ball. The uniformity in thickness must be within 5×10^{-6} m (0.2×10^{-6} inch). The uniformity is so as to avoid vibration of the spinning rotor. Selection and testing of the ball material grinding and finishing including machines and equipment has been discussed earlier in

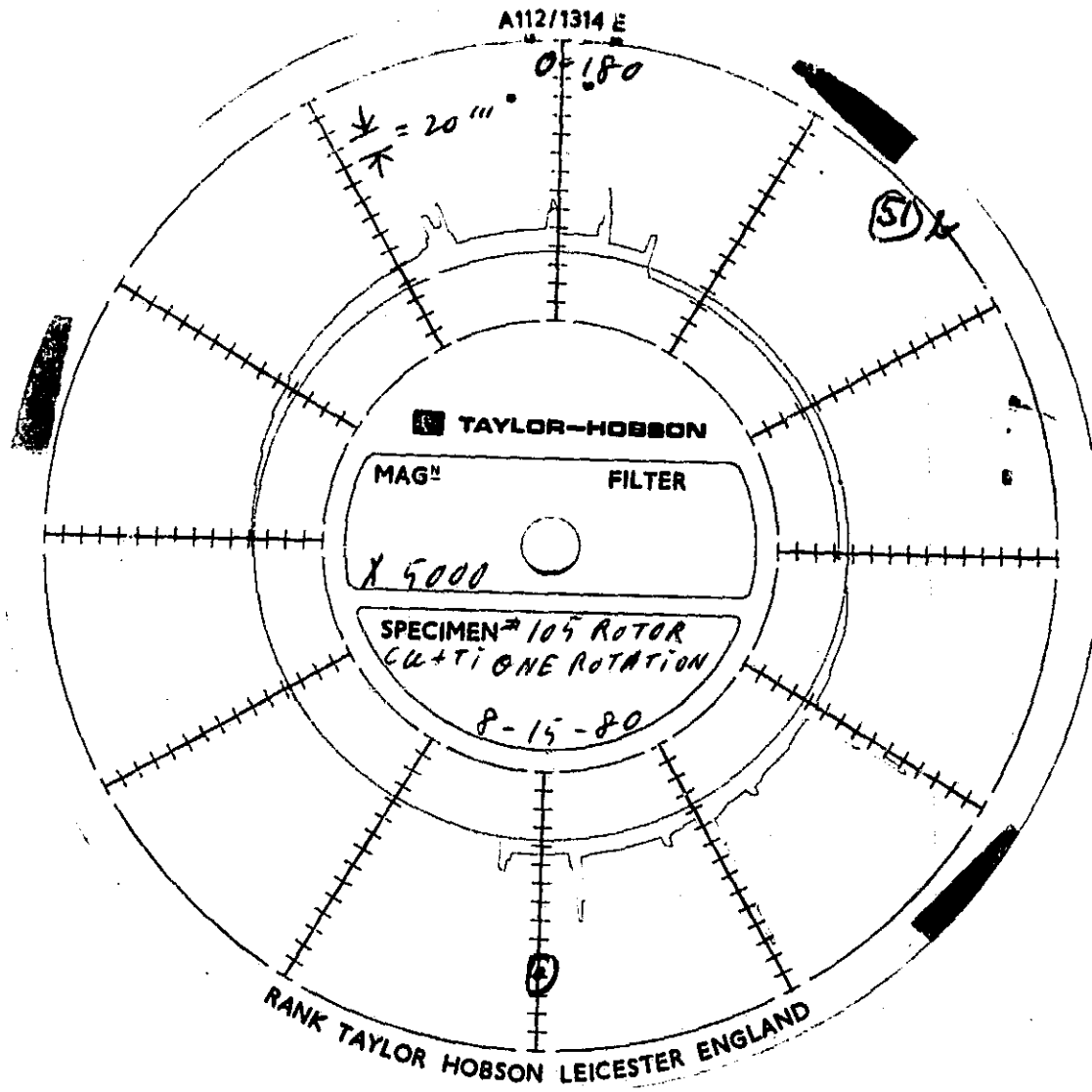


FIGURE 4-36. TYPICAL POLAR CHART

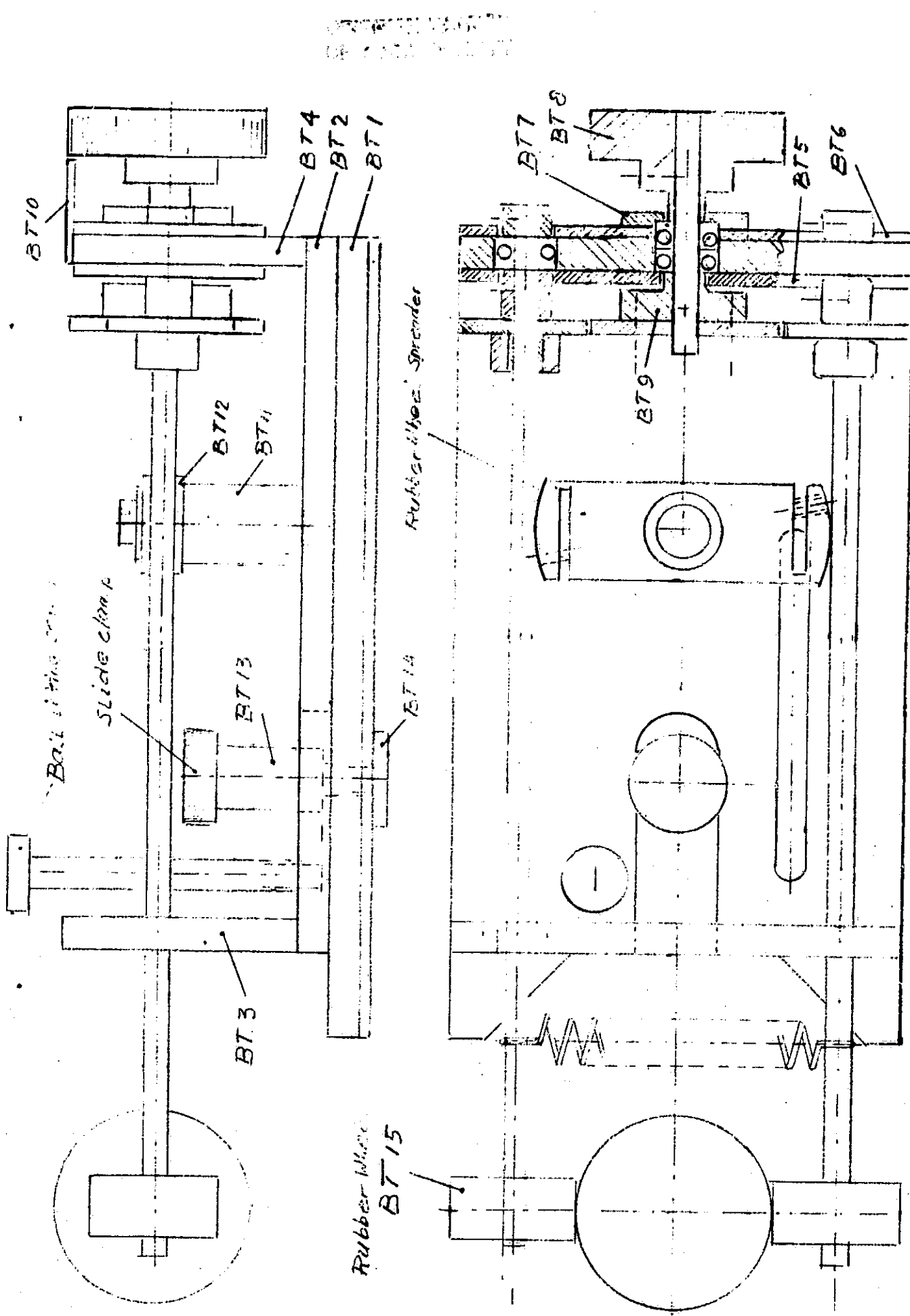


FIGURE 4-37. BALL TURNER ASSY

ORIGINAL PAGE IS
OF POOR QUALITY

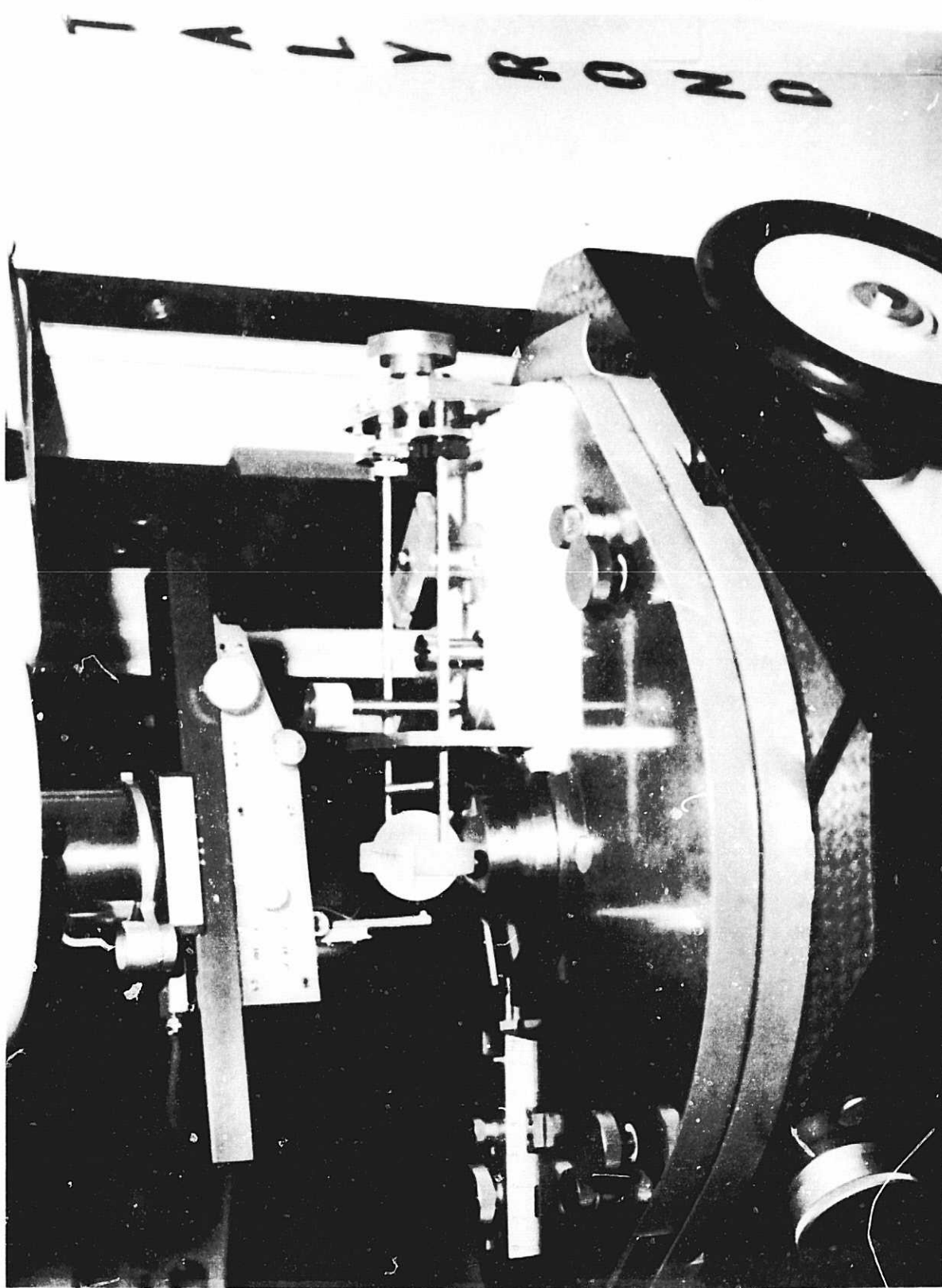


FIGURE 4-38. PHOTO OF BALL TURNER ATTACHED TO TALYVONAL MACHINE

this report. The following chapter deals with the rotor metal coatings, the equipment for coating and testing for uniformity.

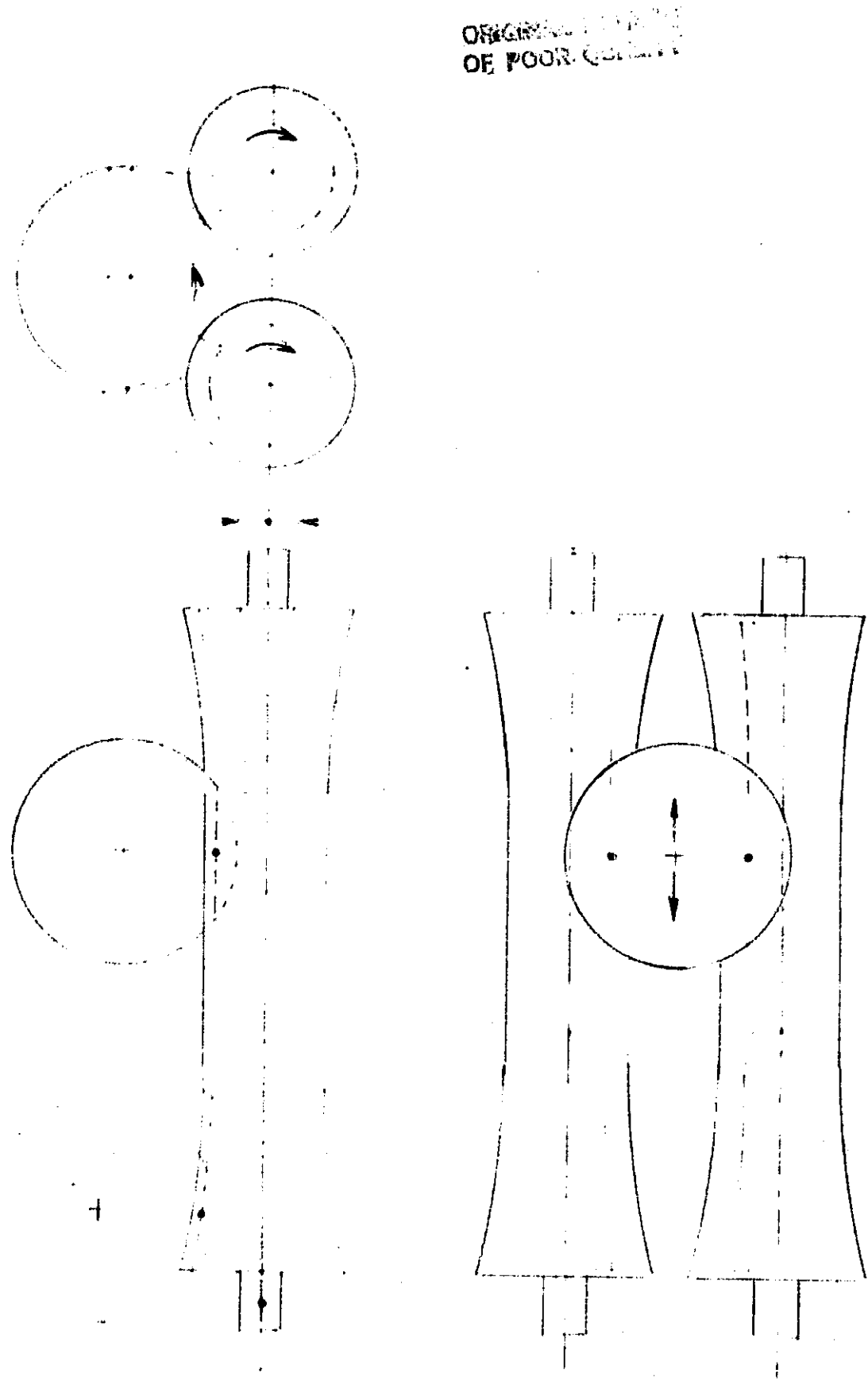
The coating process is typically a three step procedure in which a first coating of 100 Å of titanium is applied for adhesion. A second coating of 15000 Å of copper is then applied provide good electrical conductivity for testing at 1 g and room temperature. A final coating is 100 Å of niobium which will become super-conductive at helium temperatures. The following pages describe mainly the various efforts in rotating the ball for achieving uniform coatings.

2. Metal Deposition Processes

Various conventional means of metal deposition were considered which could potentially fill the requirements stated above. Electroless plating was tried but did not result in good bond. Vapor deposition needed a mechanism to support and rotate the ball. Electrogalvanic coating needs a conductive precoat. The only process which produced good bonding was found to be sputtering of titanium to a heated rotor. This bonding layer can be very thin, 50 to 100 Å, and need not be extremely uniform in thickness due to its thinness. The titanium layer may vary as much as 10%. The sputtering technique also requires that the ball be rotated in order to achieve a uniform coating. A number of rotating techniques were investigated and there are described in the following sections.

3. Ball Coating on Tilting Turning Tapered Rollers

Figure 4-39 shows the tapered roller concept for rotating the ball. A pair of rollers carrying the ball to be coated are slowly rotating and oscillating a few degrees. Both rollers rotate in the same direction which causes the ball also to rotate. As the rollers tilt, the ball is rolling down hill and changes its spin axis. Before the ball reaches the down hill end of the rollers the tilt angle of the rollers is reversed. The tumbling motion of the ball comes to a stop and begins tumbling in the other direction down hill again. These roll



ORIGIN
OF POOR COATING

FIGURE 4-39. A PAIR OF CYLINDER SYMMETRICALLY TAPERED ROTATING & TILTING FOR COATING SPHERES

and tilt motions are to be continued till the desired coating thickness is reached.

The roller distance should be as close as possible to keep the contact force between ball and roller small. The length of the rollers should be at least 4 times the roller diameter, the tilt angle and frequency established by testing. The hoped for uniformity in coating to be achieved in this concept is based on the tumbling motion of the ball, the uneven ratio of roller length to ball circumference and the large number of turns and tilts. The disadvantage of this roller system is contact effect of rollers and the ball.

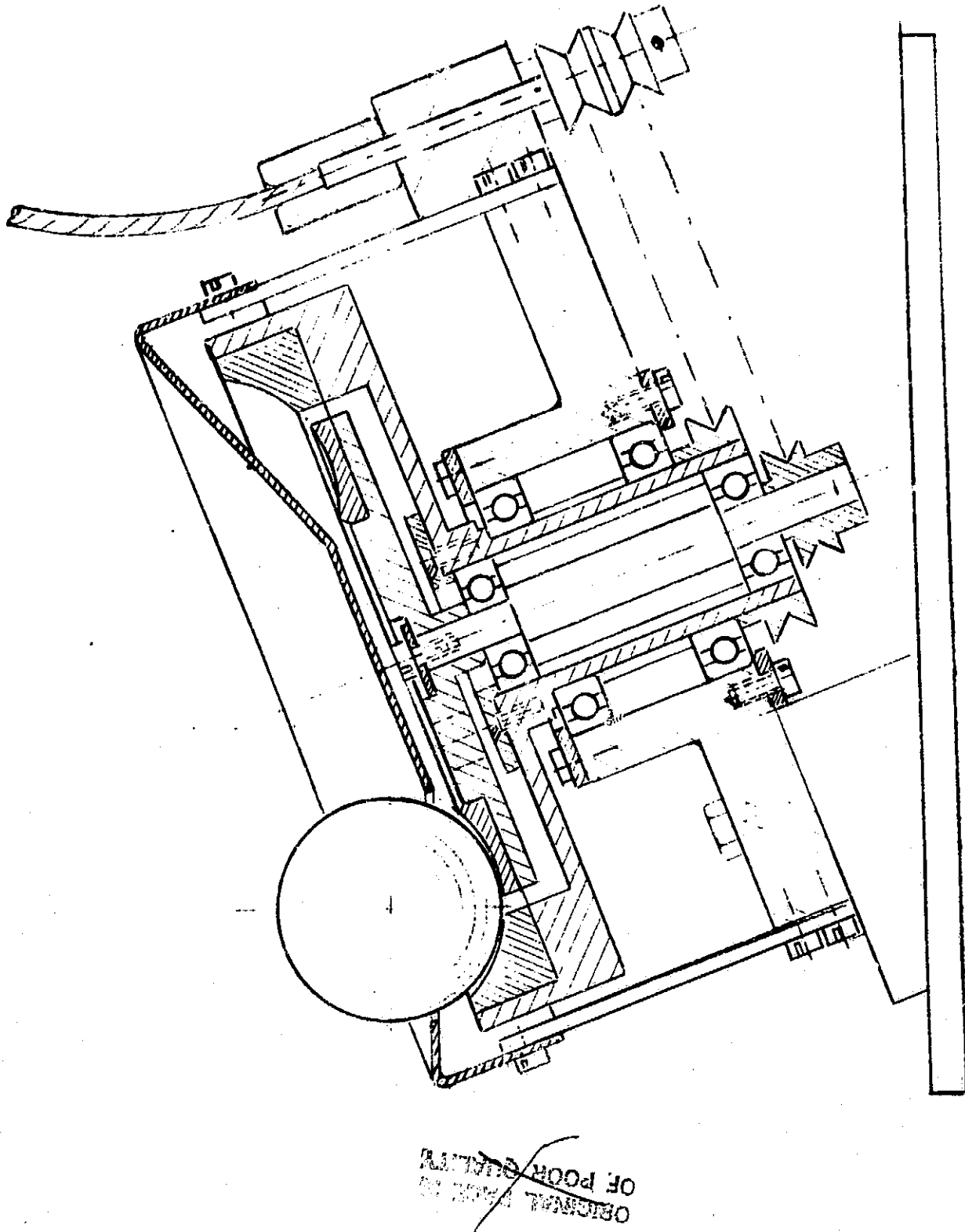
4. Ball Coating on Two Concentric Rings

The concentric rings concept is shown in figure 4-40. The ball is supported by two toroid like concentric rings, with one rotating with slightly different speed, in equal direction. This turns the ball about its vertical axis. The rings are tilted to keep the ball from moving in a circle away from under the sputtering target, and to roll this ball about its horizontal axis.

The toroidal rings have a radius slightly larger than the radius of the ball to be carried which increases the contact area and decreases the pressure substantially as compared to the pressure typical to the parallel rollers. Another advantage is the simplicity of the drives. Both rings are driven by two ball chains from one shaft. The shaft extension is a flexible cable connection to a vacuum feed through. The drive-motor with all its contamination potentials is out of the vacuum chamber.

A shield is provided to protect the curved rings from sputtering. The ball moves a small amount within the kidney shaped shield opening. The use of Teflon TFE or Kapton-Polyimid as material for the curved rings, instead of hard metal, would reduce the specific pressure considerably. One problem is the possible contamination by the plastic materials the typical pressure and temperatures for

UNARMED POSITION
OF POOR QUALITY



OF POOR QUALITY
UNARMED

FIGURE 4-40. CONCENTRIC RING CONCEPT

sputtering is 10^{-3} mm Hg and up 200°C. The disadvantages of this system is as before the mechanical contact of ball and toroidal rings. No tests have been made however.

5. Gas Bearing For Ball Support, Spinning and Precession

It is very desirable to support the ball during the coating process without touching it so as to avoid spots, scratches or other imperfections caused by mechanical supports. The gas bearing offers this advantage and also provides rotation possibilities. Inert argon gas was chosen. The gas can be used during sputtering to float and spin the ball and also cause the spin axis to precess. The gas bearing system must be able to control the ball motion so that every ball surface element has equal time under the target and receives equal coating thickness with high degree of uniformity. The gas bearings suspension, spin, and precession orifices are timed by an automatic control device to provide the desired ball motions. The system and control program was tentatively established and first tested in a standard environment with success. Tests were then run in 10^{-3} torque vacuum in a specially built chamber with a plate glass lid for better observation of the ball movements. These test were required since the sputtering chamber will obscure the visibility beyond the minimum observation requirement. The automatic gas bearing control must therefore work with high reliability. Several gas bearings were developed and tested based on many years of gyro air bearing design experience.

Figure 4-41 shows a typical gas bearing design. A set of five (5) orifices are at the floor of the cavity with .006 inch diameter to float the ball. A set of eight (8) tangential orifices .012 in diameter are to spin the ball and to precess its spin axis. Once the spin axis is established it cannot be changed with respect to the ball. A set of three (3) leveling screws are provided to keep the ball from rolling downhill with a horizontal spin. The leveling screws also make the eight (8) tangential spin-precession orifices more uniform in

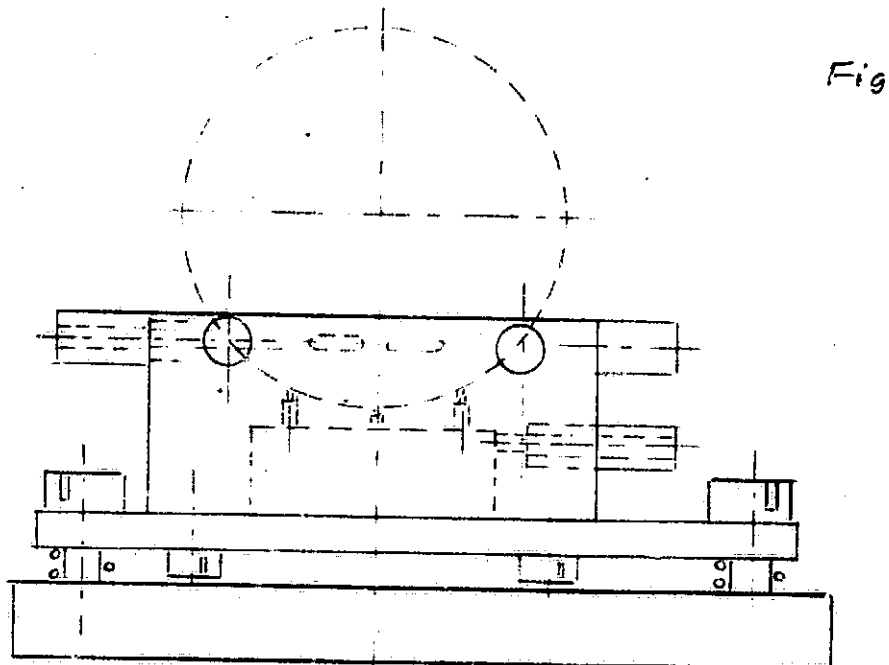
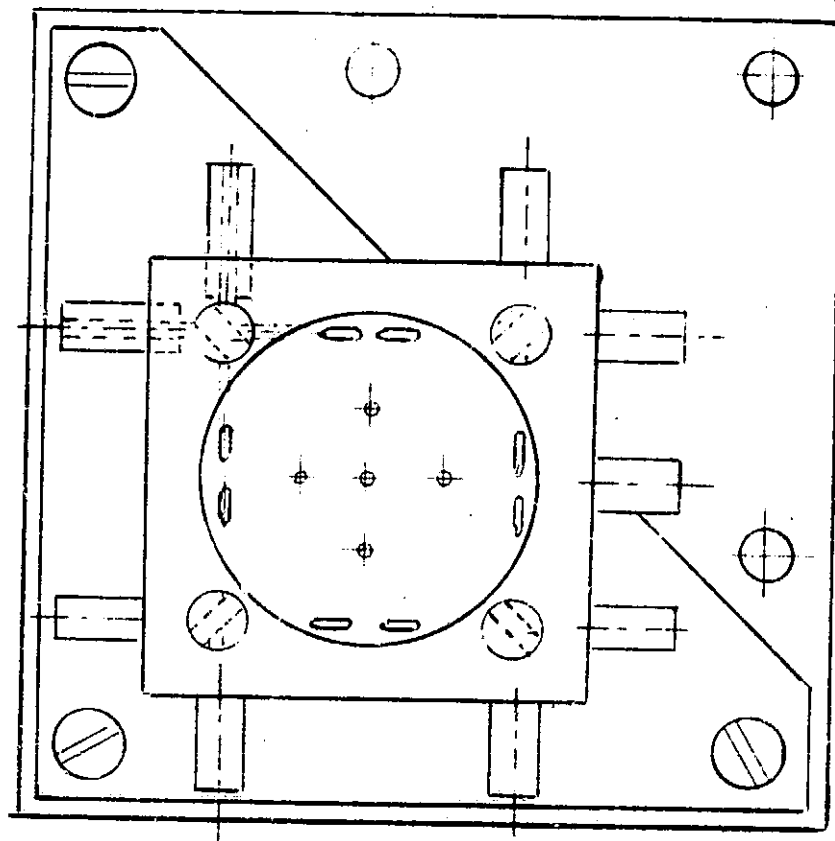


FIGURE 4-41. SPHERICAL GAS BEARING FOR 1.500" BALL WITH SUPPORT - SPIN - & PRECISION ORIFICES

performance. Uniform coating of the ball with a gas bearing seems to be theoretically possible, if the following conditions are fulfilled (a) target and shade ring configuration provide linear or symmetrical deposition. (b) Rotational and precession speeds are controllable, constant and measurable. We have not been able to measure the precession speed, therefore, the efforts to coat using the precession as a means for achieving uniformity was given up. A new start will be made by spinning without precession. Meanwhile, other possibilities will be evaluated.

6. Three Point Support for Ball Coating

Since the gas bearing for controlled ball rotation could not be developed to the desired performance in the available time, efforts were concentrated on a mechanical support by three points with periodic resettings to achieve sufficient uniformity of coating thickness. The ball is simply placed on top of three metal pins, which have small teflon tips to prevent maring of the ball. The three pins are pointing square to the ball surface, 120° spaced and touch the ball at 45° south. For pin dimensions and arrangement, see Figure 4-42. The lower half of the ball gets very little coating during sputtering and the areas where the teflon pins carry the ball are very small and do not receive any coating during sputtering. To compensate for the nonuniform coating two or more coats are applied with different ball position settings. It is expected that several coats are needed to accomplish sufficient coating uniformity and to minimize the lack of coating at the support points. For example, the first coat could be performed with the north pole of the ball up and the second with the south pole up. Such a procedure requires only that metal be deposited symmetrically with respect to the equator. The distribution can be triangular, trapezoidal, rectangular, sinusoidal, and any other form as long as symmetry to the equator is maintained. By selecting the proper sputtering target form and shading such symmetry can be achieved. The final arrangement is pictured in

ORIGINAL PAGE IS
OF POOR QUALITY.

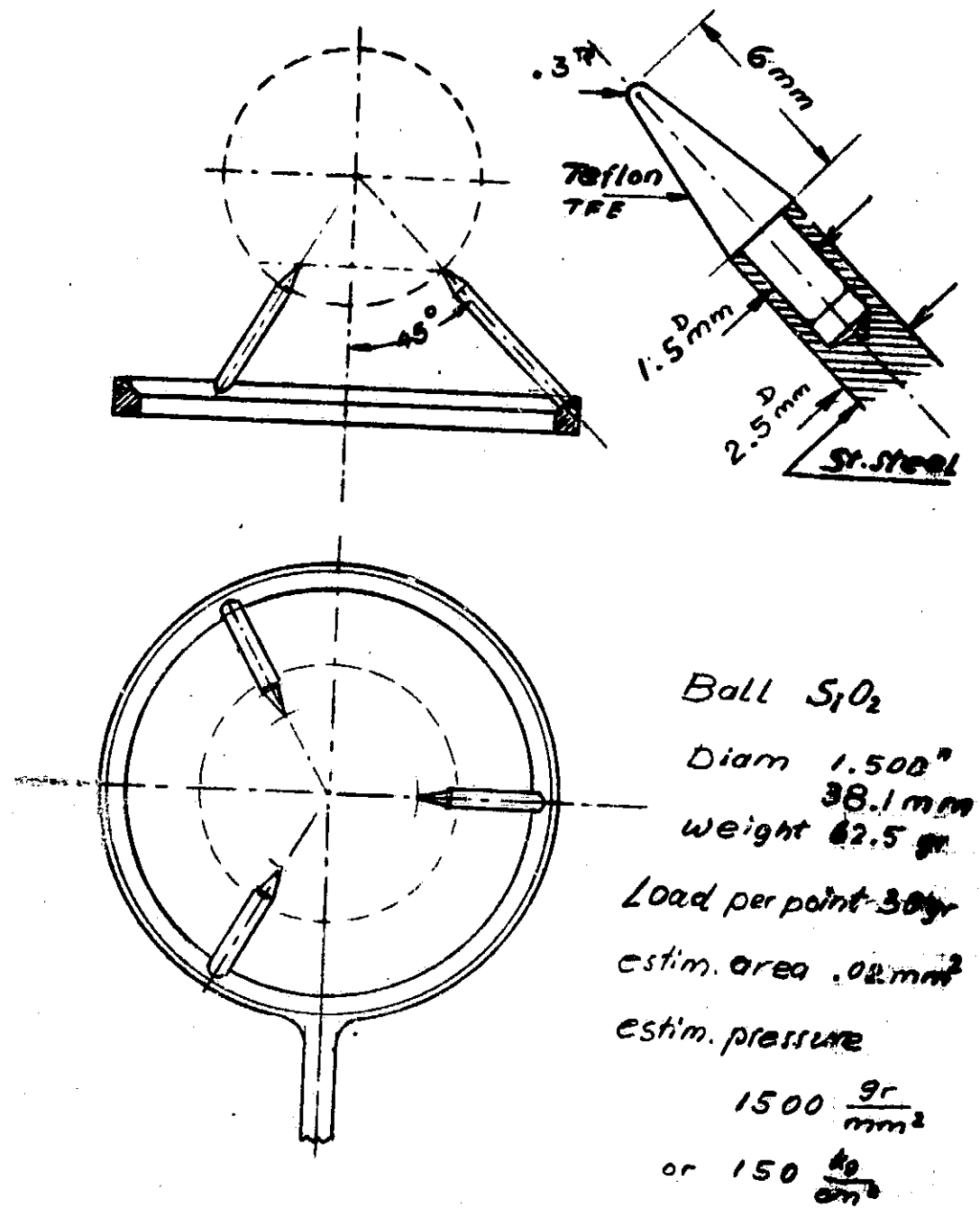


FIGURE 4-42. BALL SUPPORT BY THREE POINTS

Figure 4-43. The effort then concentrated on the problem of how to change the ball position during the sputtering process.

7. Ball-Walker For Coating

The three point support and special target with shade ring performed well, except that the vacuum had to be broken each time that resetting of the ball was needed. Breaking the vacuum results in oxidation and is therefore not acceptable. The ball-walker system was conceived to move the ball in 28 steps each around the three orthogonal axes (see figure 4-44). The ball is supported by three teflon tipped arms fastened to a ring on a horizontal beam, which lifts, turns, and sets down the ball to a second three point support with a vertical axis (see Figure 4-45).

To achieve sufficient uniformity in metal coating thickness, the ball should be rotated as that all surface elements have equal exposure to the sputtered metal particles. An acceptable solution is the rotation of the ball about the x, y, and z axis in the succession according to the following program.

(a) The ball will rotate 360° about a horizontal axis by walking 28 full steps. One full step is accomplished by rotating the actuator shaft from stop to stop and return. These first 28 steps have rotated the ball about the x-axis or in the plane of the zero - 180° meridian.

(b) Rotate the inner ball support with the ball 90° clockwise, and again proceed to make the 28 steps with the same selected exposure time for each step as before. The ball will rotate about the y-axis in the plane of the 90° - 270° meridian.

(c) Stop deposition briefly, make seven steps and then turn the base support with the ball counterclockwise 90°. Then continue deposition during the last 28 steps. The ball will rotate about its polar (z)-axis. This completes the three axis rotation and coating.

ORIGINAL DRAWING
OF POOR QUALITY

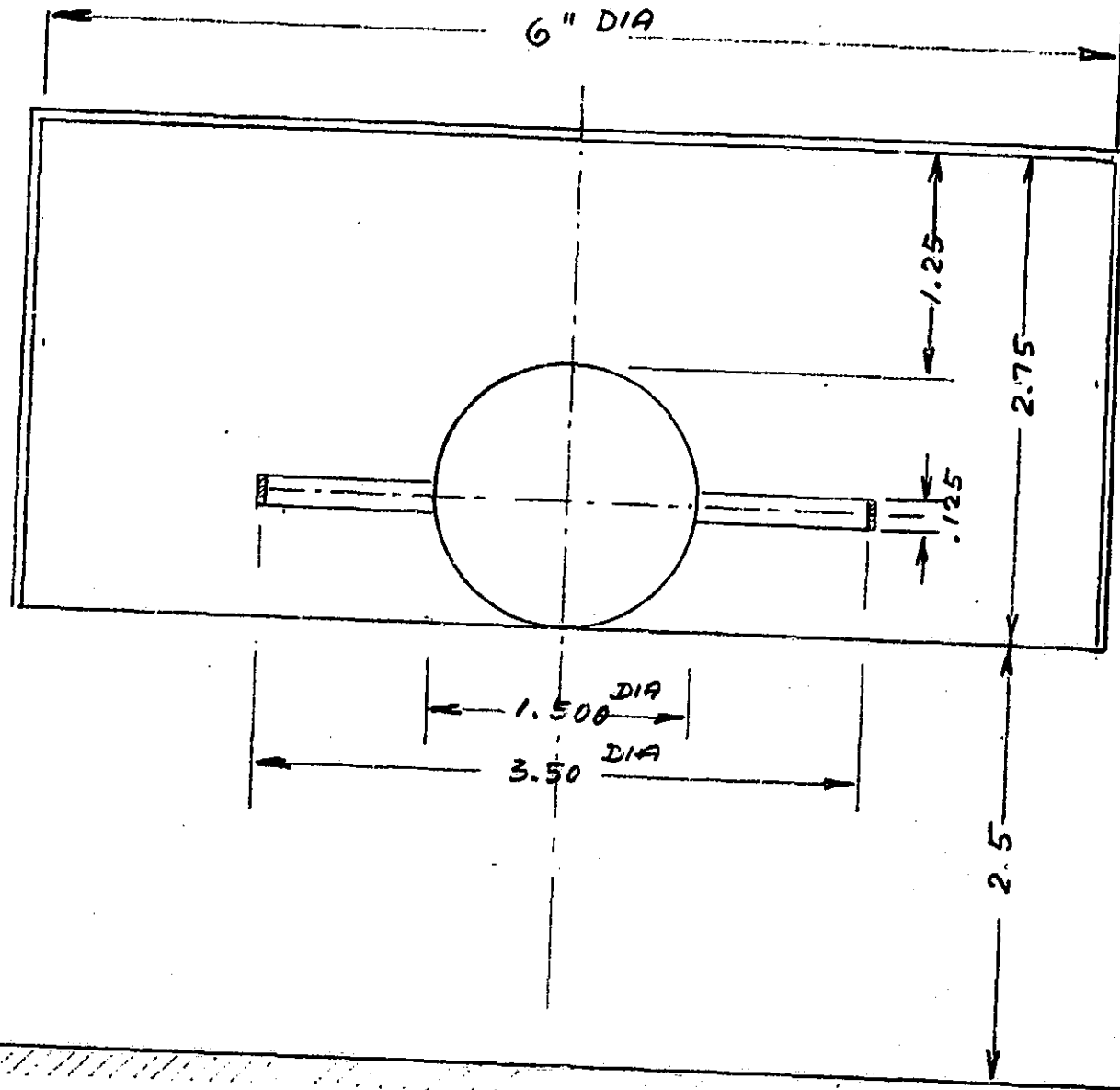


FIGURE 4-43. SPUTTERING TARGET AND SHADE RING

ORIGINAL PAGE IS
OF POOR QUALITY.

Target

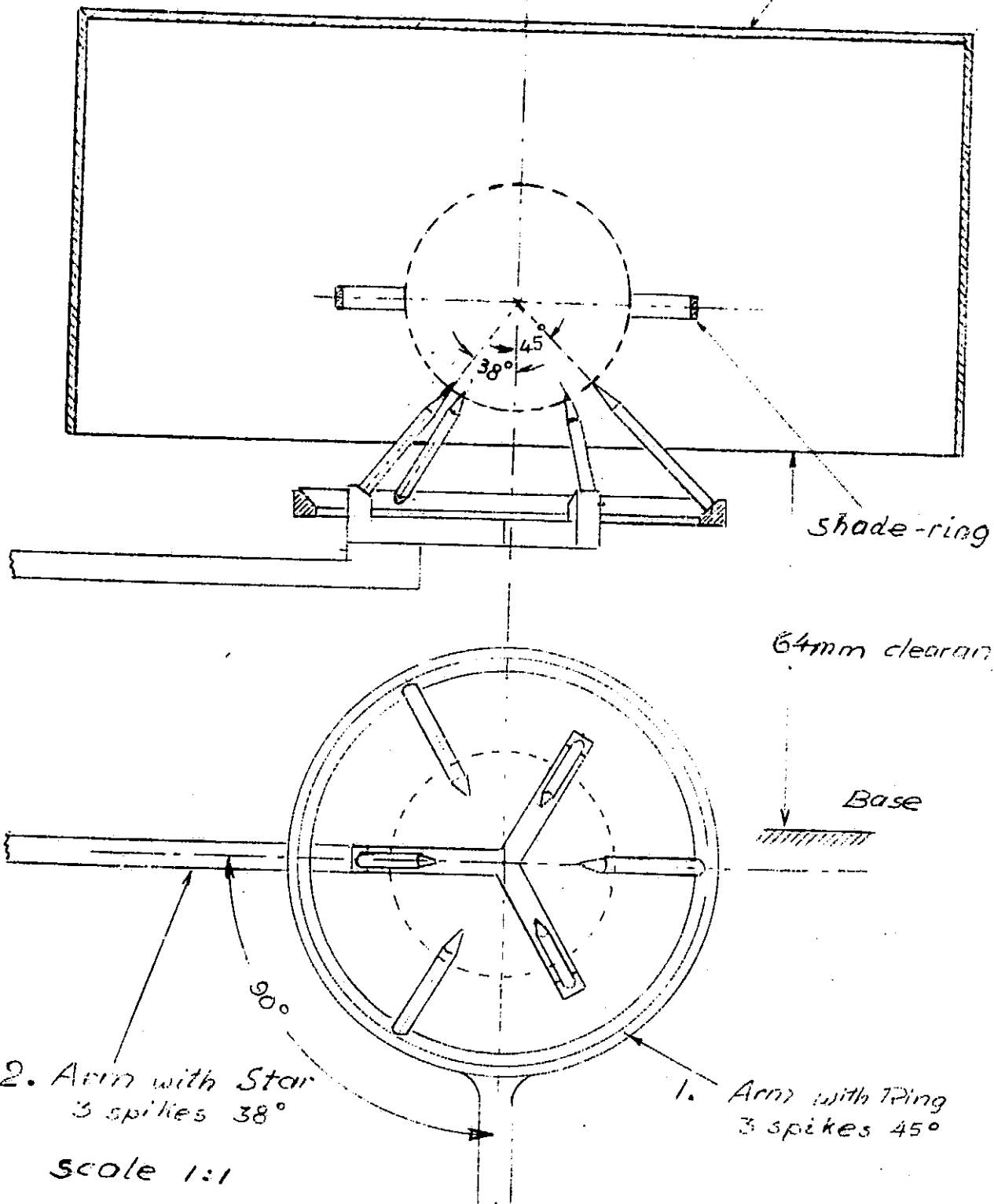


FIGURE 4-44. TWO ARM BALL SUPPORT FOR STEP BY STEP BALL ROTATION

ORIGINAL PAGE IS
OF POOR QUALITY.

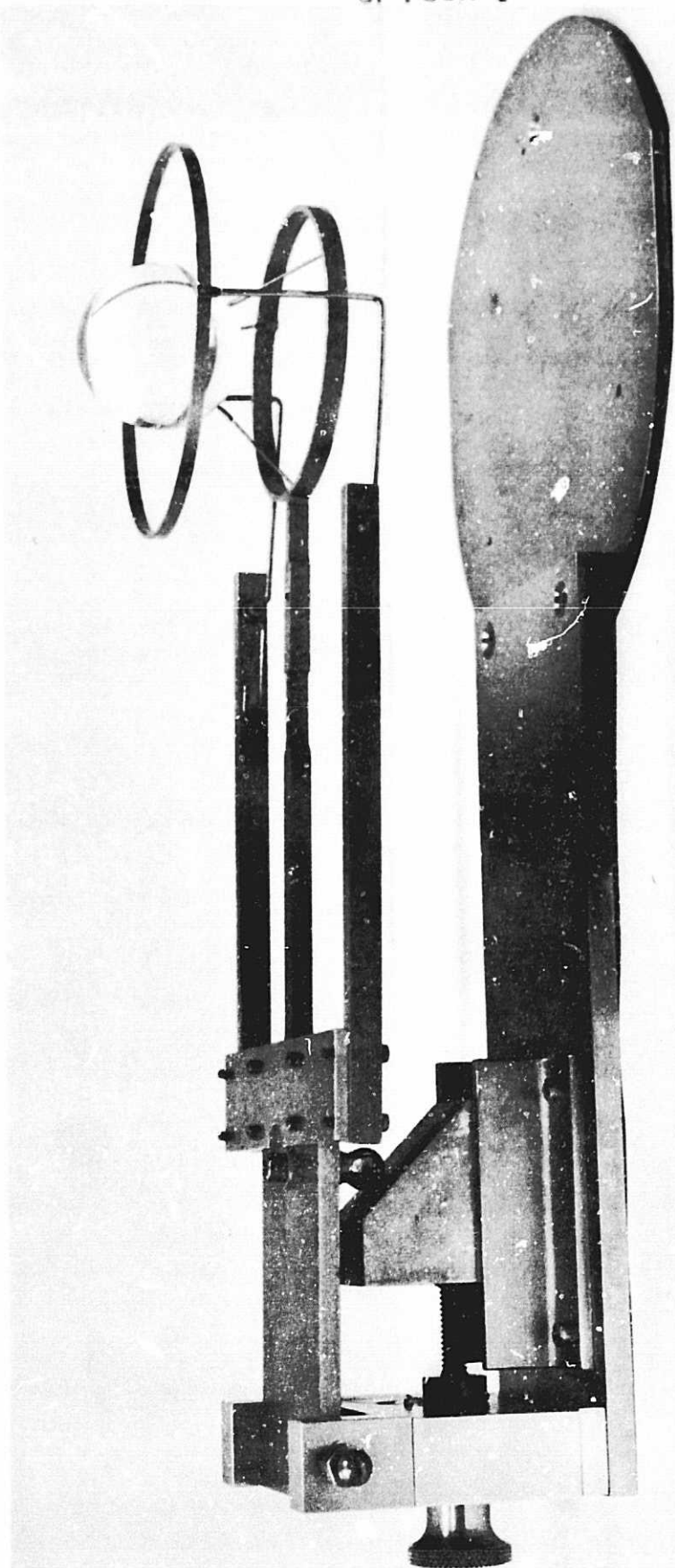


FIGURE 4-45. THE BALL WALKER FOR BALL COATING

The adjustment of the two sets of three support points was cumbersome and was never successfully performed. Because of this, the ball always made a rocking motion when lifted and set down. The three point support was therefore changed to a two ring system shown in Figures 4-46 and 4-47. One ring attached to the horizontal arm for lifting, turning and setting down to the second smaller ring below. Also, the high voltage insulation (teflon tips) has been eliminated, and the metal rings are grounded to eliminate sparking. The two rings are made of stainless steel, their contact surfaces have the ball curvature and are highly polished for large contact area with the ball (see Figure 4-48).

The coating uniformity was not good as expected when the stepping (walking) was done manually. The major causes of the nonuniformity were traced to accumulation of stepping errors and operator fatigue. The complete walking process is as follows

A new ball walker is being designed for motor drive and automatic timing. The $3 \times 3 \times 28 = 252$ steps will be done automatically. Two changes to another great circle still need to be done by hand. The timer will actuate the motor to make one step every minute. After 28 steps are completed an alarm will sound for the operator to turn the base 90° . Again after 28 steps of two minutes each the alarm will sound for another 90° circle change, by hand. After the third 28 steps of one minute each, the coating will be completed.

8. Measuring the Metal Coating Thickness

The requirements for the titanium and copper coatings are

<u>Material</u>	<u>Thickness Range</u>	<u>Accuracy</u>
Titanium	2 to 5 microns	± 0.2 microns
Copper	20 to 40 microns	± 0.2 microns

spotting target

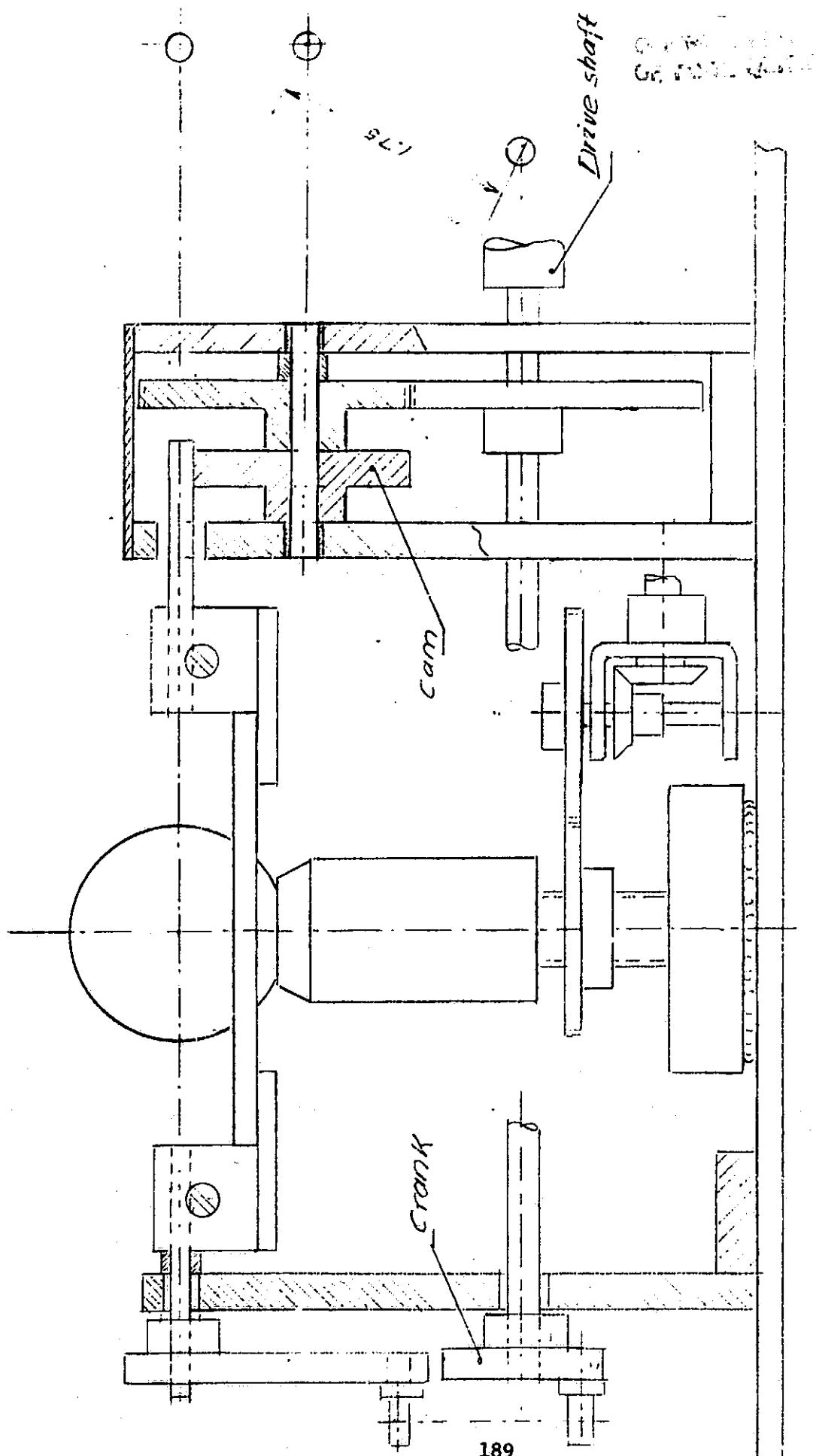


FIGURE 4-16. BALL WALKER II

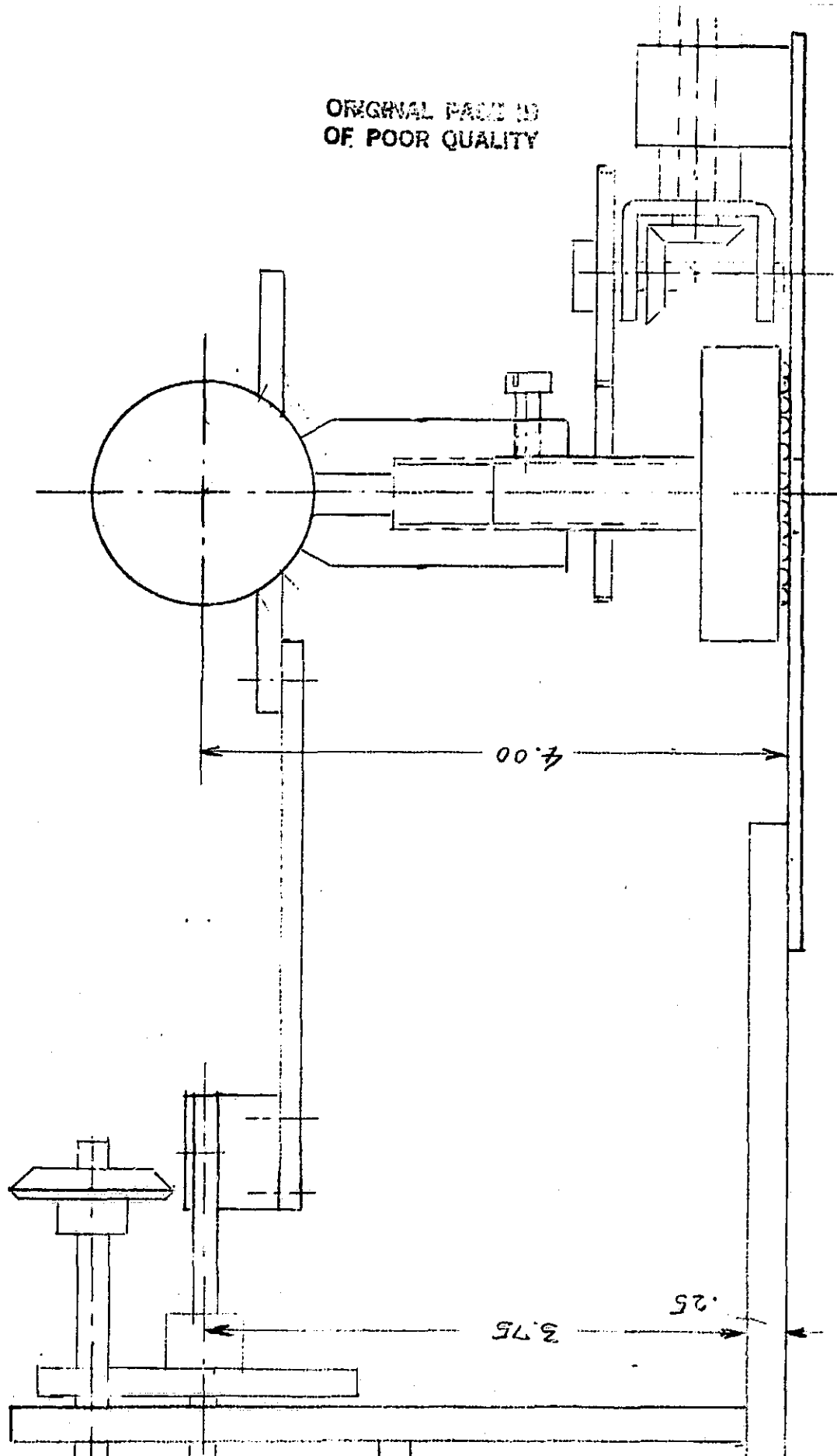


FIGURE 4-47. BALL SUPPORT ASSY FOR BALLWALKER
NOTE INSULATED

ORIGINAL PAGE IS
OF POOR QUALITY

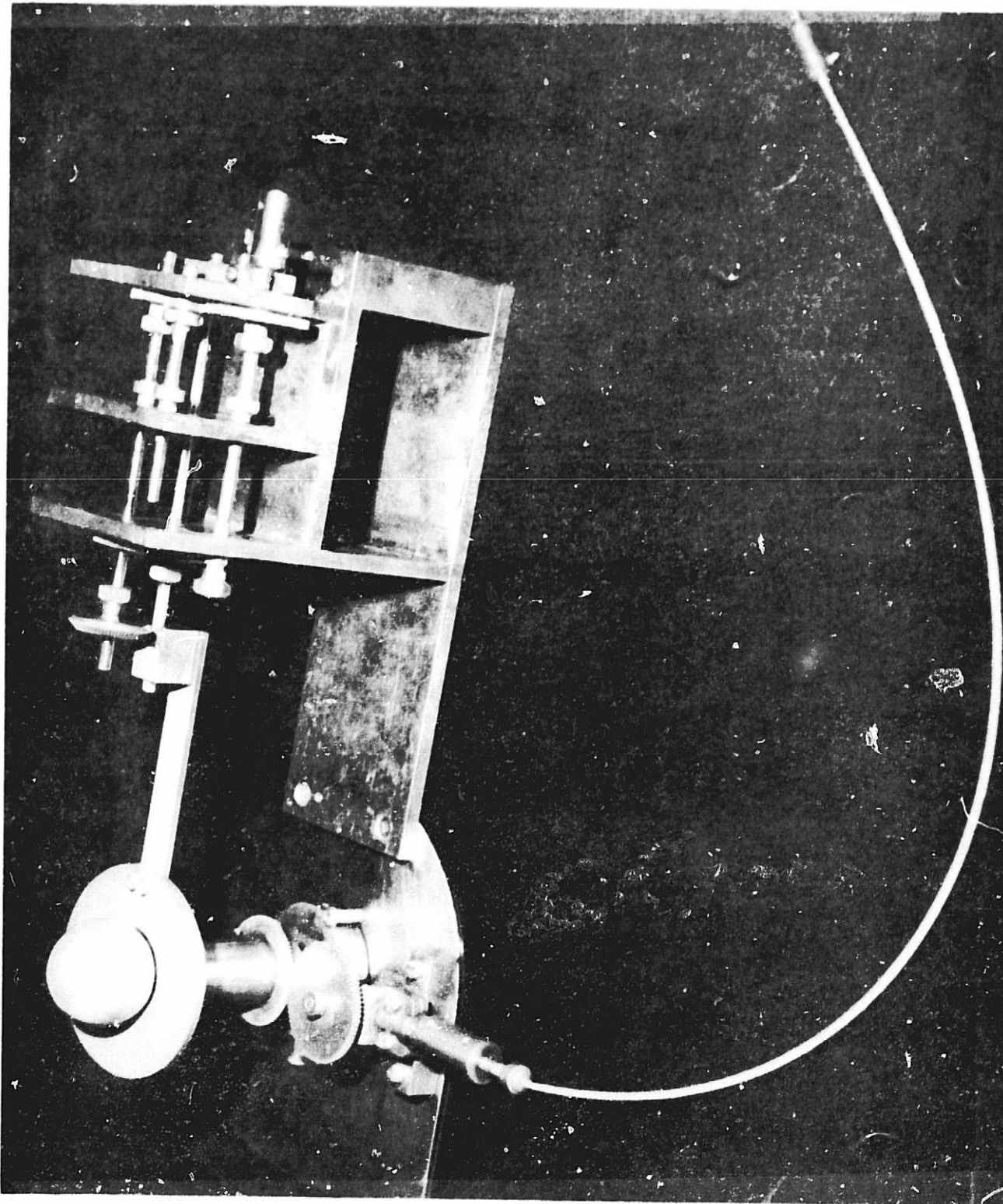


FIGURE 4-48. ASSEMBLED TWO RING BALLWALKER

The measurement of these thicknesses has been investigated using a number of methods. The weight measurement method is the easiest to perform. A rough determination of the average coating thickness can be made by weighing the ball before and after coating. The coating thickness is given by the equation

$$\text{Coating thickness} = \frac{\text{weight of coating}}{(\text{surface area})(\text{density})}$$

For copper 1 g. weight difference represents 0.001 inch and for Titanium 1 g. represents 0.002 in. The weight method yields only the average thickness of the film. The weight method gains importance when the process of coating guarantees uniformity to 2%.

The beta-ray backscatter method is based on the principle that part of a high energy (beta-ray) beam striking a sample is backscattered and detected by a Geiger Mueller tube. The instrument can be calibrated with thin films of known materials and thickness. It is useful for nondestructive measurements. A report was written by L. C. Clune: Nondestructive Techniques for Measuring the Thickness of Thin Niobium Films, and by Laverne Clune and Thomas D. Barber, entitled: Beta-ray Back Scatter Measurements of the Thickness Profiles of Thin Metal Films on Quartz Sphere Gyroscope Rotors.

A very simple and reliable method is to chemically etch a hole into the metal film and measure the step from the substrate to the top of the metal film. This can be done with a Schmalz microscope, a surface tester, or a standard electric measuring pickup. We made an exposure template which is wrapped around the ball, coated with a photoresist (see figure 4-49). The template has 36 holes, 1/16" diameter and 0.131 inch between centers. After exposure to the sun

C-3

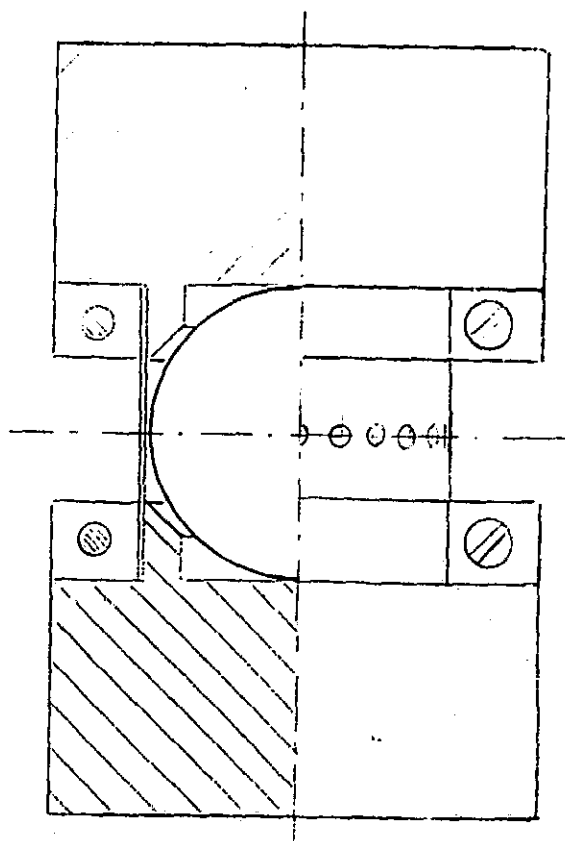


FIGURE 4-49. FIXTURE FOR EXPOSURE OF HOLES ON ROTOR

the resist at the hole location is dissolved and the copper etched. After etching, the rest of the photoresist is removed. Three series of holes marking 3 orthogonal circles are etched. The ball is then ready for coating measurements. This destructive system is used to establish the process for sputtering a uniform coating. Figure 4-50 shows the result of one such test.

The etching of the metal coatings requires some care. Copper can easily be dissolved by Ferric chloride. Most difficult to remove chemically, however are titanium and niobium. Hydrofluoric acid is a constituent of most of the etchants for these metals. Since hydrofluoric acid is also a very efficient etchant for fused silica, it is difficult to use. The removal of the titanium and niobium coatings from the rotor can more easily be done by polishing with ceriumoxyd, which is used in the standard polishing process of the rotor. If the diameter of the ball does not permit any further polishing then place the ball in 50% solution of hydrochloric acid and boil for several hours until the metal is removed.

XI. GYRO ASSEMBLY AND TEST MOUNTING

1. Assembly Procedures

The gyrohousing halves are oriented to each other by three quartz dowel pins and held together by three metal screws and nuts. The accuracies of the dowel pin locations and their fits are most important. The two cavities must be placed in angular and lateral position as accurately as the location of the electrodes which is dictated by the drive channel seal gaps of $.000125 \pm .000025$ inch (3 ± 1 micron). Each housing half must have the dowel pin holes and the screw holes drilled when the housing is still in its original fixturing (holder) for final machining in order to produce the location accuracy required. The halves are joined and held loosely in place by three screws. Next in each of the three pinholes an expansion tool is inserted and expanded to align the two

ORIGINAL PAGE IS
OF POOR QUALITY

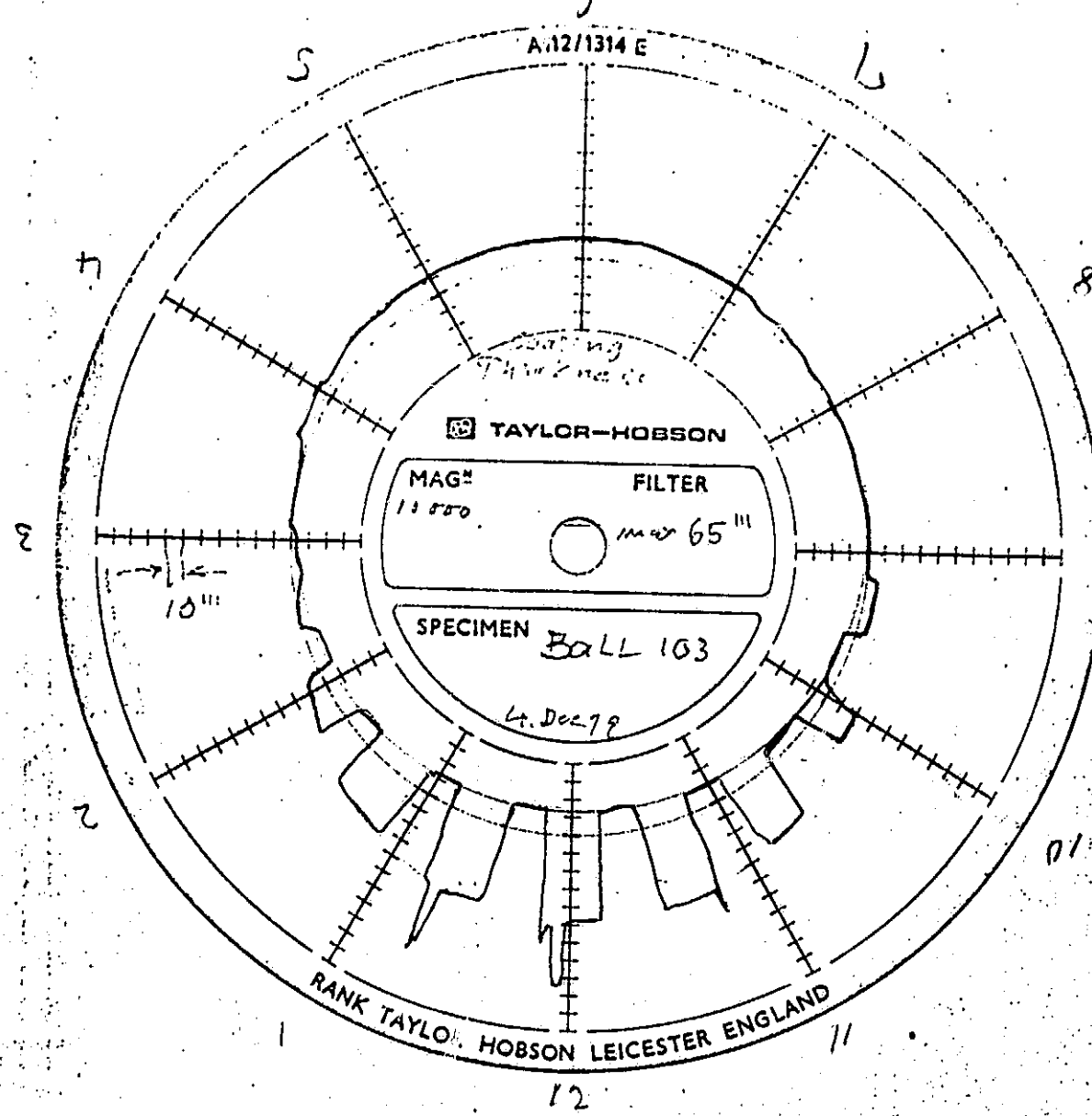


FIGURE 4-50. RESULT OF COATING THICKNESS TEST

halves. Then the three screws are tightened to keep the halves in place. The process of dowel pin fitting can now begin.

Before the assembly begins, the three screw holes and the three dowel pinholes must be lightly chambered on both ends to avoid chipping during the fitting and assembly operations. The dowel pins are .75 inch long, .187 inch in diameter, and tapered 3°. A special diamond impregnated tapered homing tool, cross-slitted for elasticity, is used to fit the holes for the dowels. The dowels and holes are numbered and individually fitted, therefore, not interchangeable. The markings of hole and dowel pins are always at the larger side to eliminate the gussing of which end goes where. The dowel insertion is done with a special tool to apply controlled force via calibrated spring and screw. The same tool must be used for the removal of the pins punch and hammer are not allowed. Figure 4-51 shows the dowel insertion tool before final assembly can start, all parts must be carefully cleaned, measured, and the results properly documented. Immediately before assembly all measured parts must be cleaned again. Cleaning and assembly should be done in the highest class clean room.

2. Gyro-Mount for Testing

The purpose of the mount is to hold the gyro firmly in place and provide all necessary connections; e.g., high voltage for suspension, helium gas for spin up, vacuum-suction at gas exits, fiberglass cable for speed measurement. For testing the gyro in vacuum at very low temperatures, the material selection is of great importance. Most materials shrink and some plastics also harden when exposed to low temperatures. The gyro mounting must not apply undue forces to the gyro housing, because of the danger of distortion or even breaking. Therefore, the design has to allow for the metal shrinkage without exerting dangerous forces to the gyro. The basic principle employed in the design is the "three point contact" which does not torque the gyro housing. All gas connec-

OPTIONAL POSITION
OF DOWEL PIN

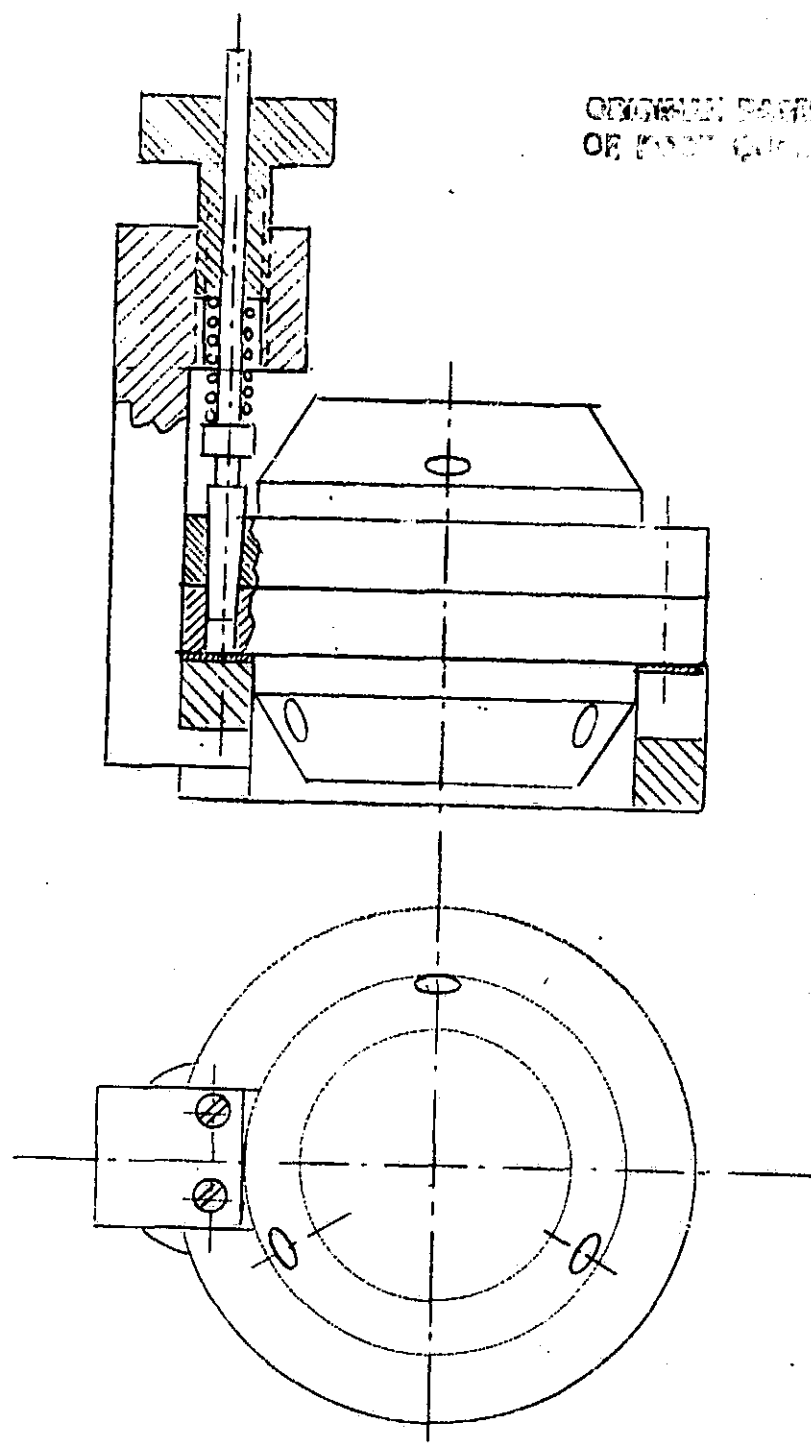


FIGURE 4-51. DOWEL PIN INSERTION TOOL

tions have "O" ring seals and all screws are holding via metal helical springs to avoid high local stresses. The mount as shown in Figure 4-52 is for horizontal rotor spin axis in which the three suspension electrodes carry equal loads. An extra base was made to be added to the mount for spinning the gyro at 54°, 44°, 32° to the vertical. In this position one electrode axis alone carries the rotor weight. The other two electrode axes are horizontal.

3. Auxiliary Gas Bearing for Rotor Levitation

A gas bearing has been proposed to carry the rotor weight for testing the gyro at 1 g., which would eliminate the need for high voltage in the levitation system. The high voltage has caused arcing which causes defects in the rotor coating. We considered two options: (a) a gas bearing for the vertical axis only or (b) a gas bearing in all three axes. To reduce the amount of gas flowing into the cavity - rotor gap, the gas bearing should be used only for a vertical electrode axis. If the gyro is mounted for testing with a horizontal or vertical spin axis, all three electrode axes have equal load which means all three axes need gas bearings.

A design of a gas bearing is shown in figure 4-53. The electrodes are recessed and form just the right type of gas bearing pad. A redesign of the contact screw for the gas supply is all that is required. A gas flow restriction to reduce or eliminate the rotor vibration is at the end of the bore next to the entrance to the gas pad.

Gas bearing data:

Rotor weight 63g. or 0.14 lb.

Pad diameter 0.75 inch, Area 0.44 sq. in.,

Gas pressure needed in the pad: $\frac{0.14 \text{ lbs}}{0.44 \text{ sq.in.}} = 0.3 \text{ psi}$

Pressure reduction by the flow restriction nozzle 50%

Supply pressure 0.6 psi

A gas filter (milipore) of sufficient capacity is needed close to the gyro.

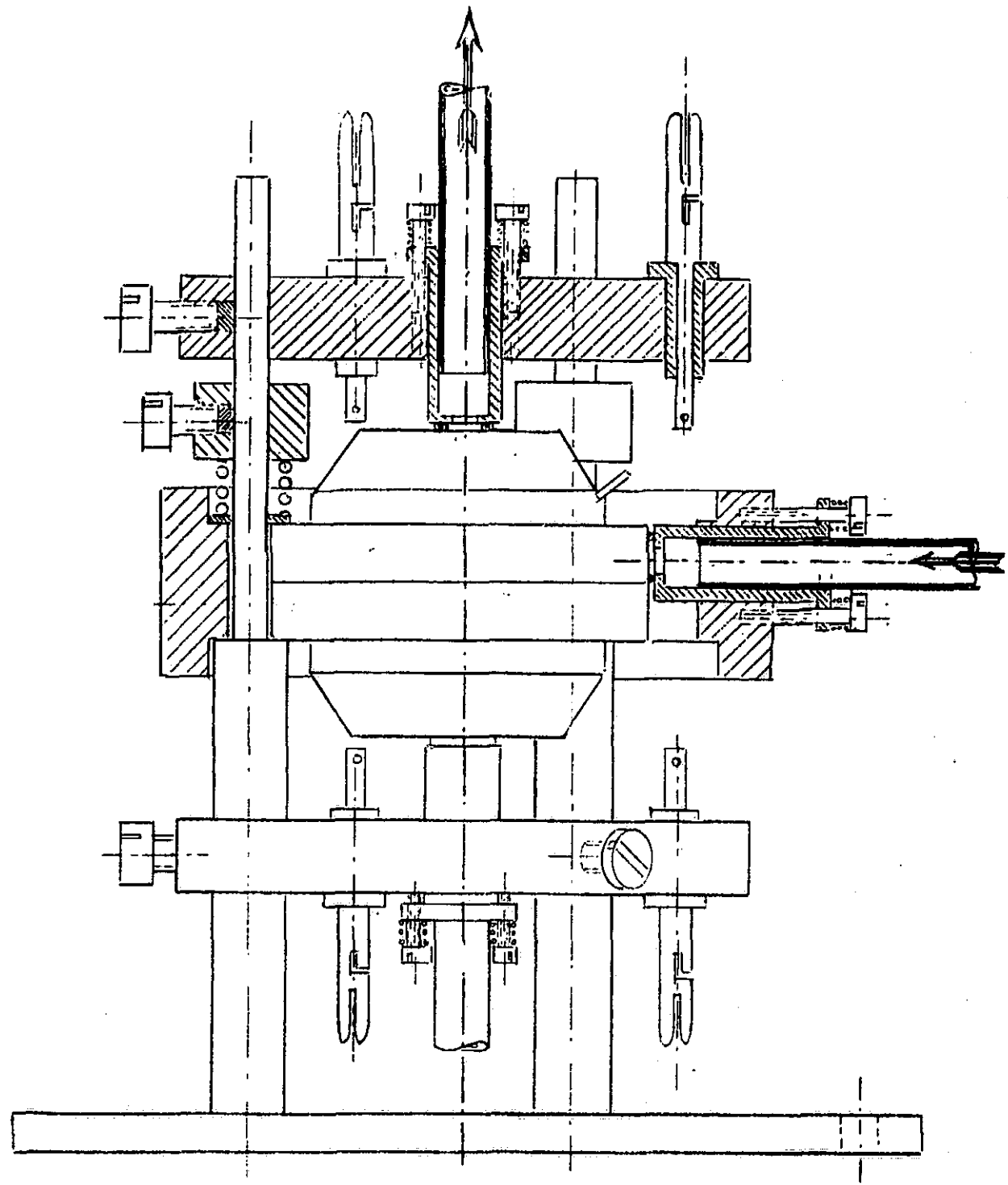


FIGURE 4-52. GYRO MOUNT FOR HORIZONTAL SPIN TESTS

UNIDENTIFIED DRAWING
OF POOR QUALITY

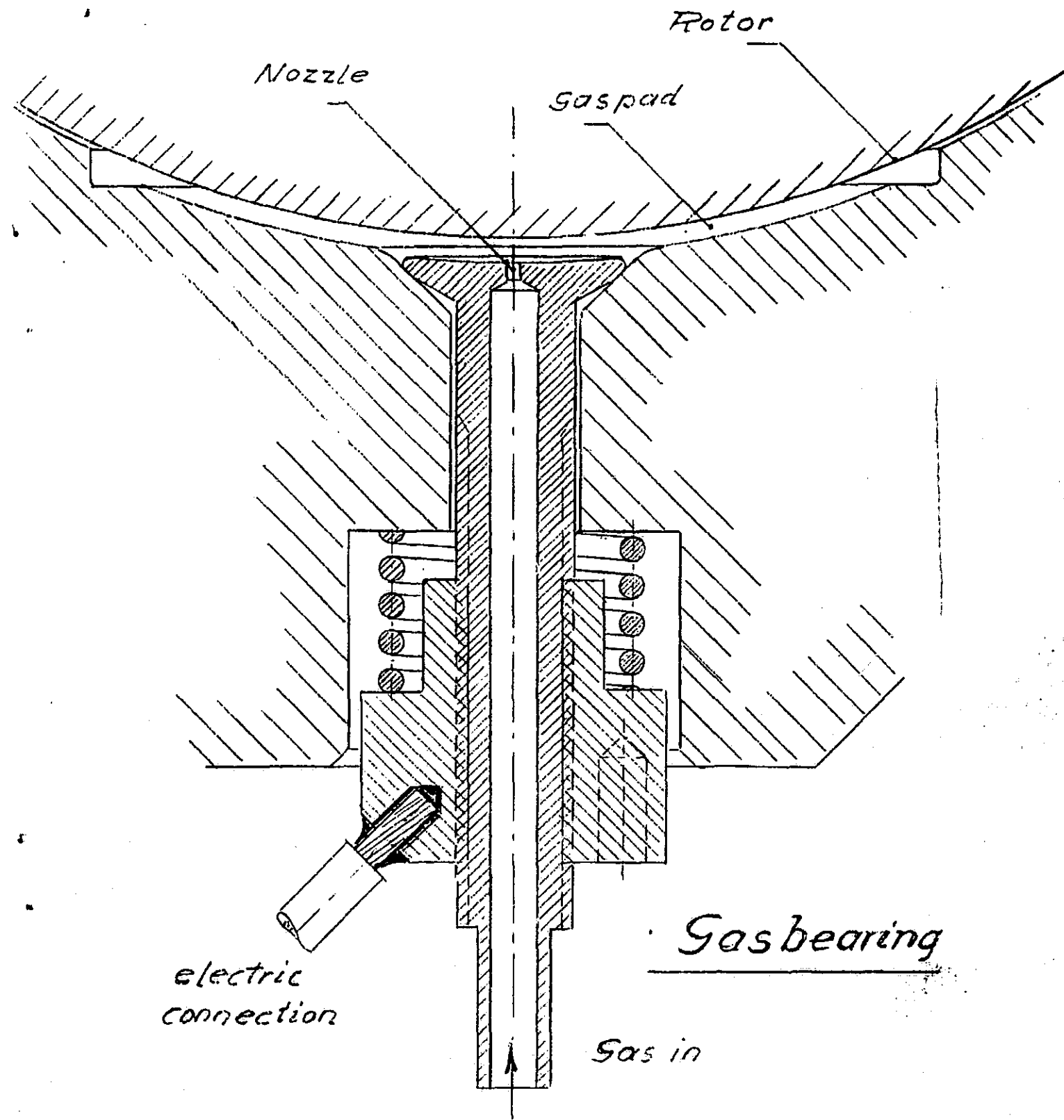


FIGURE 4-53. AUXILIARY GAS BEARING FOR ROTOR LEVITATION